PARTICLE-WALL INTERACTIONS IN TURBULENCE FLOW TO PREDICT EROSION IN PIPELINES & DEVICES

Nikolaos Galanos

Supervisor:

Dr William Dempster

Faculty of Mechanical and Aerospace Engineering

University of Strathclyde

This dissertation is submitted for the degree of Master of Philosophy

May 2022

Abstract

The aim of this study is the development and validation of computational fluid dynamics models (CFD) for two-phase dispersed flow when applied to erosion of surfaces due to particle impact. The main objectives were to understand the particle forces, understand the influence of the particle size and material on the erosion mechanism, develop and integrate the modified Finnie erosion model and perform numerical studies on channel cavities to predict material removal from the impacted surface.

An Euler-Lagrangian methodology is used and adapted to accommodate a larger number of particles. It uses time-averaged mass and momentum conservation equations to describe the time-dependent motion of fluid and particles. These equations are discretised by the Finite Volume Method (FVM) and are solved by the PIMPLE algorithm. The turbulence of the continuous phase is described utilising the k-ωSST turbulence model which incorporates turbulence terms to account for the effects of both phases.

The investigation of the particle-wall and particle-particle effects in particle-laden turbulence flows is also carried out. This is achieved by a Lagrangian approach where the motion of the particles is tracked. Initially, the simulated particle-laden flow is validated in channel geometry.

Finally, the erosion mechanisms are reviewed and an erosion model is developed and incorporated in the CFD-DEM coupled simulation solver. The developed model is applied to a turbulent flow within a channel incorporating a cavity. The simulated results are validated using literature established experimental and computational results for both cases. The CFD analysis on this study has been implemented in OpenFOAM (OF) software in which the erosion modelling has been coded.

The study shows that the DPM solver provides good results for the particle motion on a viscous fluid flow. Moreover, the solver produced similar results for the turbulence laden flows in a channel. The integrated erosion model has been tested on a channel flow and the erosion rate is comparable to the numerical data found in the literature. The applied model on the annular cavity shows good agreement in the

aggregate values on the material removal rates due to the particle impact compared to the experimental data.

Table of Contents

List of Figures

List of Tables

List of Abbreviations

Greek Symbols

α	Impact angle
α_{po}	Impact angle at which horizontal velocity component has just become zero when particle leaves body
α_{dc}	Constant for damping coefficient
α_c	Continuous phase volume fraction
α_d	Dispersed phase volume fraction
$\acute{o}$	Lift force term
β	Mass load ratio
β_1	Turbulent model constant
Γ	Diffusivity
δ	deformation wear factor, the amount of energy needed to remove unit volume of material
δ_n	Normal overlap displacement
δ_t	Time step
δ_x	Cell size
δ_t	Tangential overlap displacement
ΔN	Number of elements
ΔQ	Total volume loss
ΔV_0	Critical volume
ΔV_{mo}	Volume with eliminated variation
ε	Coefficient of restitution
ε_{dc}	Dry coefficient of restitution
ε_{eff}	Effective coefficient of restitution
ε	Turbulent dissipation
ε_{VT}	Total erosion rate
ε_{VP}	Erosion caused by deformation
ε_{VC}	Erosion caused by cutting
ε_T	True strain
ε_c	Critical strain
E	Wall constant

E_m	Material Young's modulus
E_s	Particle Young's modulus
E_w	Wall Young's modulus
η	Damping coefficient
η_{nw}	Normal damping coefficient
η_{tw}	Tangential damping coefficient
$\tilde{I}$	Pressure impulse
κ	von Karman constant
K	Experimental erosion value
K_s	Scaling coefficient
μ_c	Continuous phase dynamic viscosity
μ_t	Eddy viscosity
M	Mass
M	Matrix
ν	Fluid kinematic viscosity
ν_m	Material Poisson's ratio
ν_s	Particle Poisson's ratio
ν_t	Kinematic eddy viscosity
ν_w	Wall Poisson's ratio
ν_T	Turbulence viscosity
π	Math constant
P	Plastic flow stress
ρ	Density
ρ_c	Continuous phase density
ρ_f	Air density
ρ_p	Particle density
σ_k	Turbulent model constant
σ_y	Yield stress
σ_ω	Turbulent model constant
ΣF_{ex}	Summation of external forces
τ	Reynolds stress
τ_C	Time between collisions
τ_{ij}	Subgrid-scale tensor

τ_w	Wall shear stress
τ_V	Momentum particle response time
υ	Velocity y-component
υ'	Fluctuation velocity
υ_i	Dispersed phase velocity
φ	Cell gradient
φ_f	Face volume term
ϕ	Fluid domain variable
$\bar{\phi}$	Spatial filter of phi
χ	Cutting wear factor, the quantity of energy needed to scratch out unit volume from a surface
$\dot{\chi}_t'$	Horizontal velocity of particle tip when cutting ceases
ψ	Function
ψ	Constant value
ω_i	Rotational velocity of particle i
ω_P	Particle rotational speed
ω_{log}	Logarithmic sublayer
ω_{vis}	Viscous sublayer

Roman Symbols

a	Lift force term
A	Particle area
B	Channel span
B_k	Turbulence constant
c	Fraction of particles cutting in idealised manner
C	Turbulent cross-diffusion term
$C_{1,2}$	Empirical constant
C_μ	Turbulence constant
C_k	Turbulence constant
Co	Courant number
C_D	Drag coefficient
C_l	Lift force coefficient
C_{ld}	Lift force ratio

C_{vm}	Basset force coefficient
C_{ij}	Sub-grid-scale cross stresses
d	Vector
D	Domain
D	Particle diameter
e	Math constant
e	Erosion rate on the point of impact
ER	Erosion rate
f	Lift force term
f	Friction coefficient
F_B	Basset (history) term
F^{cp}	Sum of fluid-particle interactions
F_D	Steady state drag force
F_G	Gravitational force
$F_{s,i}$	Saffman-Mei lift force
F_{UF}	Undisturbed flow force
F_{VM}	Virtual (added) mass term
F_{niw}	Normal contact force
F_{tiw}	Tangential contact force
$F_{vm,i}$	Virtual mass force
F_s	Particle sharpness factor
F_C	Blending function
g	Gravity
G	Gaussian filter function
G_0	Erodent feed rate
G_s	Shear modulus
h	Entrance channel height
H	Step channel height
I	Turbulence intensity
I	Relative turbulence intensity
I_P	Particle moment of inertia
k	Cell
k	Turbulent kinematic energy

κ^+	Wall turbulence kinematic energy
k_n	Normal stiffness
k_t	Tangential stiffness
K_p	Stress constant
l	Length scale
l	Ratio of depth contact
L	Turbulence characteristic length scale
L_D	Downstream channel length
L_{ij}	Leonard stresses
L_U	Upstream channel length
m	Mass
m_p	Particle mass
n	Normal vector
n	Impact velocity power law coefficient
n_p	Dimensionless strain hardening exponent constant
p	Pressure (density normalised)
$\bar{p}$	Filtered kinematic pressure
p	Plastic flow stress
P	Particle
P_n	Norman force component
P_t	Tangential force component
r	Sphere radius
r	Gradient
R	Divergence stress tensor
R_{ij}	Sub-grid-scale Reynolds stress
Re	Reynolds number
Re_G	Shear Reynolds number
Re_r	Relative Reynolds number
Re_y	Turbulent Reynolds number
S_ϕ	Source term
S_{ij}	Mean strain rate tensor
S_p	Source term due to particle influence on the fluid
St	Stokes number

t	Time
t_{ij}	Tangential unit vector
T	Particle torque
u	Velocity x-component
u^+	Dimensionless friction velocity
u_i	Filtered velocity
u_i	Continuous phase velocity
$\sqrt{\overline{u'^2}}$	Root mean squar of carrier fluid turbulence fluctuations
u_T	Friction velocity
U	Fluid velocity vector
U_c	Continuous phase velocity
U_p	Particle velocity
U_{iw}	Velocity vector of particle I relative to wall
U_{siw}	Slip velocity of the contact point
$U_{x,0}$	Maximum velocity at centreline
$U_{x,mean}$	Mean fluid velocity
$U_{x,rms}$	Fluctuating fluid velocity
$U_{x,avg}$	Averaged mean velocity in the inlet
V	Volume
V_c	Continuous phase volume
V_d	Dispersed phase volume
V_k	Cell volume
V_p	Particle impact velocity
$V^{t_c^+}$	Post-collision velocity
$V^{t_c^-}$	Pre-collision velocity
v_r	Rebound velocity
v_{imp}	Impact velocity
w	Velocity z-component
W_p	Sand flow rate
y	Wall distance
y^+	Dimensionless wall distance
y_t	Depth of cut

Acronyms

API	American Petroleum Institute
BC	Boundary conditions
BFS	Backward - Facing Step
CFD	Computational Fluid Dynamics
CLBM	Cascaded Lattice Boltzmann Method
DEM	Discrete Element Modelling
DIC	Diagonal-based Incomplete Cholensky
DNS	Direct Numerical Simulations
DPM	Discrete Phase Modelling
E-L	Euler-Langrange
FOAM	Field Operation And Manipulation
GAMG	Geometric agglomerated Algebraic Multi-Grid
HRN	High Reynolds Number
IB	Immersed Boundary
LES	Large Eddy Simulations
LRN	Low Reynolds Number
LUST	Linear-Upwind Stabilised Transport
N-S	Navier-Stokes
OF	OpenFOAM
PD	Peridynamics
PIC	Particle-In-Cell
PIMPLE	PISO-SIMPLE
PISO	Pressure Implicit Splitting Operator
RANS	Reynolds-Averaged-Navier-Stokes
SAE	Society of Automotive Engineering
SGS	Sub-Grid-Scale
SIMPLE	Semi-Implicit Method for Pressure-Linked Equations
SST	Shear Stress Transport
TKE	Turbulent kinetic energy
VOF	Volume of Fluid

Statement of Original Authorship

The work contained in this thesis has not been previously submitted to meet requirements for an award at this or any other higher education institution. To the best of my knowledge and belief, the thesis contains no material previously published or written by another person except where due reference is made.

Signature: Nikolaos Galanos

Date: 30/04/2022

Acknowledgements

I would like to say a special thank you to my supervisor, Dr William Dempster. His support, guidance and overall insights in this field have made this an inspiring experience for me. Also, I would like to thank Dr Sina Haeri, who has supported me throughout this research project.

I would like to give special thanks to my wife Merlinda and my daughter Eliza for their continuous support and understanding when undertaking the research and writing the project.

1 Introduction

1.1 BACKGROUND AND MOTIVATION

Particle-laden flows are of great interest both for academia and industry. The understanding and modelling phenomena which occur is key for a variety of systems like internal combustion engines, chemistry, hydraulics and many others. In a similar fashion, the consequent erosion of the industrial equipment from particle-laden flows causes vast financial losses to various industries. Subsequently, the understanding of the erosion mechanisms and predictive modelling is a subject of significant research interest in recent years.

There are several methods to simulate these physical phenomena and the most often used are the Direct Numerical Simulations (DNS), Volume of Fluid (VOF) and Mixture models. In DNS the multi-phase flow modelling represents all the scales (geometrical and turbulent) and are solved to the associated boundaries and interfaces. This is not practical for industrial-scale problems as the computational cost is enormous. In the VOF approach, different scales are resolved and the turbulence is solved temporally by averaging using the Reynolds-Averaged-Navier-Stokes (RANS) or spatially using the Large Eddy Simulation (LES). The Mixture model is a simplified model where the phases are treated as mixtures solving the momentum and mass conservation equations for the mixture and the mass phase fraction for all except one phase.

Erosion modelling has been a controversial subject for decades as engineers struggle to understand the process fully resulting in an enormous number of publications. In these publications, there are numerous numerical and empirical models with poor agreement among them. However, two predominant theories have appeared establishing a consensus on modelling: cutting and deformation mechanisms. Cutting wear describes the creation of an impact crater through elastic/plastic deformation with edge removal through repeated impacts. It is predominant in ductile materials and low attack angles. On the other hand, the deformation mechanism occurs when several particles hit the same area, stress concentrations occur during contact and deforms and cracks the material. If these stresses exceed the elastic limits, plastic deformation occurs. This deformation results in hardening of the material and

eventually after further load, material is removed from the surface and is entrained with the fluid [1].

1.2 OBJECTIVES

This study is concerned with the prediction of the physical flow and surface erosion of pipeline features by considering the modelling of the particle and fluid motion, the solid deformation and erosion mechanism effects. These complex phenomena associated with particle-laden flows have been investigated in the literature both experimentally and numerically. This project is investigating the particle-laden flows and its corresponding erosion at geometries that have been assessed in the literature. The project utilises computational dynamic simulation (CFD) tools to represent and calculate the physical characteristics of the processes.

The turbulence fluctuations are primarily responsible for particle transport near the walls and control the rate of erosion [2], [3]. A multiscale modelling approach is adopted in this project to provide a comprehensive correlation to relate the rate of erosive collisions to the particle flow characteristics. The first step is to assess the contribution of the particle forces. The accuracy of the available drag and lift in the models considering a single particle is investigated in the near-wall region. Following this analysis, an Eulerian-Lagrangian (E-L) type simulation (unresolved – large number of particles) provides a correlation between turbulence flows and the rate of erosion. This is achieved by coupling the Discrete Phase Modelling (DPM) with CFD. The numerical results are assessed with benchmark cases available in literature.

The specific objectives of the project are:

- To understand the forces acting on a particle – considering a single particle sedimentation and validate the DPM solver.
- Review the erosion mechanisms and understand the influence of particle size and material properties on the process.
- Develop an erosion model based on the existing literature and embed it into the OpenFOAM DPM solver.
- Perform a study to predict the surface erosion rate (material removal) in an aluminium pipe annular cavity related to sudden expansions or

contractions in comparison with experimental and computation results from the literature.

1.3 THESIS OUTLINE

The approach taken to meet these objectives are as follows. The E-L solver has been selected and an initial study carried out to check its validity for the desired scope. Firstly, the motion of a single particle impacting on a surface is examined followed by the study of a particle laden flow in backward facing step. Experimental and numerical data from previous studies are used for the assessment of the simulation results. Then, a modified Finnie erosion model selected has been integrated to the E-L solver. A channel cavity geometry was used to check the erosion rate of this model against the default Finnie erosion model of the OF library and numerical results. Finally, the investigation of the material removal rate on an annular cavity due to particles presence is examined using experimental and numerical data from the literature. The thesis is organised as described in the following outline.

- Chapter 1 represents the introduction.
- Chapter 2 contains the literature review of the study and the CFD methodologies including the discretisation schemes. The properties of the dispersed phase are given and finally, the unresolved CFD-DEM coupling is explained.
- Chapter 3 contains the theoretical background modelling for all the cases studied; including the particle-wall interactions, the turbulence methodology and boundary conditions and finally the erosion models used in the study. Also, the developed erosion model in OpenFOAM (OF) software is described and integrated into the E-L solver.
- Chapter 4 contains the study of the particle-wall collisions and the forces applied to the particle. An analysis of a single particle sedimentation is utilised to examine the E-L model.
- In Chapter 5 the modelling of a dispersed flow carrying a large number of solid particles is assessed against a benchmark case of a channel flow.

Experimental data for particle-laden and unladen flows are used for the evaluation.

- In Chapter 6 the developed erosion model of Finnie is utilised for the analysis of the surface erosion of a pipe channel with an embedded cavity and is examined against the data from the literature (experimental and computational).
- In Chapter 7 the results and findings from Chapters 4 to 6 are discussed further.
- Finally, Chapter 8 contains the conclusions of the study.

2 Literature Review and Methodology

2.1 INTRODUCTION

This chapter provides the existing literature review on particle interactions in turbulent flows and associated erosion modelling. It starts with the particle motion and interactions and what is the impact on the particle-laden flows. An overview of the turbulent flow modelling with RAS methods is described. An overview of particle erosion modelling is described with attention to the models that have been used in this study. Finally, the methodology used is given considering the numerical solutions and the phase coupling.

2.2 PARTICLE MOTION & INTERACTIONS

The motion of a sphere falling from rest in a quiescent fluid under gravity was studied by Basset [4] and later Boussinesq [5] and Oseen [6]. A rigorous derivation of the motion equation for small particles in non-uniform, unsteady flows at low Reynolds numbers was performed by Maxey and Riley [7]. In their equation, apart from gravity other additional body forces are included that contribute to the fluid dynamic force on the particle. Crowe et al. [8] addressed these terms individually and rewritten for conditions outside the region which Maxey and Riley's equations valid.

There are several studies on the rebound of colliding particles in the last decades. Davis, Serayossol & Hinch [9] employed an elastohydrodynamic model in which they showed that the pertinent parameter for collision in the fluid is the Stokes number St = $1/9(\rho_p/\rho_f)$Re, (where ρ_p and ρ_f are the particle and fluid densities, respectively) which compares the particle inertia to the viscous forces. Joseph et al. [10] show that the rebound velocity strongly depends on the Stokes number and weakly on the material elastic properties. Also, it has been shown that in St < 10 the coefficient of restitution is 0, therefore no rebound occurs [10], [11], [12] and for St > 500 the coefficient of restitution reaches an asymptotic value to that for a dry collision measured in air or vacuum. Ardekani & Rangel [13] investigated the dependence of the effective coefficient of restitution on the Stokes number using a distributed Langrange

multiplier-based computational method in a solid-fluid system for the bouncing motion of a spherical particle onto a wall.

Gondret et al. [12] show that in a liquid, drag and added mass effects are important but not sufficient, whereas the Basset term is negligible even in large Reynolds numbers. Legendre et al. [14] have shown that the added mass of a particle doesn't change with Reynolds number. Its contribution to the particle depends on instantaneous accelerations similar to irrotational theory predictions. They correlated the coefficient of restitution with Stokes number (including added mass) with experimental data. For a particle moving towards the wall, the added mass coefficient is given by Milne-Thomson [15] which depends on the sphere radius r and the distance from the wall y. Ardekani, Rangel & Joseph [16] used the viscous potential flow theory to calculate the contribution of the force to the particle proportional to the particle acceleration. Their equation does not match well the Milne-Thomson equation for values of factor 1 + y/r less than 1.5 whereas they are identical for values above 3.5.

Zhang et al. [17] utilised a coupled model consisting of a Discrete Element Method (DEM), an Immersed Boundary (IB) and Cascaded Lattice Boltzmann Method (CLBM) to fully resolve the interactions around the particle within a viscous fluid. The particle-wall interaction is compared with results in the literature [13]. The peridynamics theory is also employed for modelling the material damage. It is shown that for the deformable plate (peridynamics theory PD) the velocity after the first rebound is slightly smaller than the rigid plate (DEM) but both are in very good agreement with the literature results (Fig. 2.1).

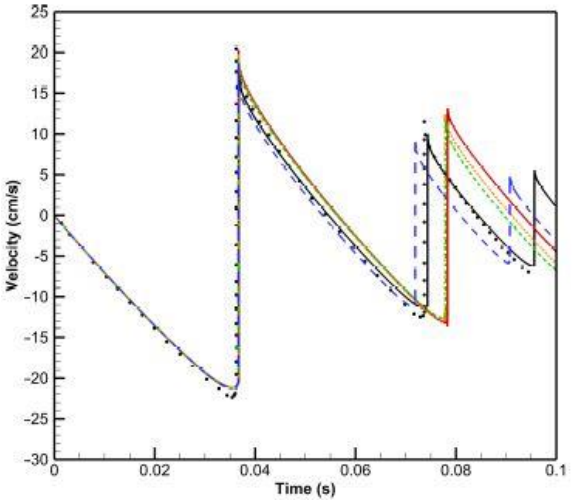

***Figure 2.1: Particle vertical velocity moving in fluid varies with time. The results from Ardekani and Rangel* [13] ••*; DEM* —*; PD, N = 10* —*; PD, N = 15* —*; PD, N = 20* ----*; PD, N = 25* ---- [18]**

2.3 TURBULENCE MODELLING

2.3.1 Direct Numerical Simulations

In the Direct Numerical Simulation (DNS) method, the mean and all turbulent velocity fluctuations are computed. This computation is modelled from boundary conditions on the particle surface instead of empirical correlations. For an incompressible flow, the continuity and Navier-Stokes (N-S) equations form a set of four equations with the unknowns u, v, w and *p*. The DNS takes these equations to set as a starting point for developing a transient solution with fine spatial grids to solve the unsteady N-S equations. These can resolve the Kolmogorov length scales where energy dissipation arises and with small time steps that can resolve the fastest fluctuations period. Overall, these simulations are quite powerful for accurate correlations of the micro-scale transport coefficients however, the computation resources required are quite costly, therefore the method is not used for industrial applications [19], [20].

2.3.2 Large Eddy Simulations

The Large-Eddy Simulation (LES) concept is the method to separate and calculate the larger eddies of the flow in time-dependent simulations, while the smaller eddies behaviour can be captured with a compact method. The foundation of LES modelling is based on Smagorinsky's work [21]. LES is introduced by a filtering concept to separate small and large eddies. During spatial filtering, all small eddy information is removed. The interaction effects between the resolved large eddies and the smaller unresolved ones gives the sub-grid-scale (SGS) stresses. When the finite volume method is used, the space-filtered flow equations are solved on a control volume grid along with the unresolved stresses of the SGS model. This yields the mean flow and all turbulent eddies at scales larger than the cut-off width [19]. In the fluid domain *D*, any variable φ can be decomposed into a large-scale part and a small-scale part, respectively. A filter function G has usually been taken to be a Gaussian filter in infinite domains or a piecewise continuous distribution of bounded support, in compact domains.

For incompressible turbulent flows, the N-S equations filtering yields:

$$\frac{\partial \bar{u}_i}{\partial t} + \frac{\partial\left(\overline{u_\iota u}_j\right)}{\partial x_j} = -\frac{1}{\rho}\left(\frac{\partial \bar{p}}{\partial x_i}\right) + \frac{\partial \tau_{ij}}{\partial x_j} + \nu\nabla^2\bar{u}_i \qquad (2.1)$$

where $\bar{u}_i$ is the filtered velocity, ρ the density, $\bar{p}$ is the filtered kinematic pressure, v is the kinematic viscosity, and τ_{ij} is the sub-grid-scale stress tensor ($\tau_{ij} \rightarrow 0$ as $\Delta \rightarrow 0$). Moreover, $\partial\bar{u}_i/\partial x_i = 0$ as the continuity equation requires. The full form of the SGS stress tensor is the summation of the Leonard stresses (L_{ij}), sub-grid-scale cross stresses (C_{ij}), and sub-grid-scale Reynolds stresses (R_{ij}) and is given by [22]:

$$\tau_{ij} = L_{ij} + C_{ij} + R_{ij} = \left(\overline{\bar{u}_\iota \bar{u}_j} - \bar{u}_i\bar{u}_j\right) + \left(\overline{\bar{u}_\iota u_j' + u_\iota'\bar{u}_j}\right) + \left(\overline{u_\iota' u_j'}\right) \qquad (2.2)$$

2.3.3 Reynolds Averaged Simulations (RAS)

Two equation turbulence models are a common approach to solve turbulence flow. The k-ε and the k-ω model have become industry standard models nowadays and are used to solve fluid engineering problems. On these models, the one transported variable is the turbulent kinematic energy k and the second transported variable which determines turbulence scale is either turbulent dissipation ε or the specific turbulence dissipation rate ω (depending on the model used). However, these two-equation turbulence models are also very much still an active research area. The two-equation models include two extra transport equations to represent the flow turbulence. This allows a two-equation model to account for history effects of turbulent energy (convection and diffusion).

The basis of the two-equation models is the Boussinesq eddy viscosity assumption in which the Reynolds stress tensor τ_{ij} is assumed proportional to the mean strain rate tensor S_{ij}:

$$\tau_{ij} = -\rho\overline{u_i' u_j'} = 2\mu_t S_{ij} - \frac{2}{3}\rho k\delta_{ij} = \mu_t\left(\frac{\partial U_i}{\partial x_j} + \frac{\partial U_j}{\partial x_i}\right) - \frac{2}{3}\rho k\delta_{ij} \qquad (2.3)$$

where μ_t is the eddy viscosity which is a scalar property [23]. In the k-ε model, the kinematic eddy viscosity ν_t is a product of a velocity scale $\partial = \sqrt{k}$ and a length scale $l = \mathrm{k}^{3/2}/\varepsilon$. As proposed by Wilcox [24], [25], [26], an alternative variable ω can be derived as $\omega = \varepsilon/\mathrm{k}$ [s^{-1}] replacing the ε variable in the model. With the ω variable, the length scale becomes $l = \sqrt{\mathrm{k}}/\omega$ and the eddy viscosity is given by $\mu_t = \rho\mathrm{k}/\omega$.

The k-ωSST model based on Menter's observations [27] that k-ε model is less sensitive in the free stream flow, but in the near-wall region the results are unsatisfactory. This leads to a hybrid model that uses k-ε model in fully turbulent flow in the far-field and the k-ω model in the near-wall region [28], [29], [30]. The Reynolds stress and k transport equation remain the same, but the ε equation transformed to ε = kω.

An important parameter of the k-ωSST model is the blending functions which are used to transit from one model to the other. These are modified the cross-diffusion term and are also used for model factors that take value C_1 for the original k-ω model and value C_2 in Menter's transformed k-ε model:

$$C = F_C C_1 + (1 - F_C) C_2 \tag{2.4}$$

A blending function F_C is a function of the ratio of turbulence $l_t = \sqrt{k}/\omega$, the wall distance y and the turbulence Reynolds number $Re_y = y^2\omega/\nu$. The F_C functional form is chosen so that it:

- is zero at the wall
- approaches unity in the far-field
- produces a smooth transition between the wall and the boundary layer edge.

Therefore, this method combines the k-ω model benefits in the near-wall behaviour with the k-ε model robustness in the far-field in a numerically stable way [19].

To summarise, the methods for turbulence modelling are given in Fig. 2.2. The DNS methods resolve all the motion scales, LES resolves most of the scales with the smaller scales modelled and on the other spectrum end RAS resolves only the large-scale eddies and most of the scales are modelled.

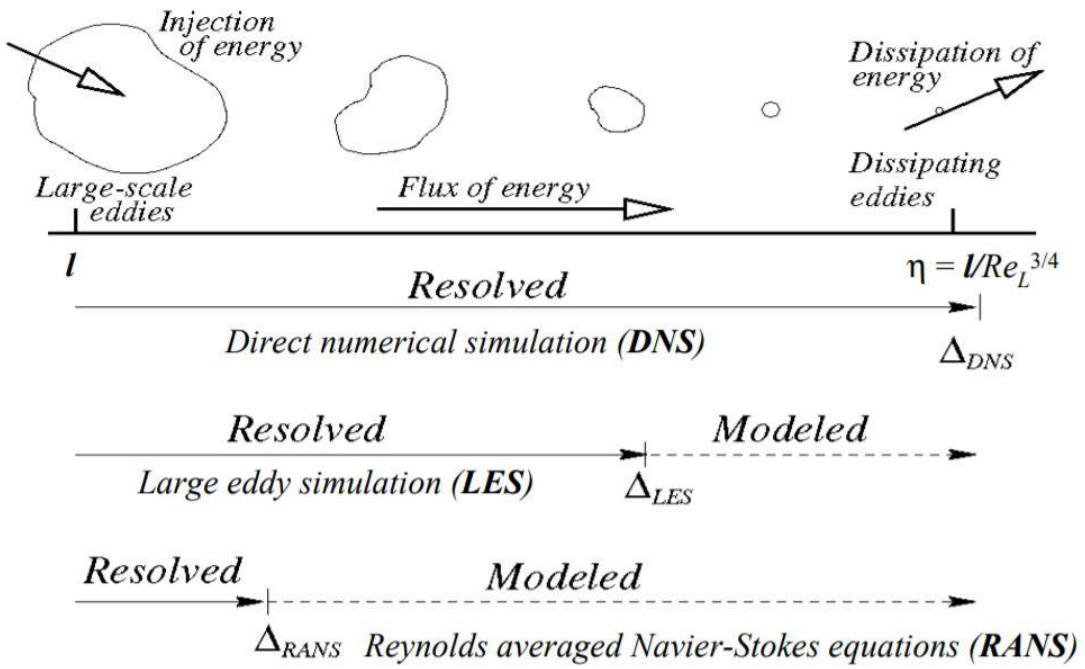

Figure 2.2: Schematic of the methods for the turbulence modelling

In Fig. 2.3 a visual difference on the resolved scales between the RAS and LES for a simple geometry.

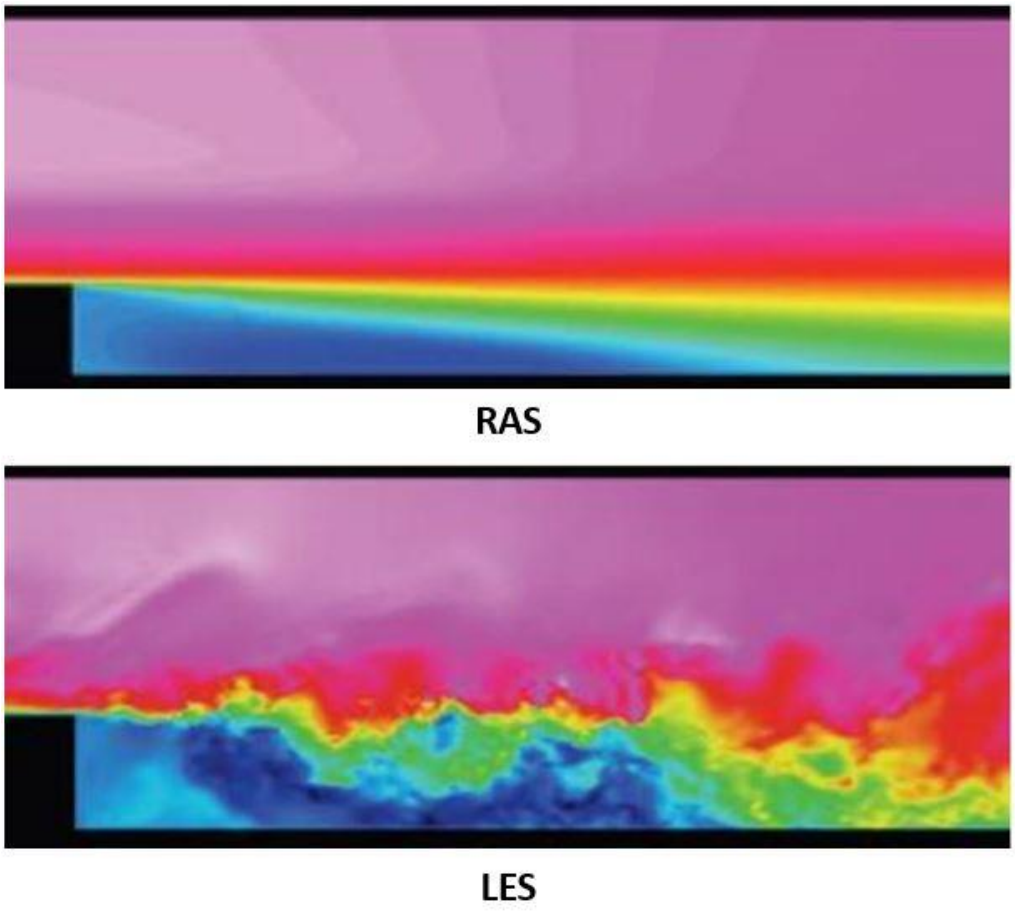

Figure 2.3: RAS against LES modelling of the flow in a simple geometry

2.3.4 Particle-fluid turbulence interactions

The interactions between particles and fluid turbulence are very complex and there are not fully understood in industrial and natural flows. Usually, particle-laden flows are inhomogeneous and anisotropic including wall interactions and flow separation. The main problem is the prediction of the fluid turbulence modifications by the particles. Moderate mass loadings of fine particles create significant changes to the flow turbulence levels. Small size particles weaken fluid turbulence whereas large size particles enhance it [31], [32]. Despite their contribution to the subject, neither managed to acknowledge the principal parameters that govern the turbulence modifications.

Different mass loading and measurement techniques used in numerous studies; a direct results comparison is not an easy task. However, the trend of the increase of attenuation with increased mass lading can be observed. Squires & Eaton [33] using direct numerical simulation found that attenuation was nearly constant with Stokes number changes. Elghobashi & Truesdell [34] showed that changes in turbulence decay rate depend on factors such as gravitation.

The backward-facing step (BFS) geometry is utilised by Maeda, Kiyota & Hishida [35] and Hishida & Maeda [36] with 50 % mass loading of glass particles with a diameter of 45 μm. In both studies, it is shown a reduction in the turbulent fluctuations along the dividing streamline but little modification in the free stream region or the re-attachment point. Hardalupas, Taylor & Whitelaw [37] investigated axisymmetric sudden expansions with mass loading between 23% and 86% of glass particles with a diameter of 80 μm. They found that in the near field, the turbulent fluctuations were decreased and further downstream the mean flow modifications increase turbulence levels.

Fessler & Eaton [38] investigated the turbulence modifications in a BFS with a fully developed channel flow inlet. The gas-phase velocities were measured in the presence of 3% to 40% mass loading of glass sphere particles of 90 and 150 μm diameter and copper sphere particles of 70 μm diameter. The attenuation is reduced as the mass loading, Stokes and Reynolds numbers are decreased. Despite the significant particle loading in the separated shear layer or the behind-step redevelopment region, no modification of the turbulence was found. Kasper, Turnow & Kornev [39] used the Fessler & Eaton results to validate their LES model. Greifzu et al. [40] utilised two

different CFD programs to simulate and obtain numerical results using the BFS case as a benchmark for validation. It is shown that ANSYS FLUENT slightly under-predicted the particle dispersion whereas OpenFOAM overestimates it. As the OF is used in this study, similar results are expected for the particle dispersion.

2.4 REVIEW OF EROSION MECHANISMS

2.4.1 Introduction

Erosion from particle impingement is very common in many applications. Many studies have been published on this matter; however, there is little agreement on the generality and accuracy of numerical predictions. A literature review conducted by Meng and Ludema [41] identified 28 equations including 33 parameters in more than 5000 papers until 1992. A consensus has emerged that the two mechanisms acting concurrently to produce damage are cutting and deformation wear.

In the oil & gas industry, unwanted production of sand from wells is common. This sand production can result in pipeline erosion and blockage, corrosion and other complications which cause severe financial and environmental damage. Sand erosion is one of the predominant results of sand production. This can cause equipment failure, pipeline leaks resulting in environmental disasters and/or personnel potential hazards. Therefore, solid particle erosion rate prediction is a key tool in designing and selecting equipment to prevent failures. Several models and approaches have been proposed by researchers; however, the solid particle erosion mechanism is still not fully understood.

Usually, erosion prediction models are divided into three categories: empirical, mechanistic and CFD-based. Since erosion is complex, most proposed erosion prediction models are a combination of all these categories. An overall discussion on the empirical and mechanistic models is implemented. The focus of this work is on CFD based erosion modelling. The modelling categorisation is shown in the following diagram (Fig. 2.4). A summary of the empirical and mechanistic modelling is given below (section 2.4.3). An extended overview of the CFD-based modelling is provided in the section 2.4.5 as this is the erosion prediction approach in this study.

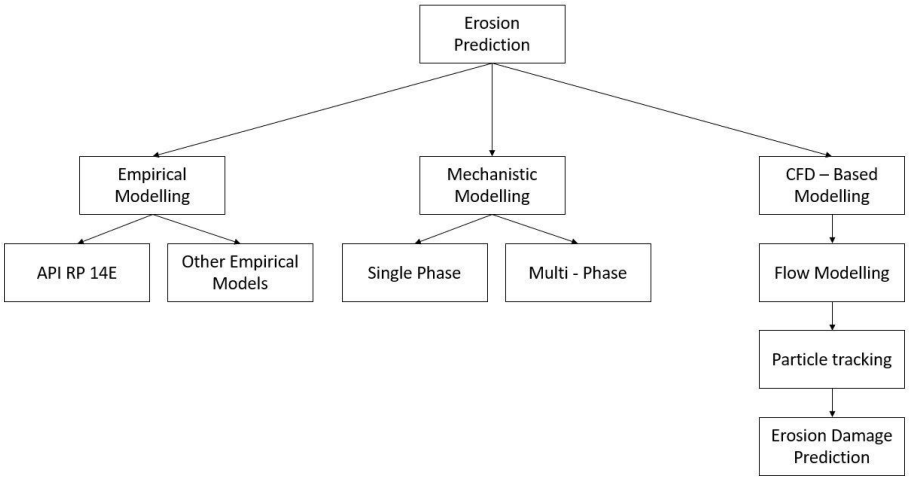

Figure 2.4: Erosion prediction flowchart

2.4.2 Mechanisms of solid particle erosion

Two mechanisms act together to produce the wear scar: cutting and deformation wear. When particles hit the surface, material is removed in plowing and cutting action and is called cutting wear. This mechanism is the predominant one for ductile materials and particles impinging at low angles of attack with respect to the surface being eroded. Alternatively, several particles might impact the same place transferring some of their kinetic energy to the surface in the form of hardening work. According to this theory, in a given collision with the target material, as soon as the particle contacts the surface, stress concentrations appear as a result of the elastic deformation that takes place. If these stresses are not over the elastic limit of the target material and leave aside fatigue damage effects, they should cause no deformation. However, if the elastic limit is reached, plastic deformation will occur at the location of the maximum stress. The repeated impacts then create a plastically deformed layer that will deform further upon repetition of the particle collisions. This deformation causes hardening and increases the elastic limit in that region turning the material harder and more brittle until it reaches a point where it can no longer be plastically deformed. Eventually, upon further load, pieces of the material's surface separate from the target and are carried away by the fluid [1]. Before erosion data is considered it should be noted that erosion data is reported differently by various investigators. For example, erosion rates are normally a mass loss of materials or thickness loss of materials as a function of time such as kg/hr or mils per year or mm per year. Some authors report erosion data in the units of mass loss, volume loss or thickness loss per mass of impacting particles such

as g/g or mils/lb (in/1000 lb), etc. The latter will be referred to as the “erosion ratio” in this manuscript [42].

2.4.2.1 Ductile materials

Finnie [43] proposed a micro-geometry model for ductile materials. He suggested that erosion in ductile materials is the result of micro-cutting. When a particle impacts a surface at a low impact angle, it creates a crater. Other particle impacts make the crater larger and also pile up material around the crater.

Finnie [44] modified the model to address this weakness. Based on the erosion micro-geometry model work hardening of the metal surface should decrease the erosion rate. However, Levy [45] showed that initial erosion is lower than erosion from previously eroded surfaces. Bellman and Levy [46] proposed a macroscopic erosion mechanism. They suggested that particles hitting the surface create shallow craters and platelet-like pieces. These platelets are easy to separate from the surface by subsequent particle impact (Fig. 2.5). During the formation of platelets, adiabatic shear heating on the surface and work-hardening under the surface occur. The occurrence of these two processes helps platelet formation which explains the higher erosion rate for the steady-state condition compared to the initial erosion rate.

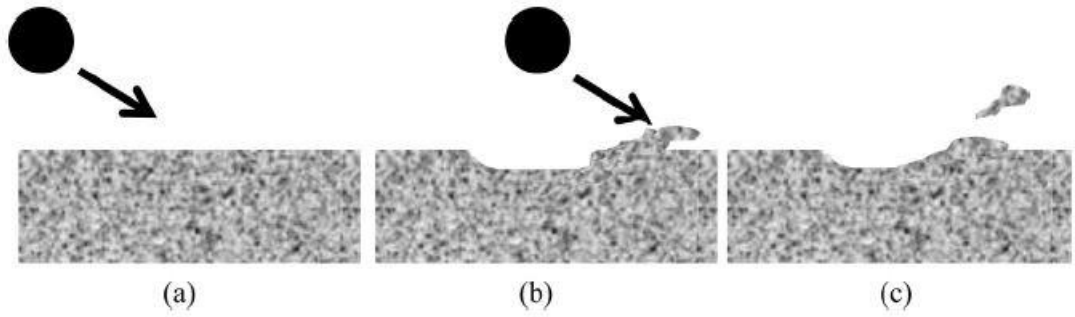

Figure 2.5: Schematic of erosion procedure in ductile material (a): before the impact, (b): crater formation and piling material at one side of the crater, (c): separation of material from the surface **[42]**

2.4.2.2 Brittle materials

Unlike ductile materials, there is wide acceptance of the erosion mechanism for brittle material. It has been suggested that in brittle materials that erosion is due to crack formation [47], [48], [49]. When a particle hits a brittle surface, it creates lateral and radial cracks. Other impacts cause these cracks to grow. These cracks divide the

surface into smaller pieces which can be removed by other particles impacting the surface (Fig. 2.6) [42].

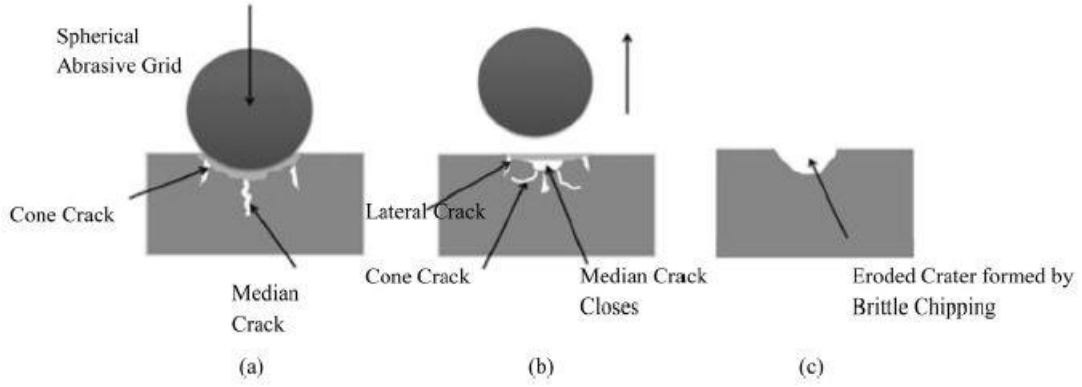

Figure 2.6: Expected mechanism of erosion in brittle material: (a) growth of cone crack and median cracks (b) closure of median and creation of lateral cracks, (c) eroded crater formed **[50]**

2.4.3 Modelling of solid particle erosion

2.4.3.1 Erosion equations

In Finnie's study [44], it is stated that erosion on the surface of a material struck by solid particles depends on the motion of the particles and the material properties. He divided the material into two categories: ductile where erosion is caused by plastic deformation and brittle where the intersection of cracks is the main reason for erosion. Based on some assumptions, he proposed two equations to predict the volume of removed material by a single abrasive grain for low and high particle striking angles.

Finnie [51] modified his previous model [44] to predict erosion for ductile metals. In that study, the parameters that may affect ductile erosion were listed and it was stated that not all these parameters can be implemented in a model (some of them are not controllable or measurable). These models will be discussed in detail in the next chapter.

Bitter [52] [53] proposed repeated deformation and cutting as two mechanisms for erosion and developed two models to predict the erosion rate caused by these two mechanisms for ductile and brittle materials. Total erosion rate is the summation of erosion caused by these two mechanisms (repeated deformation and cutting).

$$\varepsilon_{VT} = \varepsilon_{VP} + \varepsilon_{VC} \quad (cm^3) \tag{2.5}$$

In the first part of his study, he developed an equation, based on the balance of energy for a plastic elastic collision, to predict erosion caused by the deformation mechanism:

$$\varepsilon_{VP} = \frac{1}{2}\frac{M(V_P \sin a - K)^2}{\delta} \tag{2.6}$$

where M is the total mass of impinging particle, V_p is the particle velocity, α is the particle impact angle, K is the velocity component normal to the surface below which no erosion takes place and δ is the deformation wear factor. He compared the model prediction with experimental data and reported that there is good agreement between the model prediction and the erosion data for brittle substances at different impact angles.

In the second part of his study, he considered two scenarios for impacting particles including particles that still have a horizontal velocity component when they leave the body surface and particles with zero horizontal velocity component during the collision. He proposed two models for the cutting mechanism based on these scenarios:

$$\varepsilon_{VC} = \frac{2MV_P(V_P \sin a - K)^2}{(V_P \sin a)^{1/2}}\left\{V_P \cos a - \frac{C(V_P \sin a - K)^2}{(V_P \sin a)^{1/2}}\chi\right\} for\ a \geq a_{p0} \tag{2.7}$$

$$\varepsilon_{VC} = \frac{1/2M\left[V_P^2 \cos^2 a - K_1(V_P \sin a - K)^{3/2}\right]}{\chi} \qquad for\ a < a_{p0} \tag{2.8}$$

where χ is the cutting wear factor, K_1 is a proportional constant, and a_{p0} is the impact angle at which the horizontal velocity component has just become zero when the particle leaves the body. A combined Finnie-Bitter equation is used by Sato et al. [54] to predict single particle impact wear. A modified version of the combined model proposed by Gnanavelu et al [55] provide the erosion ratio ER_r which is defined as the total mass loss to the mass of the particles impacting the surface.

Jennings et al. [56] experimentally reported that melting of the target surface is a major mechanism of ductile material erosion. Based on this hypothesis, he employed dimensional analysis to develop a mathematical model considering the factors that

resist and drive erosion phenomena. Hutchings et al. [57] performed a series of experiments using steel spheres impacting mild steel and reported that their experimental test results successfully simulated erosion of sand particles on metals. They investigated the dependence of crater dimension to impact velocity and angle. A correlation to predict erosion rate based on experimental data was proposed as mass-loss/mass of the sphere. Another mechanistic model to predict the erosion rate for the erosion of metals impacted by spherical particles at normal angles was developed by Hutchings [58]. He proposed a model formulated by an energy balance equation between impacting particles and the metal surface. The main assumption of this model is that particles are not deformed or fractured, and elastic effects are negligible. It was also concluded that although dynamic hardness and ductility are included in the above equation, more investigation is needed to obtain their values and incorporate them in the above equation.

A phenomenological model for erosion was proposed by Huang et al. [59]. They pointed out that particle impact on a target produces normal and tangential surface interactions which cause deformation. They considered the normal component of the force is responsible for “deformation damage removal” and tangential component for “cutting removal”. Considering the normal force, they found equations for maximum width and depth of indentation using the equation of motion in the normal direction. Having those parameters, an equation to calculate elementary indentation volume was suggested. They also derived an equation to calculate the average strain introduced into the surface by normal impact. On the other hand, a cutting profile to calculate cutting volume caused by the tangential force as a function of maximum cutting width, depth and length was suggested. They used equations from Coffin [60] and Manson [61] along with a critical strain equation to calculate the deformation damage removal. For real cutting removal by a particle, they assumed it is proportional to the cutting volume but inversely proportional to the material ductility. It was emphasized that the proposed erosion considers the effect of particle mass, size, shape and speed as well as impact angle and target material properties. The equation suggested predicts the total volume loss by summing the deformation damage removal and cutting removal. A simplified version of their equation was also proposed for situations where solid transport impact angle is small and cutting wear is the dominant erosion mechanism.

2.4.4 Empirical erosion prediction

American Petroleum Institute Recommended Practice (API) 14E suggested one of the earliest empirical equations to estimate the erosional velocity (API RP 14E, 1981). A model for elbows was suggested by Salama and Venkatesh [62]. It used the experimental data for the erosion ratio of ductile metals estimated the erosion rate ER in mils per year (mpy). They also showed that the erosion rate in tees is about half of the erosion rate in elbows. Bourgoyne [63] measured erosion rate in gas-solid, liquid-solid and mist-solid flows in a diverter. He suggested another equation for liquid continuous flow and an equation for the prediction of wall thickness loss in gas continuous flows (dry gas flow or mist flow). The development of these equations is based on experimental data at high flow rates. He also obtained experiments for high sand flow rates that may be produced in diverter systems with production under low concentration. Jordan [64] considered the rate of material volume loss as a variation of the square of the particle velocity and linearly with the volumetric rate when particles impinge on a target wall. He employed Bourgoyne's data to propose his equation. The development of a new phenomenological mechanical erosion model is presented in Huang et al. [59] study which focuses on the effects of abrasive particles on a target surface similar to Finnie studies. In this model, the sum of the volume removal produced by vertical and tangential forces gives the total volume loss approximately and is given by:

$$\Delta Q = Cm\rho_p^{0.15}(V_0 \sin a)^{2.3} + Dm^{1.1875} d_p^{-0.0625} V_0^{2.375} (\cos a)^2 (\sin a)^{0.375} \tag{2.9}$$

where m is the particle mass, the ρ_p is the particle density, V_0 is the impact velocity, d_p is the particle diameter, the coefficients C and D have been derived by experiments are C ≈ 5.5×10^{-4}, 5.5×10^{-4} and 7.5×10^{-4}, D ≈ 0.17, 0.087 and 0.082 for aluminium, copper and SAE-1055 steel, respectively. The other parameters units are in SI and the volume loss is given in [mm^3].

2.4.5 CFD based erosion modelling

The CFD-based erosion modelling contains three steps: flow modelling, particle tracking, and erosion damage correlated to the particle impact on the surface (Fig. 2.4).

Each step relied on the previous one. Hence, any non-physical result in any step transferred to the next one will affect the final erosion results.

The flow modelling is provided through a CFD based solver where the flow field is simulated to obtain the flow field data (pressure, velocity components, turbulent kinetic energy). In this domain, the N-S equations are solved. Since the calculation of the time-resolved transport quantities (momentum, energy) is computationally expensive, the time-averaged forms of the N-S equations are used to obtain those quantities, but it compromises the accuracy of the turbulent fluctuations calculations. This results in additional unknown variables called Reynolds stresses and consequently, closure equations are needed. These equations are derived from turbulence models which provide flow field predictions for different geometries and conditions with different accuracy. Therefore, the turbulence model selection is important and requires an understanding of the flow characteristics.

Moreover, a CFD discretisation (mesh) sensitivity is required to assure that the flow field prediction is mesh independent. Consequently, the accuracy of the model flow field directly affects the erosion prediction results. Therefore, flow field prediction validation is essential before predicting particle trajectories prediction [65], [66].

In turbulent flow, the fluid velocity is decomposed into mean and fluctuation components. The random velocity fluctuations affect the particle trajectories and particle dispersion is attributed to the fluctuation velocity components, in turbulent particulate flow. The particles dispersion is enhanced by turbulence, and it is the dominant mechanism for regions away from the wall [67], [68]. The trajectories of turbulence affect small particles trajectories more than the large particles. To have a more physical and accurate prediction of particle behaviour, the effect of turbulent fluctuation velocity components on particle trajectories should be considered to improve the accuracy of the particles' behaviour. Many methods have been proposed to calculate the effect of turbulent fluctuations on particles [69], [70], [71], [72], [73], [74], [75], [76].

The third and final step in erosion rate prediction is to transfer the particle impact information into an erosion equation. Each particle impact information is used in the selected erosion equation to calculate surface mass loss from each particle. The overall erosion rate is the summation of all mass losses caused by all particles. A summary of

the CFD-based erosion simulation process is given in Fig. 2.7. For an accurate erosion distribution on the studied geometry surface, a significant particle number is required to be calculated. This number depends on the geometry and flow pattern. In a direct impingement geometry, for instance, the fluid transfers particles towards the wall as it moves. Hence, the necessary particle number required to be calculated is less than that in a sudden contraction/expansion geometry in which the carrier fluid moves in a parallel direction to walls in the straight sections.

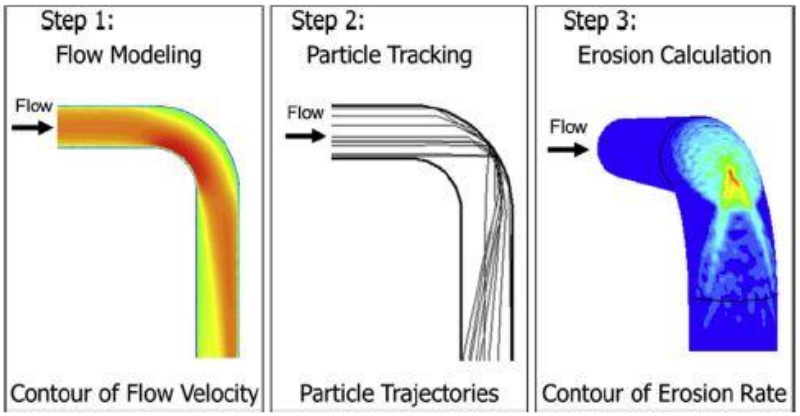

Figure 2.7: Steps of CFD - based erosion prediction **[68]**

Chen et al. [77] utilised the commercial CFD code CFX for the erosion prediction for oilfield applications specifically elbows and plugged tees. The erosion model is based on Ahlert's [78] model where the erosion ratio depends on the particle impact velocity and angle. The study shows that a stochastic rebound model is required to estimate erosion in this simulation. Zhang et al. [79] utilised several rebound models from the literature that were implemented on the commercial CFD code FLUENT. In their work, they investigate the erosion damage prediction in flat specimens in water or airflow and 90^{o} elbows in air. Their models were validated with experimental measurements using an electrical-resistance probe to measure the erosion. Gnanavelu et al. [80] developed a methodology where the universal wear map is generated for the sample material using a jet impingement test. The local wear rate from this is interpreted using a CFD simulation to produce the local wear as a function of the particle impact velocity and angle. Finally, the CFD solution is calculated for different erosion configurations providing the particle impact data at each point on the surface.

Wong et al. [81] used an experimental rig where air-suspended sands flow through an aluminium annular cavity which multi-layer paint erosion and pipe material

loss data attained. Then a complimentary CFD study based on the Lagrangian approach predicted the erosion rate at the forward- and backward-facing steps They observed that erosion rate is more accurate on surfaces experiencing direct impact from particles compared to erosion caused by secondary impacts. Similar cavity structures with expansion and contraction are investigated by Lin et al. [82]. They adopted a URANS (SST)-DPM CFD model to examine different heights between the aft and leading walls of the cavity and they explored the erosion distribution on the downstream bottom walls and the initial erosion positions.

2.5 SUMMARY

On the particle interaction studies, it is indicated the importance of the flow Stokes number as well as the coefficient of restitution of the particle collisions. The present study on the bouncing motion of a spherical particle is compared to the existing literature results. The particle-laden flows are well examined using the analysis of the channel flow with a backward-facing step. A similar analysis is incorporated in this study to discuss the validity of the methodology used and compare the simulation results. The accuracy of the RAS models which is the most efficient turbulent model regarding the computational time is examined. The erosion modelling is reviewed in this chapter. It is shown that there is more than one approach to erosion prediction. These models can predict material removal to some extent. The CFD-based modelling is incorporated to predict the material removal and erosion rates without the need for complicated experiments. These simulations results can provide useful information for the life cycle and serviceability to the pipelines. The simulation modelling is based on the erosion equations that are developed early in the literature and well discussed here. The simulation data are comparable with the experimental data from the associated studies in the literature.

3 Background Modelling Theory

3.1 PARTICLE-PARTICLE AND PARTICLE-FLUID GOVERNING EQUATIONS

3.1.1 Eulerian Framework

In the Eulerian framework, the motion of an incompressible fluid phase in the presence of a secondary particulate phase can be expressed by the volume-averaged continuity equation:

$$\frac{\vartheta a_c}{\vartheta t} + \nabla \cdot (a_c U_c) = 0 \tag{3.1}$$

and Navier-Stokes equations:

$$\frac{\vartheta a_c U_c}{\vartheta t} + \nabla \cdot (a_c U_c U_c) = \frac{1}{\rho_c}\left(-\nabla \mathrm{p} + \nabla \cdot (\rho_c \tau)\right) + a_c g - S_P + F^{cp} \tag{3.2}$$

where ρ_c is the continuous phase density, p is the pressure gradient, α_c is the volume fraction and U_c is the velocity of the continuous phase, respectively, τ accounts for the Reynolds stresses, g the gravitational acceleration and F^{cp} counts for fluid-particle interaction forces [83], [84], [85]. The term S_P is due to the influence of the particles on the fluid. For a given particle P of mass m_P and velocity U_P, the force exerted by the particle on a fluid volume unit is proportional to the particle momentum difference as it enters (t_{in}) and leaves (t_{out}) the control volume. A momentum source contribution is generated by the particle P in each cell during one eulerian timestep dt. The contribution of all the particles which have been in the cell k (of volume V_k) during the eulerian time step dt is written as:

$$S_P@cellk = \frac{1}{V_k dt}\sum m_P((U_P)_{toutcellk} - (U_P)_{tincellk}) \tag{3.3}$$

3.1.2 Lagrangian Framework

In the Lagrangian framework, a particle P is defined by its centre position x_P, diameter D, velocity U_P and density ρ_P. The particle volume is $V_P = (4/3)\pi(D/2)^3$ and its mass $m_P = (\rho_P \pi D^3)/6$. Each particle position vector is calculated from the equation:

$$\frac{dx_P}{dt} = \vec{U}_P \tag{3.4}$$

and the motion of particles is governed by Newton's equations:

$$m_P \frac{d\vec{U}_P}{dt} = \sum F_i \tag{3.5}$$

$$I_P \frac{\omega_P}{dt} = T \tag{3.6}$$

where F_i represent the forces acting on the particle, I_P is the particle moment of inertia and T is the torque acting on a rotating particle due to viscous particle-fluid interactions.

3.1.3 Numerical Solutions

3.1.3.1 Finite volume method discretisation

The Navier-Stokes equations are initially integrated over the whole solution and time domain and then the solution domain is discretised into a given number of cells whilst the time domain is discretised in time steps. All the variables and parameters are designated in the cell centroids. The spatial discretisation (meshing) is built with structured or unstructured cells which fill the whole domain. The time step is controlled by the Courant number which corresponds to the cell portion that the flow will transverse due to advection effects in a time step [86]. This is defined as:

$$Co = \frac{\delta t |U|}{\delta x} \tag{3.7}$$

where δt is the time step, |U| is the velocity magnitude and δx the cells size in the velocity direction. The explicit scheme is used in this study, therefore the Courant number should be maintained as Co < 1 throughout the domain to ensure solution stability.

The generic transport equation for mass and momentum conservation integrated over the control finite volume V_p provides [87]:

$$\left[\frac{\vartheta}{\vartheta t}\int_{V_p} \phi dV + \int_{V_p} \nabla \cdot \left(\vec{U}\phi\right) dV - \int_{V_p} \nabla \cdot (\Gamma \nabla \phi)\, dV\right] = S_\phi(\phi) \tag{3.8}$$

On the left-hand side, the first term is the time gradient, the second the spatial discretisation divergence and finally the third the Laplacian surface normal gradient. On the right-hand side is the source term.

The first-time derivative ($\partial/\partial t$) term discretisation schemes include 1st order transient Euler implicit, 2nd order standard backward implicit difference and 2nd order Crank-Nicolson [88].

For the gradient terms, the default scheme uses the Gauss linear approximation. The Gauss entry indicates the standard finite volume Gauss integration discretisation which interpolates the values from cell centres to face centres. The linear entry indicates a linear interpolation and is referred to as central differencing. A limiter is used to constrain the gradient so that the face values remain in the bound of values in surrounding cells when cell values are extrapolated to faces [87].

The divergence terms represent convective processes are based on Gauss integration and the advected field is interpolated to cell faces using one of the following schemes:

- upwind: 1st order bounded (not too accurate)
- linear: 2nd order unbounded
- linearUpwind: 2nd order unbounded and upwind – biased. The velocity gradient discretisation needs to be specified.
- LUST: mixed scheme of 75% linear and 25% linearUpwind. Also, the velocity gradient requires to be specified.
- limitedLinear: a linear scheme that limits towards upwind in rapidly gradient change regions.

The bounded term for the above refers to the material time derivative treatment given in spatial time derivative and convection. The divergence terms can be expressed using the Gauss theorem as:

$$\int_{V_P} \nabla \cdot \left(\vec{U}\phi_P\right) dV = \sum_f S \cdot \left(\vec{U}\phi\right)_f \tag{3.9}$$

The face value term φ_f includes the φ cell gradient in adjacent volume which denotes the 2nd order linear upwind approach [89].

The Laplacian terms contain the diffusion term in the momentum equations ($\nabla \cdot (\nu \nabla U)$). The only discretisation scheme available is the Gauss scheme which is in the form of:

$$\int_{V_P} \nabla \cdot (\Gamma \nabla \phi_P) dV = \sum_f \Gamma_f S \cdot (\nabla \phi)_f \tag{3.10}$$

$$S \cdot (\nabla \phi)_f = \frac{|S|(\phi_E - \phi_P)}{|d|} \tag{3.11}$$

where d is the vector of the distance between the computational centres E and P and S is the outward normal to the surface vector. The formulation above represents the 1st order accurate Laplacian calculation.

3.1.3.2 DPM Solver

The Euler-Lagrange solver selected for this study is the DPMFoam which is a standard solver of OpenFOAM. It is described as a transient solver for the coupled transport of a single kinematic particle cloud including the effect of the volume fraction of particles on the continuous phase with the particle-particle collisions. In the case of a single particle, the pair collision is described by the particle-wall model. The transient solver solves for instant-of-time variables. The flow chart of the DPMFoam is given in Fig. 3.1.

The solver utilises the lagrangian library coupled with the PIMPLE algorithm to solve the continuous (Eulerian) phase. The sequence of the solver is as follows: the velocity and position of the particles are calculated from the Lagrangian tool and this information passes to the Eulerian code. The particles are located within the Eulerian grid and the cell ID of each particle (centre) is allocated. The calculation of the particle volume fraction follows and along with the boundary conditions, the particle forces are calculated. The force data are transferred back to Lagrangian code to compute the particle velocity field for the next time step [90].

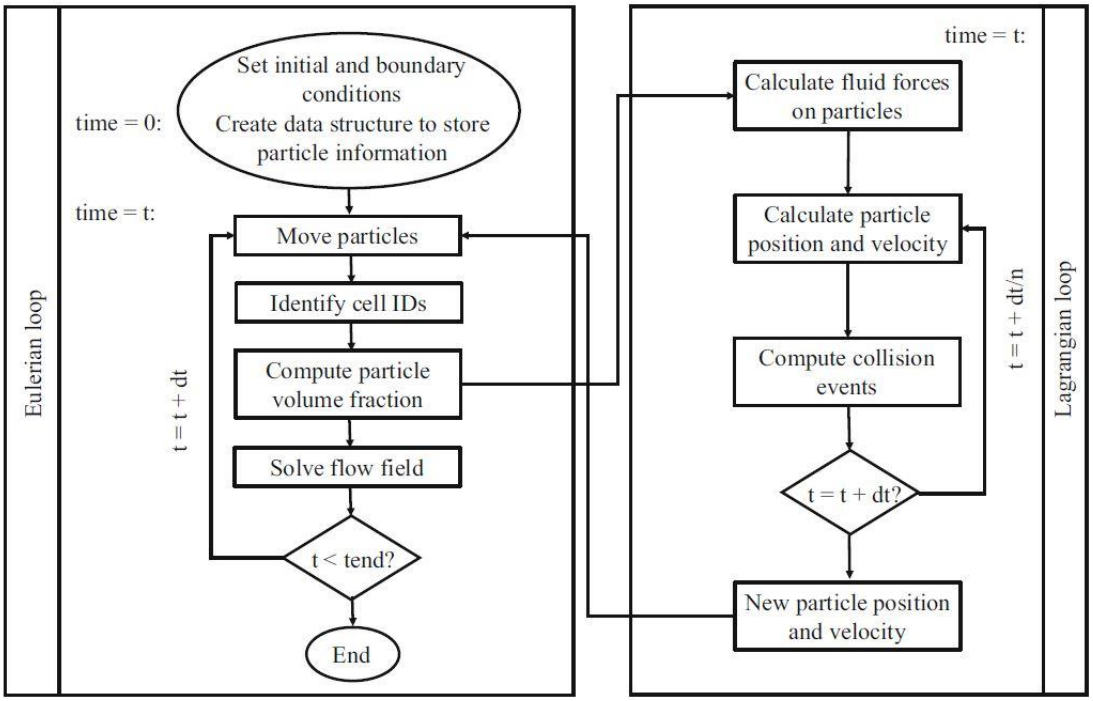

Figure 3.1: DPMFoam Flow Chart **[90]**

3.1.3.3 PIMPLE and Algorithm Controls

The DPM solver is based on the PIMPLE algorithm to solve the pressure-velocity coupling. This is merging the Pressure Implicit Splitting Operator (PISO) [91] and Semi-Implicit Method for Pressure-Linked Equations (SIMPLE) [92] algorithms which allow transient solutions. With the SIMPLE algorithm, the pressure on a mesh point is calculated from velocity components by coupling the N-S equations iteratively. The PISO algorithm is applied to remedy the pressure-velocity correction [93]. In this variation of PISO outer corrections and equations under relaxation between outer correctors are implemented for increasing stability [87]. The flowchart of the PIMPLE algorithm is shown in Fig. 3.2.

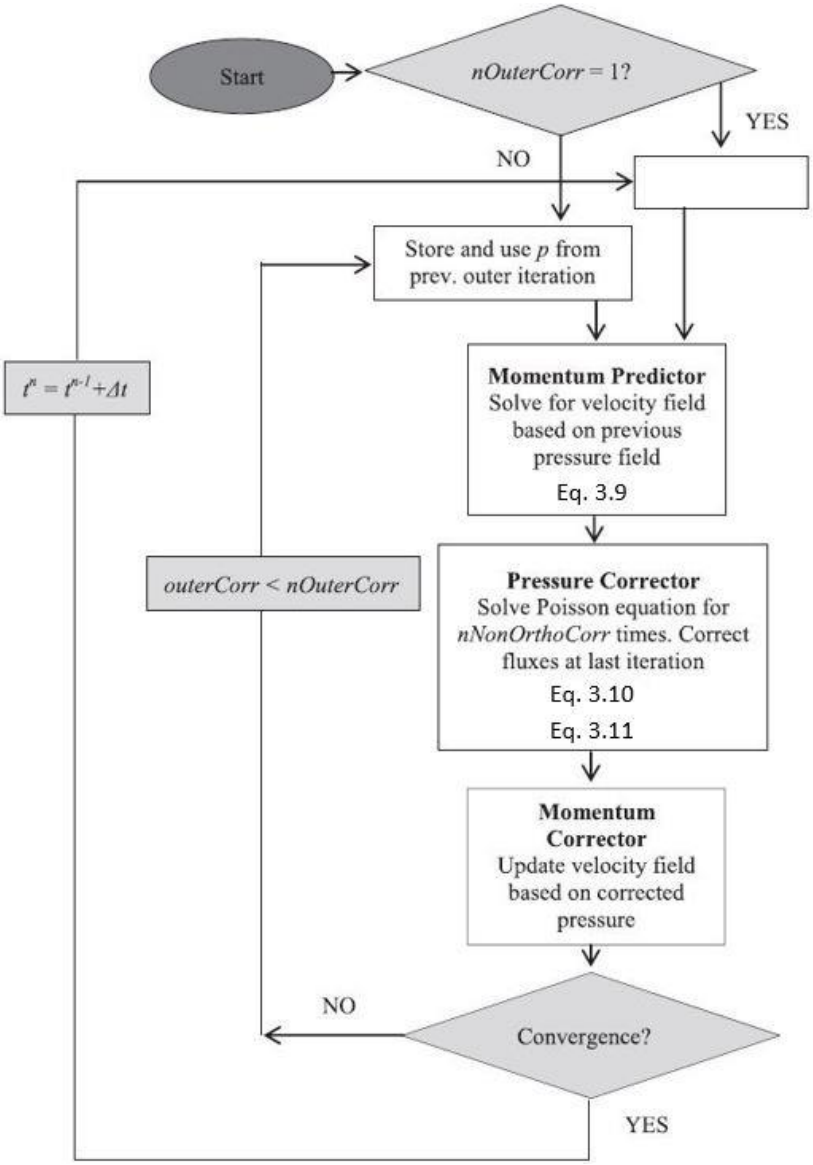

Figure 3.2: PIMPLE flowchart as used in OpenFOAM. nOuterCorr is the number of outer corrector loops; nNonOrthoCorr is the number of non – orthogonal pressure corrector loops **[87]**

The control of the solution is achieved using preconditioners which improve the solution convergence. Thus, for a system [A]{x} = {b} the preconditioner uses a matrix [*M*] which resulting a new system $[M]^{-1}[A]\{x\} = [M]^{-1}\{b\}$. The smoothers are used to reduce the dependence of the iterations number on mesh type.

There is a range of options for the matrices preconditioning in the conjugate gradient solvers. The algorithms used here are the simplified Diagonal-based Incomplete Cholesky symmetric/asymmetric (DIC/DILU) and the Geometric agglomerated Algebraic Multi-Grid (GAMG) preconditioners. The latter generates a quick solution on a small cell mesh domain and mapping this solution to a finer mesh

and using it as an initial guess for achieving an accurate solution. Generally, it is faster than other solutions, therefore it is the first choice for solution control. The available smoothers include the Gauss-Seidel, DIC/DILU and the combination of both smoothers. The symmetric Gauss-Seidel smoother works for a range of applications for reducing residuals [90].

3.1.4 Properties of the Dispersed Phase

3.1.4.1 Volume Fraction

The volume fraction concept is applied to the dispersed phase. Consider a mixture volume containing some dispersed elements. The number density is defined as $n \approx \Delta N/\Delta V_m$ (where ΔN is the number of elements), so subsequently defining as ΔV_{mo} the volume where variations are eliminated, the number density is given by [8]:

$$n = \lim_{\Delta V \to \Delta V_{mo}} \frac{\Delta N}{\Delta V} \tag{3.12}$$

The volume fraction of the dispersed phase is defined as:

$$a_d = \lim_{\Delta V \to \Delta V_{mo}} \frac{\Delta V_d}{\Delta V} \tag{3.13}$$

where V_d is the dispersed volume into the mixture volume V. Similarly, the continuous phase volume fraction V_c is defined as:

$$a_c = \lim_{\Delta V \to \Delta V_{mo}} \frac{\Delta V_c}{\Delta V} \tag{3.14}$$

By definition, the sum of continuous and dispersed volume fractions is equal to unity, thus:

$$a_c + a_d = 1 \tag{3.15}$$

3.1.4.2 Response Time

The response time of a particle is the time required for a particle to react to flow velocity or temperature changes. Therefore, the corresponding response times can be defined. Starting with the momentum response time, the (spherical) particle motion equation is used:

$$m\frac{dv}{dt} = \frac{1}{2}C_D\frac{\pi D^2}{4}\rho_C(u-v)|u-v| \Rightarrow m\frac{dv}{dt} = \frac{1}{2}C_D\frac{Re_r}{24}(u-v) \qquad (3.16)$$

where C_D is the drag coefficient and with particle Reynolds number defined as $Re_r = \rho_C D|u-v|/\mu_C$.

Eq. 3.16 can be rewritten by dividing with the particle mass, so that:

$$\frac{dv}{dt} = \frac{18\mu_C}{\rho_C D^2}\frac{C_D Re_r}{24}(u-v) \qquad (3.17)$$

For Stokes flows (low Re_r), the term $C_D Re_r/24$ approaches unity. The first term has reverse time units; therefore, the momentum response time is defined as [8], [94]:

$$\tau_V = \frac{\rho_C D^2}{18\mu_C} \qquad (3.18)$$

Solving Eq. 3.17 for constant u and Stokes flow, the particle velocity is given as:

$$v = u\left(1 - e^{-t/\tau_v}\right) \qquad (3.19)$$

As shown in the graphical illustration of the particle response time (Fig. 3.3), the time required for a stagnated particle to achieve 63% $(e-1/e)$ of the free stream velocity when is released is the momentum response time [8].

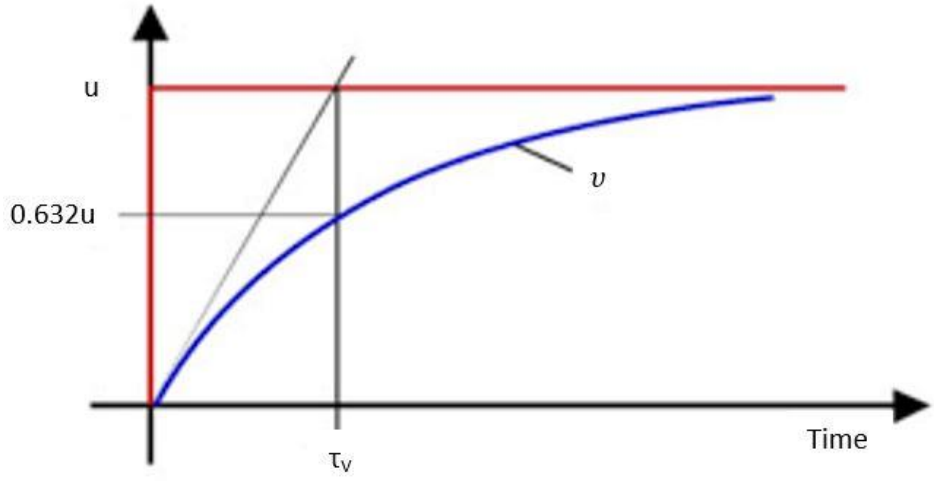

Figure 3.3: Graphical illustration of the particle response time **[95]**

3.1.4.3 Dilute and Dense Flows

A dispersed phase flow can be described as dilute or dense depending on the dominant forces. In dilute flow, the particle motion is controlled by fluid forces (lift and drag), whereas in the dense flow the particle motion is controlled by the collisions and contacts. The defining parameter for the qualitative estimation is the ratio of the particle moment response time (τ_V) to the time between collisions (τ_C). A dilute flow is considered when:

$$\frac{\tau_V}{\tau_C} < 1 \tag{3.20}$$

Obviously, when $\tau_V/\tau_C > 1$ the flow is considered as dense. In that case, the particle has not got sufficient time to respond to the local fluid force before the next collision.

A general indicator for the flow description is the particle volume fraction magnitude α_d as shown in Fig. 3.4. For a volume fraction $a_d < 0.001$, the flow can be considered as dilute where the particles have no influence on the fluid flow and can be neglected as they are transported by the flow. For volume fractions between 0.001 and 0.1 the flow is regarded as dense and collision forces are dominant. Above that limit flow is also contact-dominated and may include all three types of regimes.

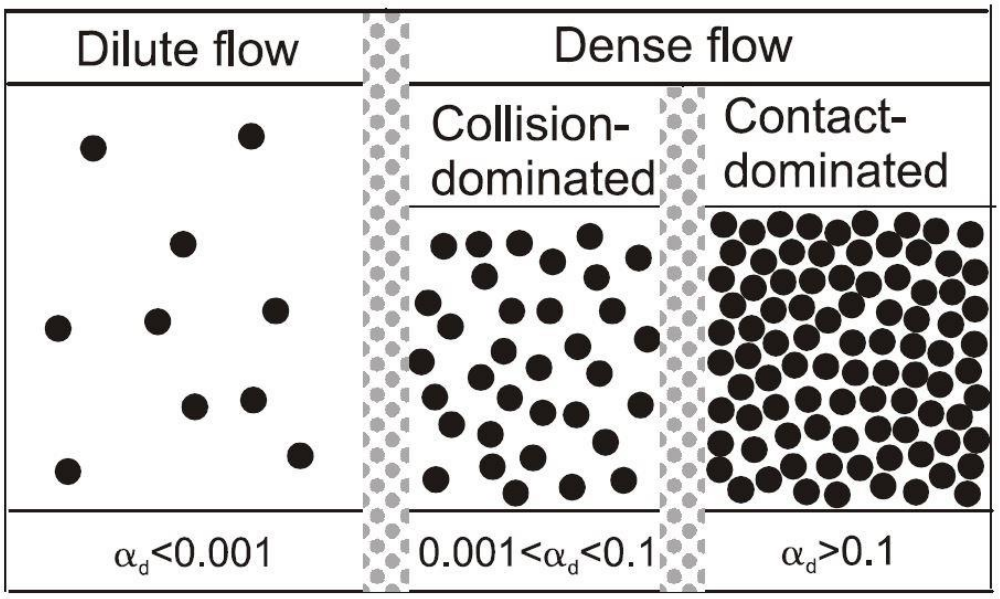

Figure 3.4:Dilute and dense flow regimes **[8]**

3.1.4.4 CFD-DEM coupling

The phase coupling mechanism is very important for the analysis of multiphase flows and influences the behaviour of continuous and dispersed phases. There are three coupling types: one-way coupling: where only the continuous phase affects the other, two-way coupling where there is a mutual effect of both phases on each other and four-way coupling wherein also the particle-particle interactions are taken into account. In this study, two-way coupling is the major mechanism of the flow analysis [8], [96]. The phase coupling classification is shown in Fig. 3.5:

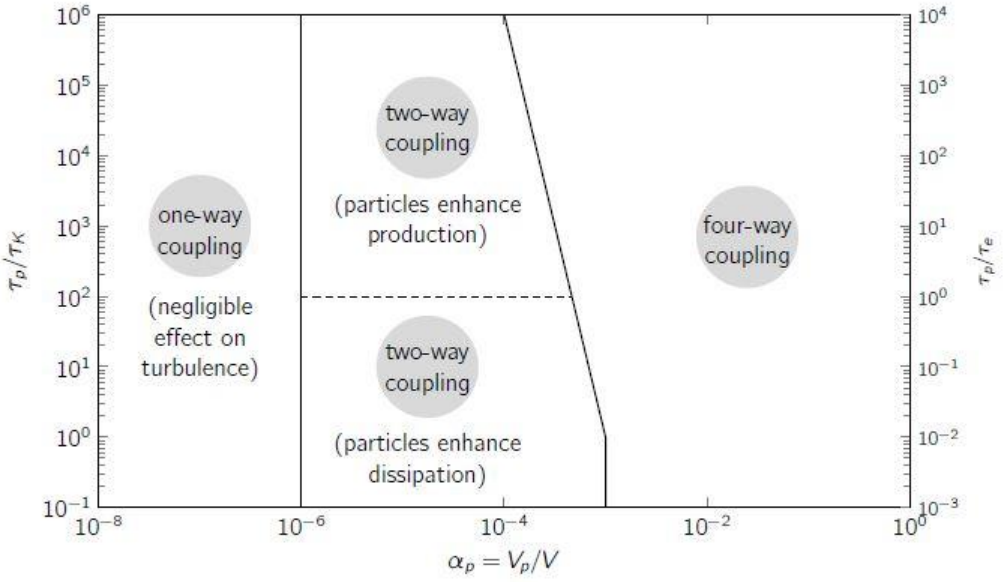

Figure 3.5: Phase coupling classification **[97]**

3.1.4.5 Unresolved CFD-DEM Method

Recently, the discrete particles have been utilised to model granular media in multi-phase flow small-scale simulations. Even though this method fully resolves the flow around each particle they have limited application due to the high computational requirements. An intermediate approach is the unresolved CFD-DEM coupled method with discrete particles where the flow around the particles remains unresolved. With the particle size small compared to the mesh resolution, the computational time is decreased significantly. The DEM part resolves the particles contrasting the CFD part and the volume-averaged Navier-Stokes equations are used.

While fine meshes are generally required for a reasonable fluid interfaces resolution, this is not possible in the unresolved CFD-DEM method. If the cell size is

quite small the void fraction field may become discontinuous leading to numerical instability [98]. It is reported that inaccuracies in the void fraction calculations result in artificial, local pressure fluctuations in the CFD field which can be captured from the structure of motion fluid equations. Therefore, any numerical noise created by the void fraction calculation immediately converts into unphysical pressure field fluctuations [99].

3.1.5 Particle Forces

A rigorous derivation of the motion equation for small particles in non-uniform, unsteady flows at low Reynolds numbers was performed by Maxey and Riley in 1983 [7] and results in:

$$m\frac{\vec{u}_i}{dt} = F_G + F_{UF} + F_D + F_{VM} + F_B \tag{3.21}$$

where:

F_G	the gravitational force
F_{UF}	the pressure shear stress due to undisturbed flow
F_D	the steady-state drag force
F_{VM}	the virtual (added) mass term
F_B	the Basset (history) term

The forces applied to a particle and its directions are given in Fig. 3.6.

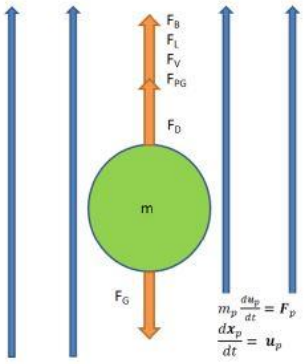

Figure 3.6: Forces applied on a particle

3.1.5.1 Drag Force

The phase coupling mechanisms are strongly influenced by the behaviour of both phases. This is determined by the volume fraction α. For a dilute flow ($\alpha < 0.001$) the particle motion is controlled by the fluid flow alone and less influenced by particle motion. On a dense flow ($0.001 < \alpha < 0.1$) the particle motion is controlled by collisions.

In a dilute flow, the dominant forces acting on a particle are drag and gravity.

$$\sum F = F_D + m_P g \tag{3.22}$$

The drag force for a spherical particle is given by:

$$F_D = \frac{1}{2}\rho_C C_D A|u_i - v_i|(u_i - v_i) \tag{3.23}$$

or

$$F_D = 3\pi\mu_C D(u_i - v_i) \tag{3.24}$$

where: F_D is the total drag force, ρ_C the continuous (fluid) phase density, A the particle area, u_i the continuous phase velocity, v_i the particle velocity, μ_C the continuous phase dynamic viscosity and D the particle diameter.

The drag coefficient for increasing Reynolds number is higher than Stokes drag because the inertial forces becoming more important. With increasing Reynolds number (~100), the flow begins to separate and form vortices behind the sphere. These vortices increase the pressure drop, therefore the form drag increases. For the region $10^3 \leq Re_r \leq 10^5$ the drag is almost entirely form drag and the curve is almost flat at a constant value of 0.445 of Newton's drag law curve (Fig. 3.7).

$$C_D = \begin{cases} \dfrac{24}{Re_r}\left(1 + \dfrac{Re_r^{2/3}}{6}\right) & 0 \leq Re_r \leq 1000 \\ 0.424 Re_r & 1000 \leq Re_r \leq 3 \times 10^5 \end{cases} \tag{3.25}$$

At the critical Reynolds number ($Re_r \sim 3\times10^5$) the boundary layer becomes turbulent and the separation point is moved rearward, sharply reducing the form drag and decreasing the drag coefficient. This phenomenon is entirely due to boundary layer effects.

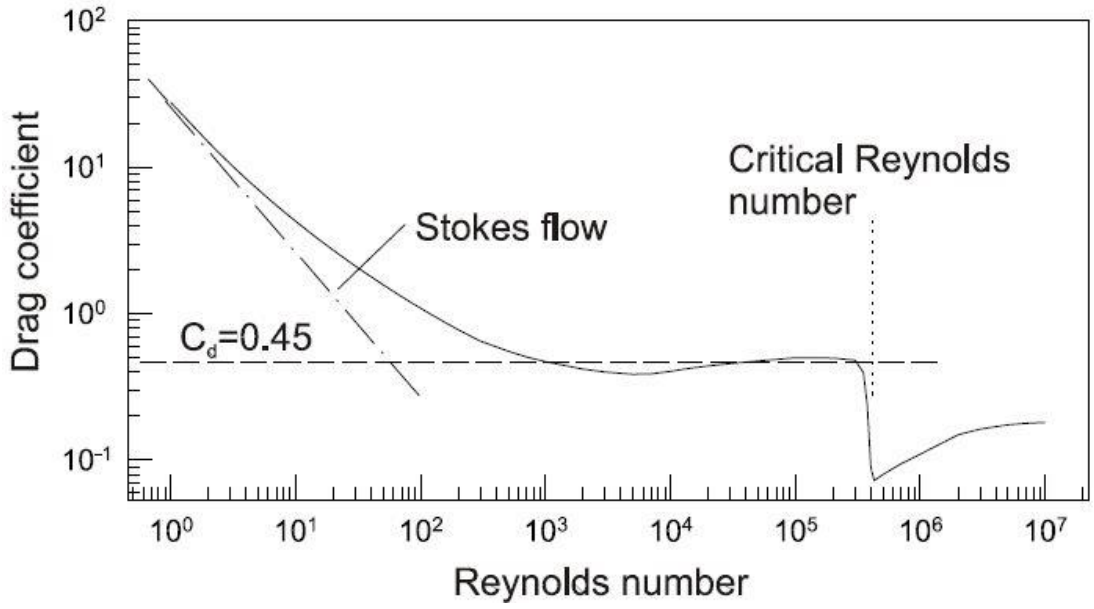

Figure 3.7 Drag coefficient as a function of Reynolds number for a flow around a sphere **[8]**

3.1.5.2 Lift Force

The lift forces applied to a particle are due to its rotation. The rotation may be caused by the velocity gradient or surface effects such as the rebound on a wall. The two primitive lift force models are the Saffman and Magnus.

The Saffman-Mei lift force which is used in this study is developed due to the velocity gradient where the higher velocity on the top of the particle gives rise to low pressure, combined with the high pressure on the low-velocity side results in a lift force [100], [101], [102]. The Saffman-Mei lift force is given by:

$$F_{s,i} = \frac{m_P}{\rho_P}\frac{D}{2}\rho_C C_l(u_i - v_i) \times (\nabla \times u_i) \tag{3.26}$$

where C_l is the lift force coefficient and given by:

$$C_l = \frac{3}{2\pi\sqrt{Re_G}} C_{ld} \tag{3.27}$$

In Eq. (3.27) the Re_G represents the shear Reynolds number and C_{ld} the ratio F_L/F_{Saff} which accounts for the Reynolds number effects. The two parameters are defined as:

$$Re_G = \frac{\rho_C |\nabla \times u_i| D^2}{\mu} = \frac{D^2}{v_C}\frac{du}{dy} \tag{3.28}$$

$$C_{ld} = \begin{cases} 6.46f & Re_r \leq 40 \\ 6.46 \times 0.00524\sqrt{\beta Re_r} & Re_r > 40 \end{cases} \tag{3.29}$$

where:

$$\mathrm{a} = 0.3314\sqrt{\beta} \tag{3.30}$$

$$\beta = 0.5\frac{Re_G}{Re_r} \tag{3.31}$$

$$f = (1 - \mathrm{a})e^{(-0.1Re_r)} + \mathrm{a} \tag{3.32}$$

3.1.5.3 Virtual Mass Force

Due to a body acceleration through a fluid, there is a corresponding fluid acceleration which is at the expense of body work done. This additional work can be formulated as a virtual (or added) mass effect. Anderson and Jackson [103] have shown that the acceleration of the fluid should be represented by the substantial derivative. Thus, the virtual mass force acting on the particle is given by:

$$F_{vm,i} = \frac{\rho_c V_d}{2}\left(\frac{Du_i}{Dt} - \frac{dv_i}{dt}\right) \tag{3.33}$$

This force is also called the apparent mass force because it is equivalent to adding a mass to the sphere. It was proposed that the above equation be multiplied by a coefficient, C_{vm} to correct the virtual mass term. Kafui et al. [104] suggested an empirical correlation for C_{vm}, as a function of the acceleration parameter. This correlation was developed from data using a sphere in simple harmonic motion.

More recently research from Michaelides and Roig [105] suggests that C_{vm} is not a function of the acceleration parameter and should be taken as unity therefore C_{vm}= 1.

3.1.5.4 Undisturbed flow

The undisturbed flow force accounts for the effects of the pressure and shear stress fields on the volume occupied by the particle and contributes to the total forces on the particle. The corresponding force of the pressure field $F_{p,i}$ is a buoyant force

equal to the fluid weight displaced and the force due to the viscous stresses $F_{\tau,i}$ depends on the shear stress tensor τ_{ij} in the external flow to the particle [8], [106]. The total force due to the undisturbed flow is:

$$F_{UF} = F_{p,i} + F_{\tau,i} = V_d \left(-\frac{\vartheta p}{\vartheta x_i} + \frac{\vartheta \tau_{ij}}{\vartheta x_j} \right) \tag{3.34}$$

The effect of this force is not significant when the material density ratio is less than 0.001 [8]. This term is not applied in the computational analysis in this study.

3.1.5.5 Basset Force

The Basset force accounts for the viscous effects and addresses the temporal delay evolution in the particle boundary layer as the particle relative velocity changes with time. This force decays as the particle motion reaches to equilibrium condition like constant velocity. It is also called the history force [8] [106]. A general form of the Basset force is given as [8]:

$$F_B = \frac{3}{2} D^2 \sqrt{\pi \rho_C \mu_C} \int_0^t \frac{\frac{d}{dt'}(u_i - v_i)}{\sqrt{t - t'}} dt' \tag{3.35}$$

where D is particle diameter, ρ_c and μ_c are the continuous phase density and viscosity, u_i and υ_i are the continuous and particle velocity, respectively and t´ is the time step. This term is difficult to evaluate, and it is insignificant in some applications (usually when the particle diameter is less than 10μm) [8]. In this study, this term is not considered.

3.2 COLLISION THEORY

3.2.1 Particle-wall interactions

There are two considerations for a particle-wall interaction: hydrodynamic interaction due to the proximity of a wall and mechanical interaction caused by contact with the wall. An example of hydrodynamic interaction is the Saffman lift force due to the velocity gradient near the wall. Another example is the fluid force acting on a particle approaching the wall in the normal direction due to the displacement of the fluid film between the particle and the wall.

The treatment of the mechanical behaviour associated with particle-wall interaction depends on the inertia of the particle. When a massive particle collides with a wall, it rebounds but loses kinetic energy due to inelasticity effects. For a very small particle approaching a wall, molecular forces become dominant compared with the inertial force. As a result, the particle is captured by the wall due to cohesive forces, and neither rebounds from nor slides along the wall. This cohesive force is identified as the van der Waals force [8].

There are two models used to deal with particle-wall and particle-particle collisions, the hard-sphere model and the soft-sphere model. The hard-sphere model is based on the integrated forms of the equations of motion, namely the impulsive equations, and instantaneous deformation of the particle does not appear in the formulation explicitly. In the soft sphere model, the instantaneous motion during the whole collision process is obtained [8].

The soft sphere model considers momentum and displacement variations for arbitrary times to solve the differential equations. The model is equivalent to a spring-dashpot-slider (Fig. 3.8) where the following parameters are considered: stiffness k, damping coefficient η and friction coefficient f. The parameter δ_n is the overlap displacement when two particles collide and then deform. In the case of the particle-wall collision the particle j is replaced by a rigid wall w where particle i remains as is.

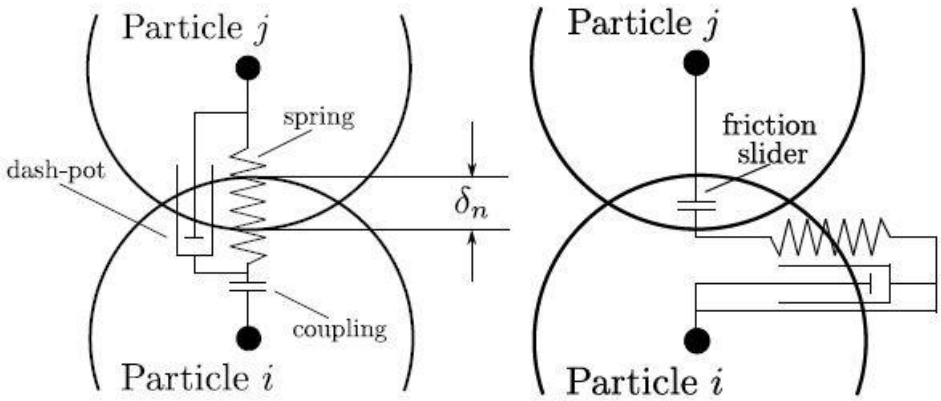

Figure 3.8: Schematic description of the spring - slider - dashpot model for normal (left) and tangential (right) forces

The normal and tangential contact force components are given below [107], [8], [90]:

$$F_{n,iw} = \left(-k_n \delta_n - \eta_{nw} U_{iw}^p \cdot n\right) n \tag{3.36}$$

$$F_{t,iw} = -k_t \delta_t - \eta_{tw} U_{siw}^p \tag{3.37}$$

where δ_n, δ_t is the normal and tangential force particle displacement, respectively; n is the unit vector from the centre of particle i to wall, U_{iw} is the velocity vector of particle i relative to wall w and U_{siw} is the slip velocity of the contact point and given by:

$$U_{s,iw}^p = U_{iw}^p - \left(U_{iw}^p \cdot n\right) + r(\omega_i \times \omega_j) \times n \tag{3.38}$$

where r is the sphere radius, ω_i is the rotational velocity of particle i ($\omega_j = 0$ in case of a wall). If the equation below (Eq. 3.39) is satisfied:

$$\left|F_{t,iw}\right| > \mu \left|F_{n,iw}\right| \tag{3.39}$$

then Eq. 3.37 changes to:

$$F_{t,iw} = -\mu\left(-k_t \delta_t - \eta_{tw} U_{s,iw}^p\right) t_{ij} \tag{3.40}$$

where t_{ij} is the tangential unit vector ($t_{ij} = U_{s,iw}/|U_{s,iw}|$).

3.2.2 Stiffness

Based on Hertzian contact theory the normal force is equal to:

$$P_n = k_n \delta_n^{3/2} \tag{3.41}$$

The equation of the normal stiffness component k_n for the contact between a sphere and wall is given by:

$$k_n = \frac{4/3\sqrt{\alpha}}{\frac{1-\nu_s^2}{E_s} + \frac{1-\nu_w^2}{E_w}} \tag{3.42}$$

where E_s and ν_s are Young's modulus and Poisson's ratio for the particle, respectively; E_w and ν_w are the same parameters for the wall. That implies that the force and displacement are non-linear, therefore Eq. 3.36 is replaced by:

$$F_{n,iw} = \left(-k_n \delta_n^{3/2} - \eta_{nw} U_{iw}^p \cdot n\right) n \tag{3.43}$$

As above, the tangential force, for the case of no-slip, is equal to:

$$P_t = \frac{2\sqrt{2r}G_s}{2-\nu_s}\delta_n^{1/2}\delta_t \tag{3.44}$$

The equation of the tangential stiffness component K_t for the contact between a sphere and wall is given by:

$$K_t = \frac{8\sqrt{r}G_s}{2-\nu_s}\delta_n^{1/2} \tag{3.45}$$

where G_s is the shear modulus and related to Young's modulus and Poisson's ratio by:

$$G_s = \frac{E_s}{2(1+\nu_s)} \tag{3.46}$$

3.2.3 Damping Coefficient

The damping coefficient η is related to a constant α_{dc} which correlates to the coefficient of restitution ε (Fig. 3.9) and is given by the following expression (in the normal direction):

$$\eta_n = \alpha_{dc}\sqrt{mK_n}\delta_n^{1/4} \tag{3.47}$$

The coefficient of restitution ε for a collision is defined as the ratio of the post-collision velocity $V^{t_c^+}$ to the pre-collision velocity $V^{t_c^-}$ so that:

$$\varepsilon = \frac{V^{t_c^+}}{V^{t_c^-}} \tag{3.48}$$

The damping coefficient in the tangential direction η_t is assumed to be equal to the normal η_n [107].

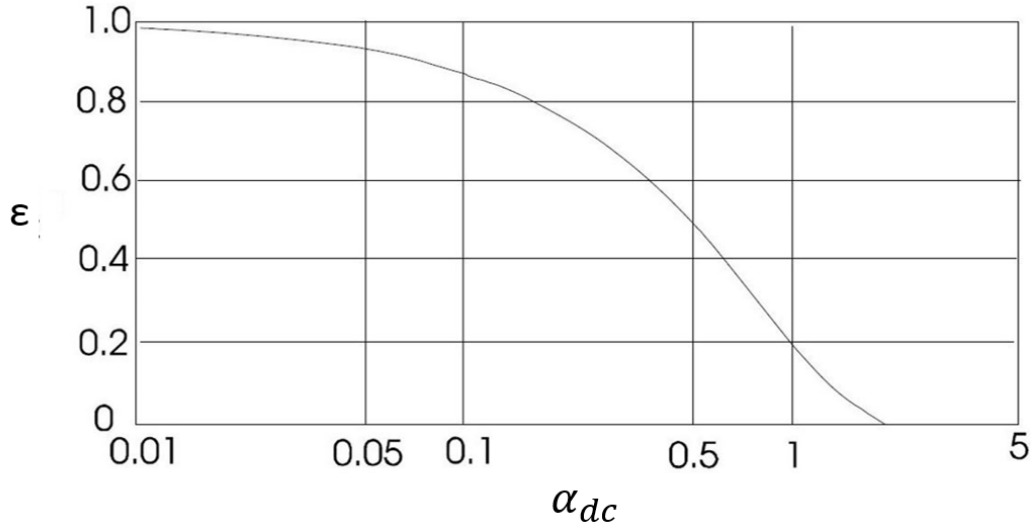

***Figure 3.9: Relation between constant α_{dc} and coefficient of restitution ε* [107]**

3.3 TURBULENCE MODELLING

3.3.1 Wall Functions

Into the boundary layer structure, the velocity and other turbulent quantities gradients differ largely from the core flow gradients. In a mesh grid, these gradients will be approximated using discretisation procedures which are not suitable for such high variation since they usually assume linear interpolation of values between cell centres. Moreover, in two-equation models, additional quantities require specification of their boundary conditions which is difficult to be specified.

The wall functions are used to overcome such difficulties. There are many wall-treatment options, however there are two major approaches: the Low Reynolds Number (LRN) treatment and the High Reynolds Number treatment (HRN) (Fig. 3.10).

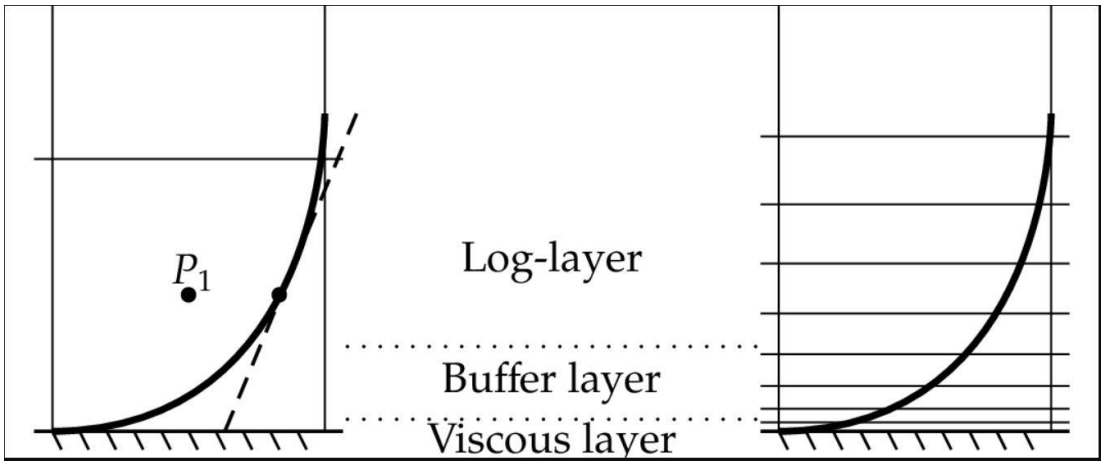

Figure 3.10: HRN (left) and LRN (right) treatments. The HRN uses log-law to estimate cell gradient

LRN integrates the turbulence on the wall down to the viscous sublayer where the first computational cell must have its centroid ($y^+ \approx 1$). This results in very fine meshes close to the wall, which means substantial computational requirements.

HRN approach uses wall functions to model the turbulence near the wall. This method relies on the log-law velocity profile, therefore the centroid of the first cell can be placed in the log sublayer. The HRN technique enhances solution convergence and numerical stability [23].

However, none of these approaches can deal with the buffer layer, therefore the first computational cell should be either in the viscous sublayer or in the log-layer. To understand better the near-wall region, the two important parameters to quantify the boundary layer are the dimensionless wall distance y^+ and friction velocity u_T [108].

$$y^+ = \frac{y \times u_T}{\nu} \tag{3.49}$$

$$u_T = \sqrt{\frac{\tau_w}{\rho}} \tag{3.50}$$

where τ_w is the wall shear stress, y is the distance to the wall and v is the fluid viscosity. The non-dimensional friction velocity is defined as:

$$u^+ = \frac{u}{u_T} \tag{3.51}$$

The near-wall boundary layer is divided into three regions:

- Viscous sublayer ($y^+ < 5$): in that sublayer, the fluid is dominated by the viscous effect, therefore the fluid shear stress is assumed equal to the wall shear stress.

$$u^+ = y^+ \tag{3.52}$$

- Buffer sublayer ($5 < y^+ < 30$): Viscous and turbulent stresses are of similar magnitude and since it is complex velocity profile is not well defined. In this area, small-scale turbulence of high energy is generated by sheared flow instability, and there is a sharp peak in the conversion of mean-flow kinetic energy to turbulent kinetic energy and turbulent energy dissipation. It is also called the turbulence-generation layer. The produced turbulence is carried outward into the broad outer layer of flow and inward into the viscous sublayer [109].
- Logarithmic sublayer ($30 < y^+ < 200$): in this region, the turbulence stress dominates the flow and velocity profile varies very slowly with a logarithmic function along the wall distance y, so that:

$$u^+ = \frac{1}{\kappa} \times \ln(Ey^+) \tag{3.53}$$

where $\kappa = 0.41$ is the von Karman constant and $E = 9.8$ constant for smooth walls.

In OF, the wall functions calculate the κ, ω and ν parameters for each cell in the wall region. There are a few schemes available in the OF library. Here the ones used will be described for the k and ω values.

The *kLowReWallFunction* provides a turbulence kinetic energy boundary condition for low- and high- Reynolds number turbulent flow cases. The y^+ parameter is calculated from friction velocity u_T through:

$$u_T = C_\mu^{0.25}\sqrt{k} \tag{3.54}$$

where the k is the turbulence kinematic energy in the cell centre adjacent to the wall and $C_\mu = 0.09$ a constant.

Next, the non-dimensional parameter k^+ is calculated from:

$$k^+ = \frac{C_k}{k} \times \log(y^+) + B_k \tag{3.55}$$

where C_k = 0.416 and B_k = 8.366 constants.

From k^+, the turbulence kinematic energy k on the wall is derived as:

$$k = k^+ \times u_T^2 \tag{3.56}$$

As discussed, the omega wall function provides the combination of viscous and log equations. The *omegaWallFunction* is a special wall function that can switch between viscous and logarithmic regions depending on the y^+ value. In the intersection of the two regions, the ω value is calculated by blending the viscous and log-law sublayer value.

$$\omega = \sqrt{\omega_{vis}^2 + \omega_{log}^2} \tag{3.57}$$

where ω_{vis} and ω_{log} are the equations for the viscous sublayer and logarithmic sublayer, respectively [108].

$$\omega_{vis} = \frac{6\nu}{\beta_1 y^2} \tag{3.58}$$

$$\omega_{log} = \frac{k^{0.5}}{C_\mu^{0.25} k y} \tag{3.59}$$

where ν is the fluid kinematic viscosity, β_1 = 0.075 a turbulence constant, y is the distance from the wall to the centroid of the cell adjacent to it and κ is the von Karman constant [110].

3.3.2 Boundary Conditions

The k-ω model involves the transport equations for the turbulence kinetic energy k and the specific turbulence dissipation rate ω. The boundary values for these parameters are derived from the turbulence intensity and the geometry characteristic length and are given from the following equations.

$$k = \frac{3}{2}\left(I U_{ref}\right)^2 \quad (m^2/s^2) \tag{3.60}$$

$$\omega = \frac{k^{0.5}}{C_\mu L} \qquad (s^{-1}) \tag{3.61}$$

where k is the turbulence kinetic energy, ω the turbulence kinetic dissipation, I the turbulence intensity (typical values 5-10%), U_{ref} the medium velocity, C_μ the turbulence constant (= 0.09) and L the turbulence characteristic length scale.

The relative turbulence intensity I is defined as:

$$I = \frac{\sqrt{\overline{\overline{u'^2}}}}{|u_i - v_i|} \tag{3.62}$$

where $\sqrt{\overline{\overline{u'^2}}}$ is the root mean square of the carrier fluid turbulence fluctuations, u_i and v_i is the carrier fluid and disperse phase mean velocities, respectively. The relative turbulence intensity is augmented as the relative velocity between the carrier and dispersed phases are reduced.

The turbulence length scale is the other parameter used to quantify the turbulence effects. There is a spectrum of turbulence length scales in the turbulence flows. The smallest length scale is the Komolgorov length scale. For particles smaller than the Komolgorov length scale, the primary effects are probably those due to unsteady flow and flow field curvature. The length scale ratio which has been the subject of experimental investigation [111] is L_x/D where L_x is the turbulence macroscale. Generally, for non-circular geometry, the turbulence length scale is given by $0.07d_h$, where d_h is the hydraulic diameter [8].

As k, ε and ω are elliptic by means of the diffusion term [19], the following geometry boundary condition should be defined:

- Inlet: k, ε and ω distributions are given
- Outlet: $\partial k/\partial n$ and $\partial \varepsilon/\partial n$
- Free stream k, ε and ω are given or $\partial k/\partial n$ and $\partial \varepsilon/\partial n$
- Solid walls: depending on the approach (HRN or LRN)

3.4 EROSION MODELLING

3.4.1 Finnie Model

The Finnie model is briefly described in the erosion literature review. Here a more analytical development of this model is given. A starting point of this model is a single rigid abrasive particle hits a ductile material in an impact angle so that it displaces or cuts away part of the surface. A first indication that erosion occurs is the crater or scratch created by the particle. Usually, shallow impact angles produce erosion which is of greater interest for crater's the length/depth of ratios about 10:1 and leads to the idealised cutting condition as shown in Fig. 3.11.

The ratio of the vertical force component on the particle face to the horizontal force component is assumed as a constant value K. This can be satisfactory if a geometrically similar configuration is maintained meaning that the particle rotation should be significantly small during cutting. Therefore, the ratio of depth contact *l* to the depth of cut y_t (Fig. 3.11) has a constant value ψ. Additional assumptions include that the particle cutting face width is uniform and large compared to the depth of cut (plane strain). Also, the constant plastic flow stress p is reached immediately upon impact. This value will be further discussed later. Once these assumptions have been made, the particle motion equations can be written down and solved in the x, y and φ directions to determine the coordinates of the particle tip x_t and y_t over time.

The surface material volume removed from the impact is taken as the product of the area swept out by particle tip and the width of the cutting face [44]. To determine the time at which cutting stops we assume that for low angles a, the cutting ceases when the particle tip leaves the surface ($y_t = 0$). For higher impact angles α, the cutting stops when $dx_t/dt = 0$ as the horizontal motion of particle tip may stop before it leaves the surface. Therefore, the volume of material removed ε_{VP} by a single abrasive grain can be obtained by integration over the cutting period [44]:

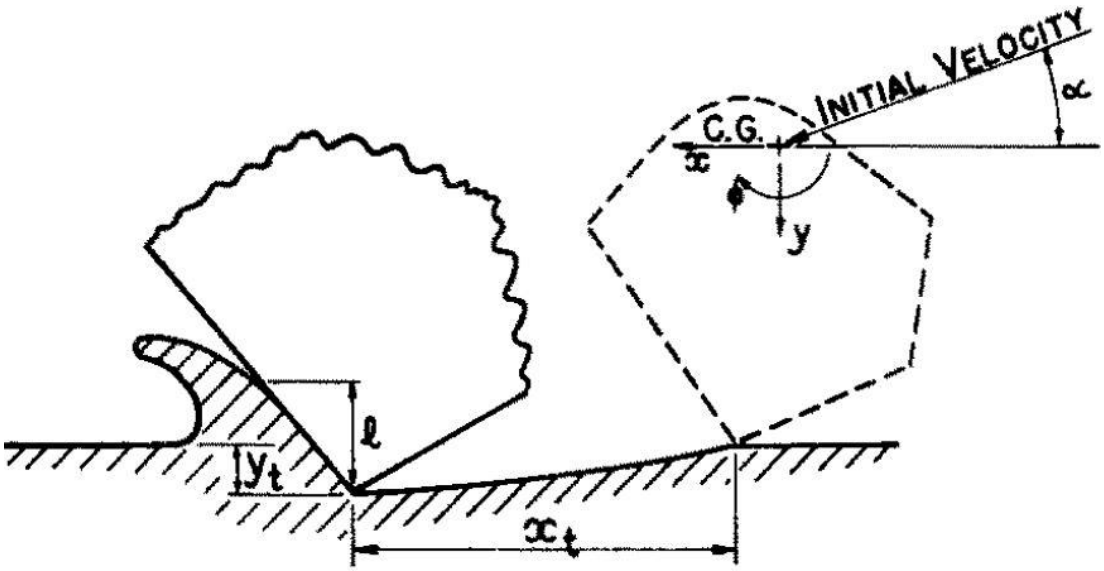

Figure 3.11: Idealised picture of abrasive grain striking a surface and removing material

$$\varepsilon_{VP} = \frac{mV^2}{p\psi K}\left(\sin 2a - \frac{6}{K}\sin^2 a\right) \quad for\ \tan a \leq \frac{K}{6} \tag{3.63}$$

$$\varepsilon_{VP} = \frac{mV^2}{p\psi K}\left(\frac{K\cos^2 a}{6}\right) \qquad for\ \tan a \geq \frac{K}{6} \tag{3.64}$$

where m and V are the mass and velocity of abrasive. The first expression applies to low impact angles a while the second one to higher angles. Both equations predict the same volume removal at tan2 a = K/6 and the maximum erosion occurs when tan2 a = K/3. The value $K \approx 2$ from Finnie is based on experimental measurement observations on scratch hardness testing [43] and grinding [112].

The erosion prediction of this model in correlation to experimental data is given in Fig. 3.12. There, the predicted material removal in relation to the impact angle from a single grain has the general form as experimental data erosion from multiple grains where there is a very good agreement, particularly at the low angle erosion.

The plastic flow stress p is the stress that exceeds the elastic limit and deforms the material at a constant strain rate. From solid mechanics theory the plastic flow stress is expressed:

$$P = K_p \varepsilon_T^{n_p} \tag{3.65}$$

where K_p is a constant [MPa], n_p is the dimensionless strain hardening exponent constant and the ε_T the true strain, expressed as a function of the elastic strain ε as:

$\varepsilon_T = \ln(1+\varepsilon)$. Strain ε in elastic limit can be also expressed as a function of the Young's modulus E as: $\varepsilon = \sigma_y / E$ where σ_y is the yield stress [113], [114].

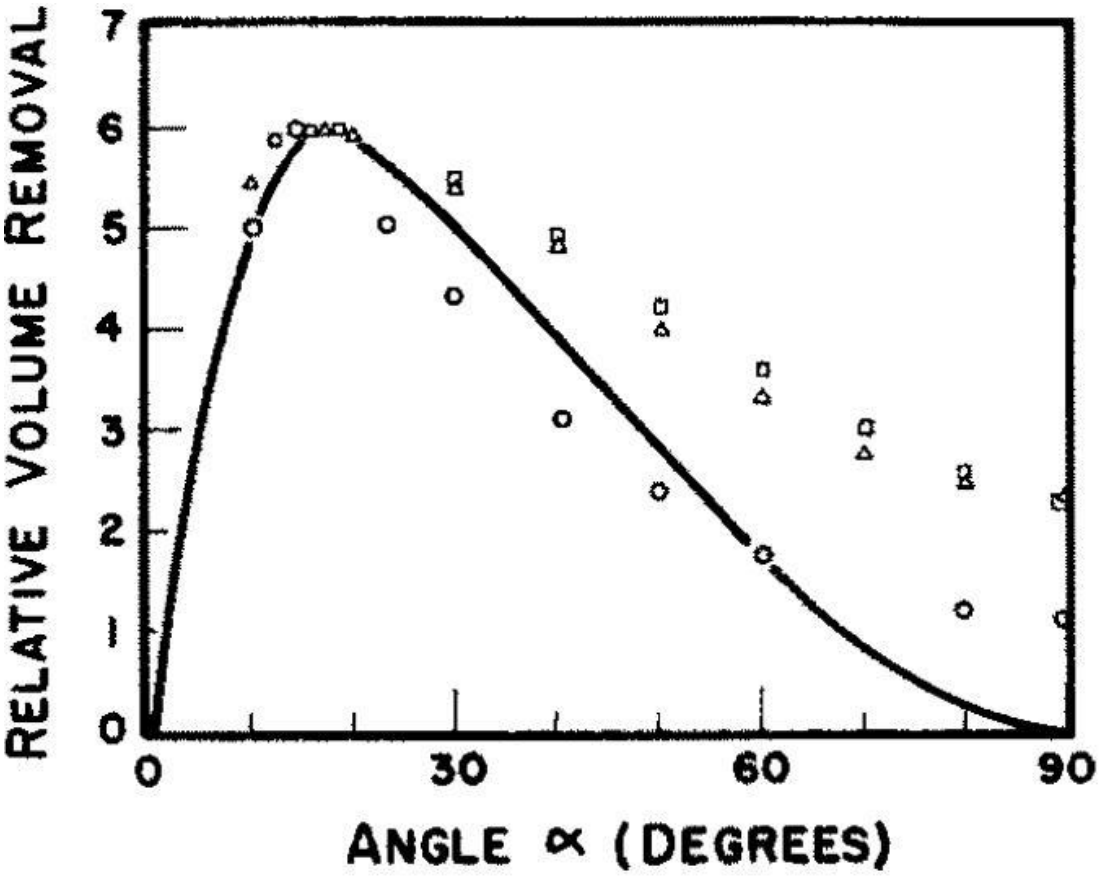

Figure 3.12: Predicted variation of volume removal with impact angle for a single grain in comparison with experimental data by many grains (Δ copper, □ SAE 1020 steel and ○ aluminium)

3.4.2 Advanced Finnie Model

The starting point of this model developed by Finnie is similar to the previous Finnie model [44] so that the volume removed from a surface by an idealised particle of arbitrary shape is approximately the integral of y_t and dx_t taken over the period in which the cutting occurs. Further assumptions can be made by stating that the area of particle contact to metal is about twice the given depth of cut. ($l = 2y_t$). Solving the motion equations, the volume removal is given as:

$$\varepsilon_V = \frac{cMV_P^2}{4p\left(1 + m_p r^2 / I\right)}\left(cos^2 a - \frac{\dot{x}_t'}{V_P}\right) \tag{3.66}$$

where: ε_V is the volume removed from the surface, M and m the mass of eroding particles and an individual particle respectively, I the particle moment of inertia, r and

U the particle radius and velocity respectively, a the impact angle, p the horizontal component of plastic flow stress, c the fraction of particles cutting in an idealised manner and $\dot{x}_t'$ the horizontal velocity of particle tip when cutting ceases. The effect of impingement angle α can be shown in for two possibilities: either the $\dot{x}_t'$ is zero, thus the cutting ceases when the particle tip horizontal velocity is zero or the particle leaves the surface while the tip moves horizontally and, in this case, $\dot{x}_t'$ should be determined for $y_t = 0$. This is given as:

$$\dot{x}_t' = V_p \cos a - \frac{2V_p}{P} \sin a \tag{3.67}$$

$$P = \frac{K}{1 + (mr^2/I)} \tag{3.68}$$

Therefore, the form of the two equations for each case ended up as:

$$\varepsilon_V = \frac{cMV_p^2}{4p(1 + mr^2/I)} \cos^2 a \qquad for\ \dot{x}_t' = 0 \tag{3.69}$$

$$\varepsilon_V = \frac{cMV_p^2}{4p(1 + mr^2/I)} \frac{2}{P} \left[\sin 2a - \frac{2 \sin^2 a}{P} \right] \quad for\ y_t = 0 \tag{3.70}$$

For the case of spherical particles, the moment of inertia is $I = (2/5)mr^2$, thus the Eq. 3.68 is recast as:

$$P = \frac{K}{1 + \frac{mr^2}{(2/5)mr^2}} \Rightarrow P = \frac{K}{3.5} \tag{3.71}$$

In the case where the $\dot{x}_t' = 0$, the impingement angle is calculated from Eq. 3.67 as:

$$\dot{x}_t' \Rightarrow 0 = V_p \cos a - \frac{2V_p}{P} \sin a \Rightarrow V_p \cos a = \frac{2V_p}{P} \sin a \Rightarrow \frac{\sin a}{\cos a} = \frac{P}{2} \Rightarrow \tan a = \frac{K/3.5}{2} \Rightarrow \tan a = \frac{K}{7} \tag{3.72}$$

Therefore, the material volume removal equations by spherical particles are modified as:

$$\varepsilon_V = \frac{cMV_p^2}{14P}\cos^2 a \qquad for\ \dot{x}_t' = 0 \tag{3.73}$$

$$\varepsilon_V = \frac{cMV_p^2}{2KP}\left[\sin 2a - \frac{7\sin^2 a}{K}\right] \quad for\ y_t = 0 \tag{3.74}$$

3.4.3 Benchmark Models

This study investigates the erosion from particle-laden flows on geometries that have been assessed in the literature. In this chapter, the erosion models of these works are provided. More specifically, for the backward-facing step and the annular cavity, the benchmark simulation case from [81] is based on a semi-empirical single-particle erosion model proposed by [77] and its expression is:

$$e = K_s V^n f(\alpha) \tag{3.75}$$

$$(\alpha) = \begin{cases} Aa^2 + Ba & a \le \varphi \\ X\cos^2 a \cdot \sin(Wa) + Y\sin^2 a + Z & a > \varphi \end{cases} \tag{3.76}$$

where e is the erosion rate on the point of impact, K_s is a scaling coefficient, V and a the local impact velocity and angle, respectively and *n* is the impact velocity power-law coefficient with typical values are in the range 1.8 and 2.3 for ductile materials. The dimensionless wear function f(α) describes the impact of angle effect on the surface wear. A, B, X, W, Y, and Z are empirical coefficients and φ is an empirical value for the impact angle. The values for the coefficients for carbon steel and aluminium are given in the following Table 1 [77], [78], [115], [82]:

Constants	Materials	
	Carbon Steel	Aluminium
A	38.4	-34.79
B	22.7	12.3
ϕ	15º	10º
X	0.3147	0.147
Y	0.03609	-0.745
W	0.2532	1
n	1.73	1.73

***Table 1: Empirical coefficients for erosion model* [77]**

4 Single Particle-Wall Interactions Study

4.1 INTRODUCTION

In this chapter, the analysis of single particle sedimentation is carried out. The particle is released from a certain distance above a wall and the downward motion of the spherical particle is examined in a static flow field. The dry coefficient of restitution is assumed applicable and the particle rebounds after the collision. The study considers different forces applied to the particle and the influence of these in particle motion is investigated. The results of particle-wall interaction are compared to the literature [13] and the importance of each force using the E-L solver is examined.

The important parameter for collision in a fluid is not the Reynolds number but the Stokes number given by $St = 1/9(\rho_p/\rho_f)Re$, where ρ_p, ρ_f are the particle and fluid density respectively and Re is the particle Reynolds number. Therefore, a rebound general description can be obtained by a correlation between the global coefficient of restitution ε and the Stokes number St that incorporates the particle inertia (added mass included) and the viscous force exerted on the particle during the drainage of the liquid film between the particle and the wall. The coefficient of restitution ε is defined by the equation $\varepsilon = v_r/v_{imp}$, where v_r is the rebound velocity and v_{imp} is the impact velocity as discussed. For comparison of the effective coefficient of restitution with experimental data, the rebound velocity of the sphere is captured at $t_r = t_{imp} + 0.001s$, where t_r and t_{imp} are the rebound and impact times, respectively [13]. The glass friction coefficient μ is equal to 0.1. In addition, there is no heat transfer between the two phases, therefore the energy equation is not required.

4.2 SIMULATION MODELLING

4.2.1 Geometry and meshing

The geometry is a 2D domain where the z-direction (required in OpenFOAM) is set as one cell (Fig. 4.1). The computational domain size is 30x30 mm (x = 10d, y = 10d). The bottom patch represents the glass wall in the simulation. The wall material density is 2.5 g/cm^3, the Young's modulus $5.5x10^{10}$ Pa and the Poisson's ratio 0.333. The fluid domain is placed inside the cavity. The top patch is open, and the zero-

gradient boundary condition is applied. The particle centre is placed at x = 15 mm (5d) and y = 6 mm (2d). The material and fluid properties are given in Table 2.

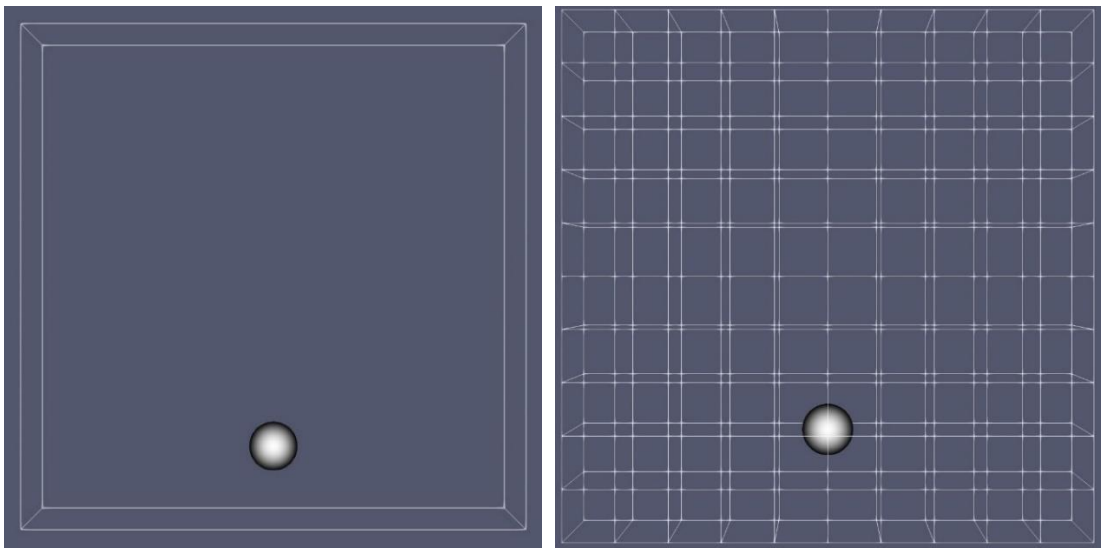

Figure 4.1: Particle-wall geometry and mesh domain in viscous flow

Fluid properties			
Density	ρ_f	0.935	g/cm^3
Kinematic viscosity	v_f	0.1	cm^2/s
Particle properties			
Diameter	d	0.3	cm
Density	ρ_p	7.8	g/cm^3
Young's modulus	E_p	$2.0x10^{11}$	Pa
Poisson's ratio	υ_p	0.333	-
Gravity	g	981	cm/s^2

Table 2: Physical properties of fluid and particle

The maximum domain mesh size is selected (cell size equal to particle diameter), therefore the cell size is 3x3 mm. An investigation of the mesh size correlation to the results is discussed in the next section.

4.3 RESULTS AND DISCUSSION

4.3.1 Sedimentation of a sphere particle towards a wall

At first, the movement of a spherical particle towards a wall with different forces applied is investigated. The results of each simulation are compared to the results from the Ardekani & Rangel study [13]. In their study, the dynamics of a particle-particle collision colliding with a wall in a viscous fluid are investigated. Also, the effective

coefficient of restitution dependency on the Stokes number is analysed. They utilised a Lagrange multiplier based computational method and the Finite-Volume Method is incorporated using a staggered grid for incompressible flow. The SIMPLE algorithm is utilised to solve the fluid equations accounting for the fluid presence.

In this study, the particle forces applied are drag and gravity, lift and virtual force. The time step for each case is $\delta t = 10^{-3}$ sec. The particle velocity and distance h from the bottom of the sphere to the wall are shown in Fig. 4.2 and Fig. 4.3 under the effect of each force. The domain mesh cell size of 3x3mm is equal to the particle diameter. The Reynolds number when the sphere approaches the wall is 55.3 and the impact Stokes number is 52. These values are consistent with the Ardekani & Rangel [13] values with a variation of about 10%. In Fig. 4.4, the fluid and particle velocity distribution are shown for pre-collision, collision and post-collision times as the particle approaches the wall after it is released from rest. The forces applied to the particle for this case is gravity, drag and virtual mass. In the first case, only the drag force is applied to the particle. Then, the drag with the lift force and the drag with the virtual mass is applied. Finally, all the above forces are applied to the particle altogether.

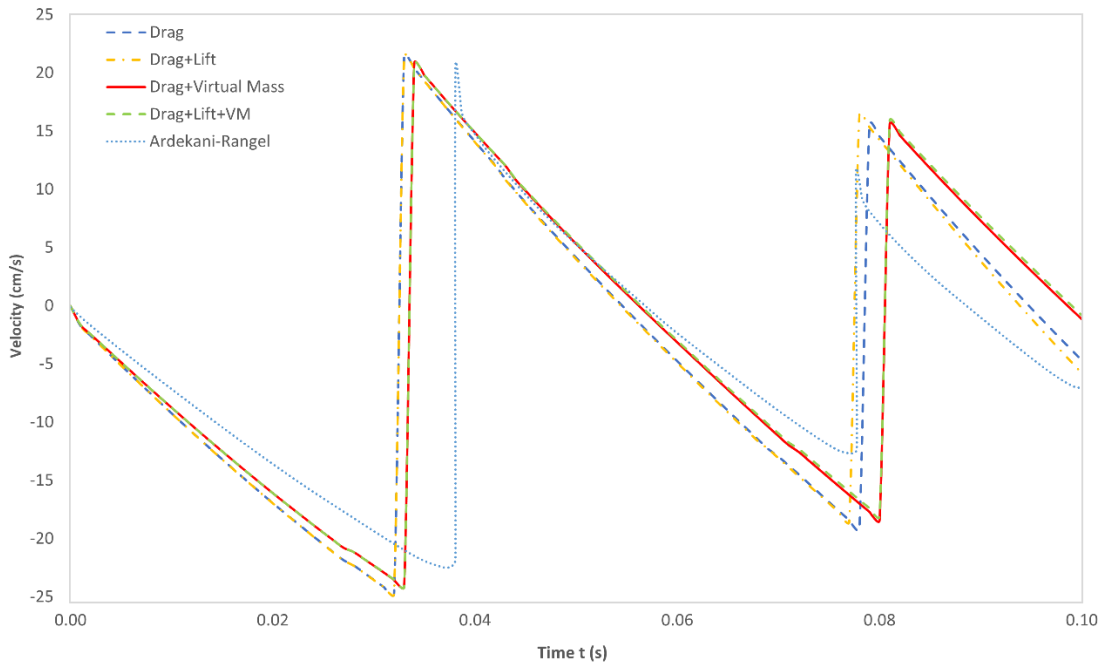

Figure 4.2: Particle vertical velocity Uy in fluid over time

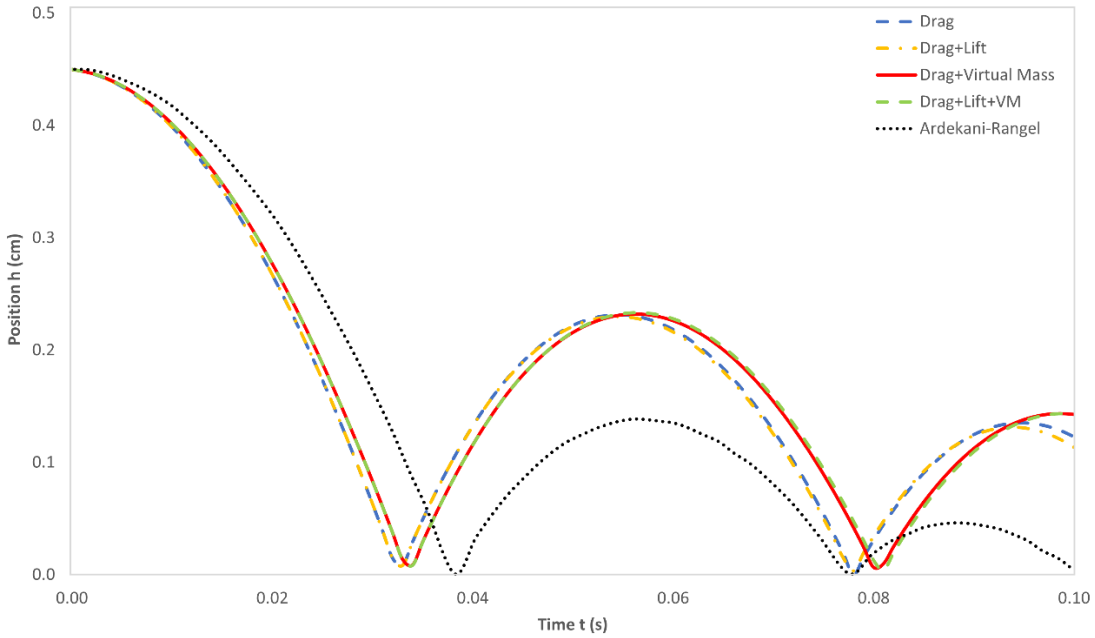

Figure 4.3: Distance of particle surface to wall

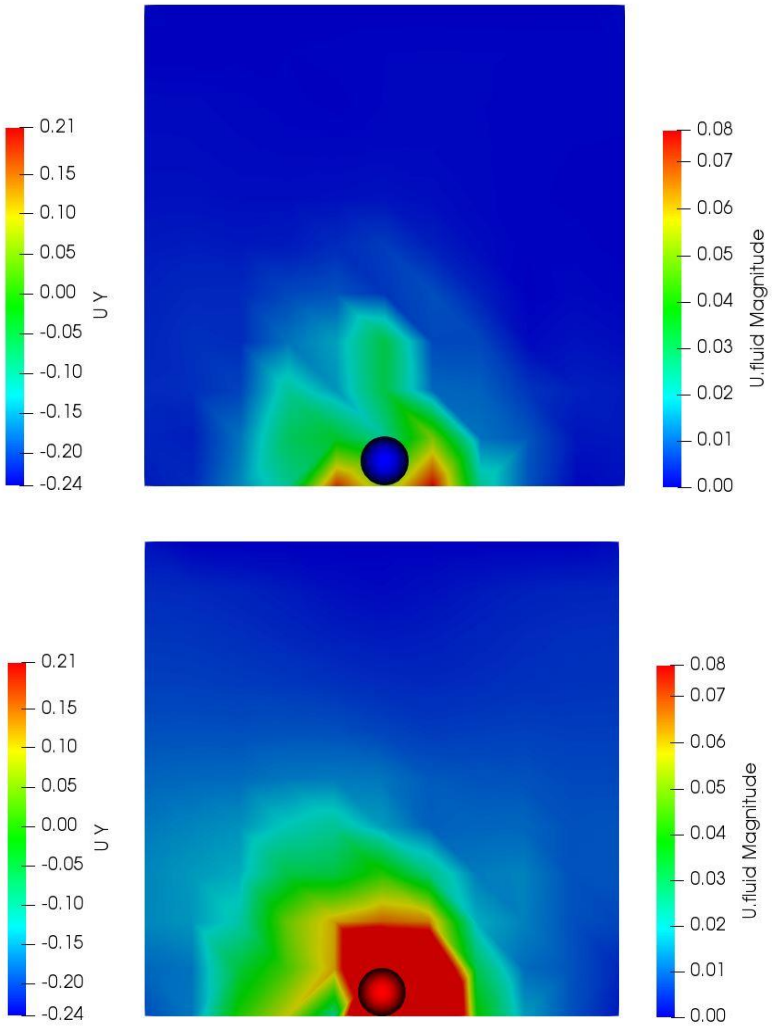

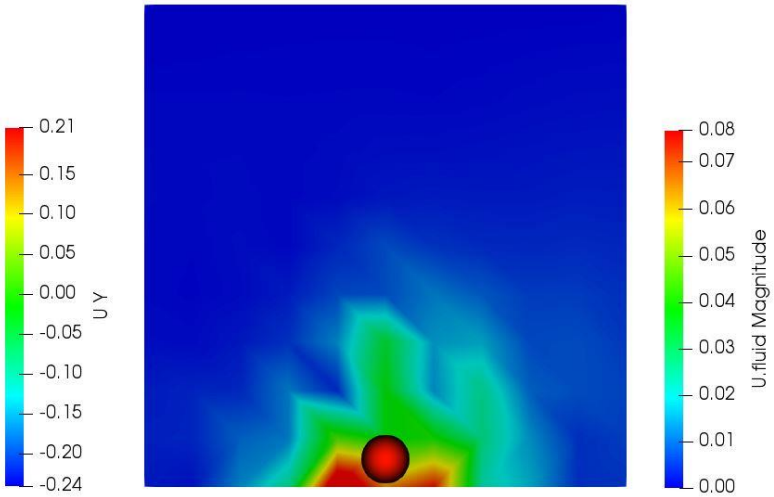

Figure 4.4: Fluid velocity contours of pre- and post-collision at t=0.033, t=0.034 and t=0.035 sec – velocity in m/s (drag and virtual mass forces applied)

Appling each force individually, the effect of each one is noticeable on the particle velocity and height profiles at each time step. When only drag force is acting, the particle is moving faster towards the wall and reaching a higher velocity (about 9.2%) compared to benchmark data. At the contact time, there is no liquid between the particle and the wall resulting in the particle velocity jumping to the post-collision velocity $V^{t_c^+} = -\varepsilon_{dc} V^{t_c^-}$. The particle velocity when the particle reaches the maximum rebound height is similar between the simulation and the benchmark with less than 3% discrepancy. As the sphere is receding from the wall, the liquid fills the gap and a significant decrease in the particle velocity occurs due to large viscous dissipation. As the gap widens this viscous dissipation reduces and particle velocity changes are much slower. The sphere approaches the wall again at a similar time compared with the experimental data but the difference in the terminal velocity is significant (about 24% variation). When the lift is added the profile is improved after the second bounce when some amount of lift force is generated. Applying only drag and added mass, the collision velocity variation is about 7% and post-collision velocity is identical. However, the sphere bounces about 3ms slower at the second collision. With a combination of all forces applied on the particle, drag and added mass are the dominant forces as the lift and pressure gradient contribution is insignificant.

4.3.2 Mesh dependant results

In this section, the simulation results are compared against the different mesh sizes. The minimum mesh size where the cell size is equal to the particle diameter was examined above. Therefore, the option of a coarser mesh is only available. The two structured mesh domains are chosen with a 5x5 and 3x3 cavity size which provides a cell size of 6x6 mm and 10x10 mm, respectively (Fig. 4.5). The time step remains the same at $\delta t = 10^{-3}$ sec. To reduce the number of simulation options, only two cases with the gravity/drag/lift and gravity/drag/virtual mass forces applied to the particle are examined. The simulation results against the different meshing are given in Fig. 4.6 and 4.7.

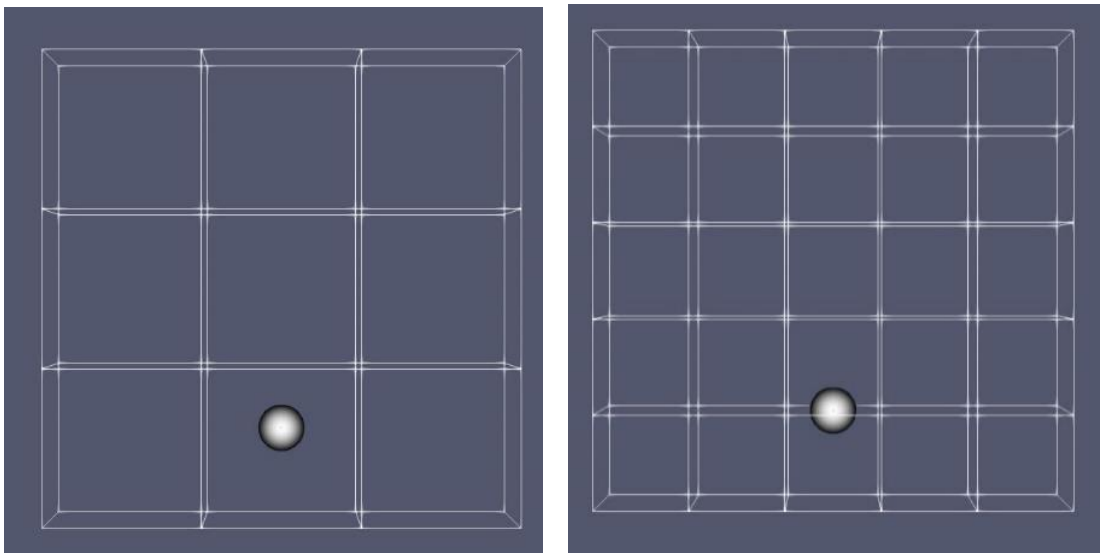

Figure 4.5: Geometry mesh of cases run

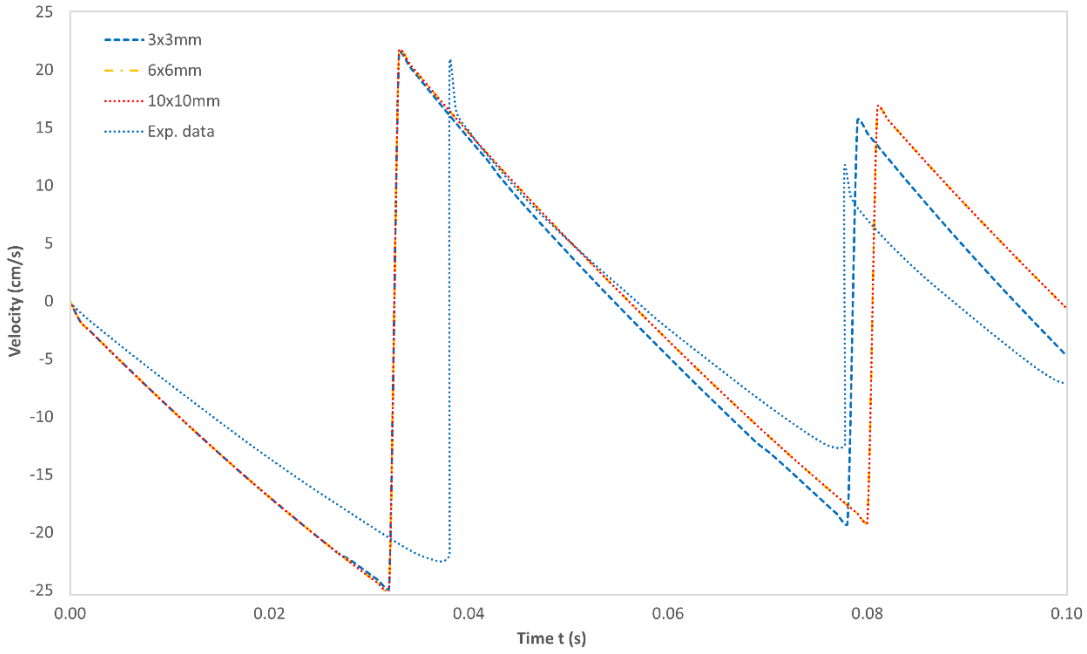

Figure 4.6: Vertical velocity of sedimented spherical particle for each mesh size with gravity, drag and lift forces

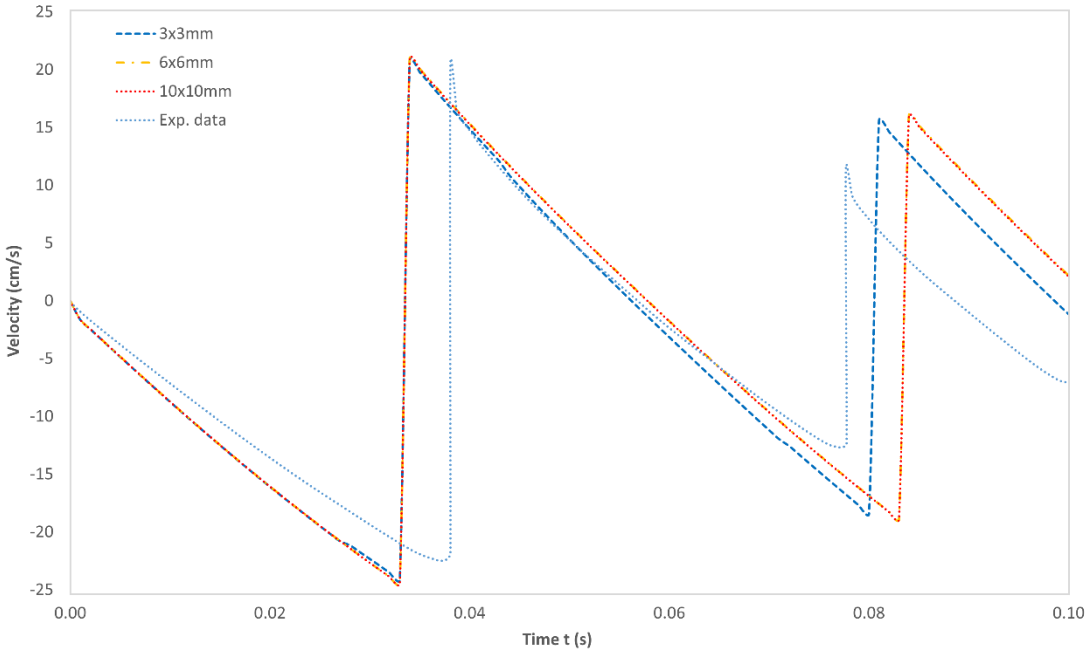

Figure 4.7: Vertical velocity of sedimented spherical particle for each mesh size with gravity, drag and virtual mass forces.

The above results show that mesh size does not affect the particle motion significantly, predominantly until the first rebound. There is some improvement for the finer mesh as the sphere approaches the wall again and it closes the gap between the simulation results and the experimental data. Therefore, the simulations are not heavily dependent on the mesh size. From an erosion perspective, since only the first

and second impacts contribute to the erosion these need to be as accurate as possible in this sense.

4.3.3 Time-dependent results

In this section, the simulation results are compared against the different time steps. The time step is set as $7.5x10^{-4}$ and $5.0x10^{-4}$ sec, respectively. The grid mesh used is 3x3 mm. There are two studies to investigate the time step influence using different force combinations. The combination of the gravity, the drag and the lift forces are applied in one study and the combination of the gravity, the drag and the added mass forces are applied in the second study. In Fig. 4.8 and 4.9 the particle velocity with time is shown.

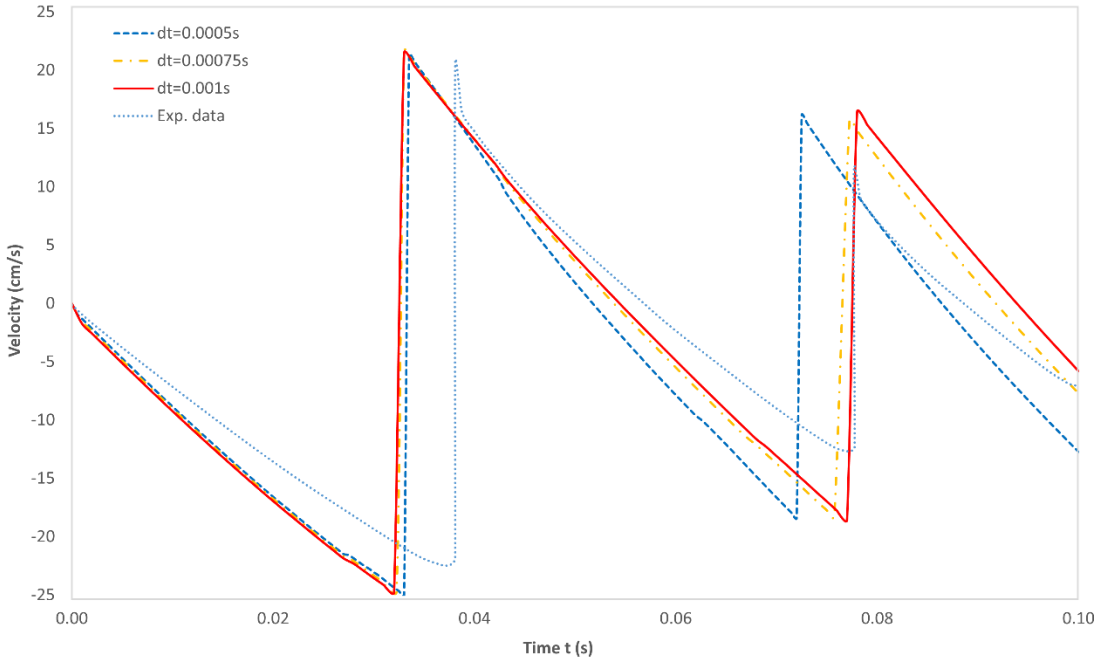

Figure 4.8: Particle vertical velocity for different time steps with gravity, drag and lift forces.

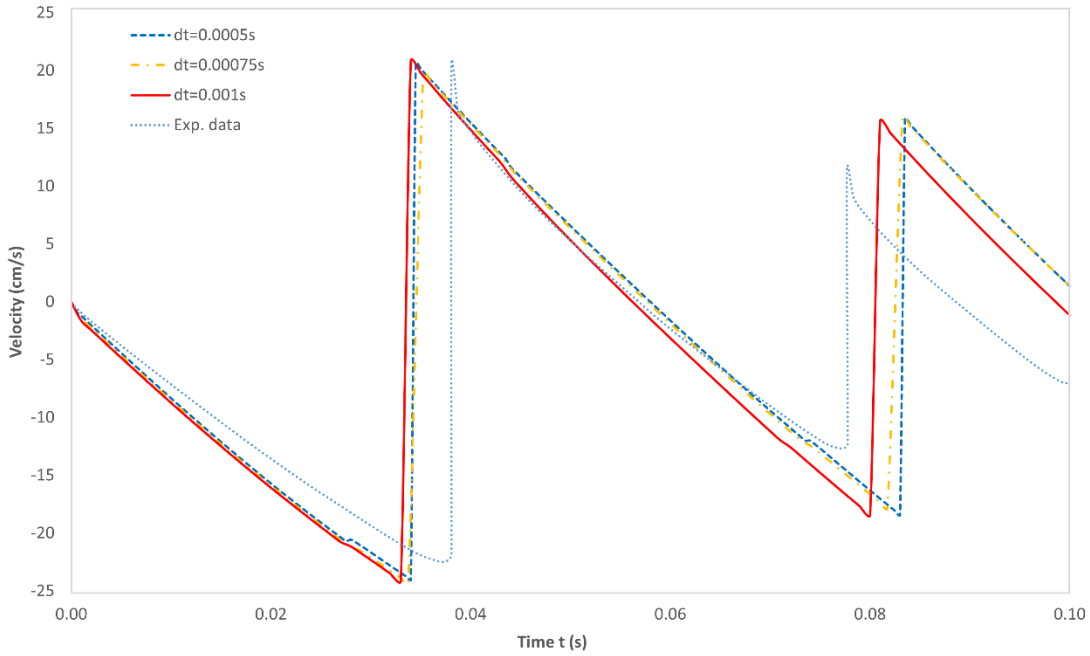

Figure 4.9: Particle vertical velocity for different time steps with gravity, drag and virtual mass forces.

The time-step affects more the simulation results compared with the mesh size but still not significantly. On the gravity, drag and lift case (Fig. 4.8), the particle moves slightly faster towards the wall while pre- and post-velocities are identical. For 0.001s and 0.00075s cases the velocity profile is quite similar and agree well with the data. For the smaller time step, the particle is moving faster towards the wall after the first collision, whereas this is not happening when added mass is considered. For the drag and added mass case (Fig. 4.9), again the velocity profile slightly improves as the sphere firstly bounces on the wall. As it moves towards the wall after the rebound, the 0.00075s and 0.0005s cases are reaching the wall about 5.7ms slower compared to experimental data.

4.3.4 Coefficient of restitution

A general description of the particle rebound is proposed by Legendre et al. [116]. The correlation of the global coefficient of restitution ε and Stokes number that contains the particle inertia (including the virtual mass) and the viscous force exerted on the particle as a liquid film between the particle and wall is drained. In Fig. 4.10, the normalised coefficient of restitution for the dry collision ($\varepsilon/\varepsilon_{dc}$) as a function of the Stokes number is shown for the simulation results, the experimental data [12] and the lubrication theory [117]. The fluid streamlines of general fluid flow around the particle are also shown before and after the collision (Fig. 4.11).

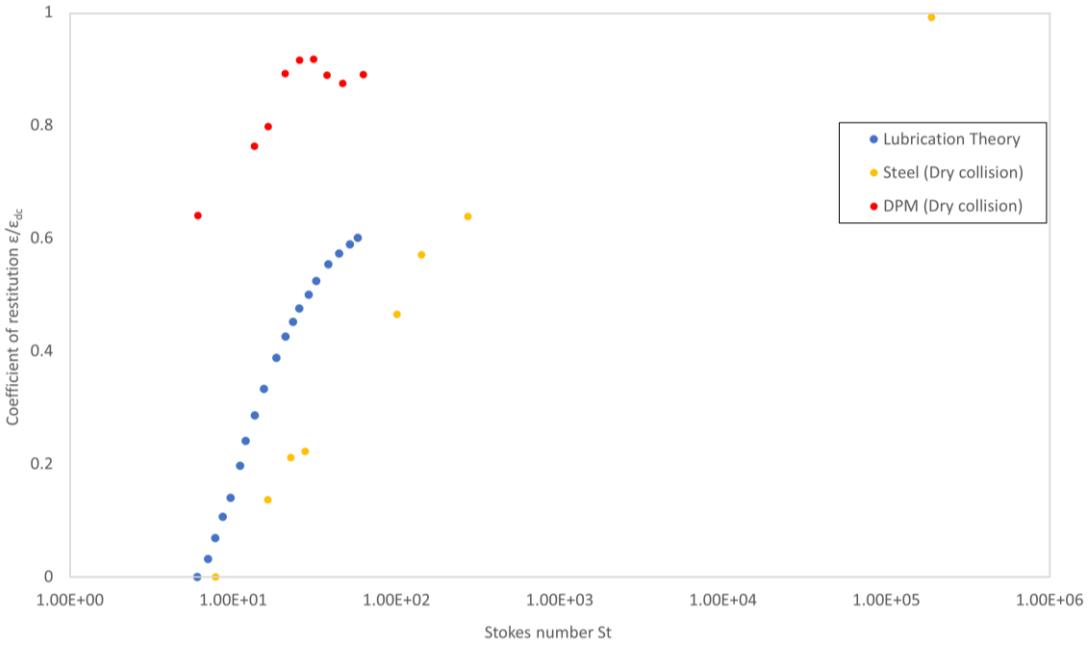

***Figure 4.10: Coefficient of restitution normalised for dry collision as a function of Stokes (St) number. Present results for DPM simulation (red), lubrication theory (blue) as per* [117] *and experimental data (yellow) for steel as per* [12].**

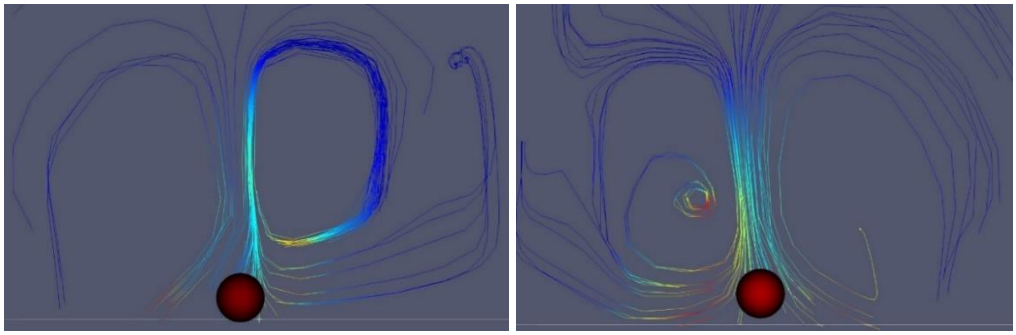

Figure 4.11: Streamlines pre- and post-collision of steel sphere on the glass wall (present results from DPM simulation).

As shown in Fig. 4.10, the coefficient of restitution deviates from the lubrication theory curve by as much as 40%. This shows the importance of the lubrication force for the estimation of the coefficient of restitution. However, the force is significant when the particle size is relatively large compared to the geometry cavity This is out of scope for this study as a large number of relatively small diameter particles are the focus of this study.

4.3.5 Virtual mass coefficient quantification

As shown previously, the virtual mass contributes a lot to particle dynamics, therefore a further investigation on this force is carried out in this section. The virtual mass coefficient is investigated by trying to assess the correlation of the value used in this study with the literature results.

Here, the assumption of incompressible flow and a rigid particle is maintained. Therefore, any instantaneous particle velocity change leads to an associated change to the fluid field velocity due to the ellipticity of the governing equations. The integration of the N-S equation during the collision turns to [13]:

$$\rho_f\left\{V^{t_c^+} - V^{t_c^-}\right\} = -\nabla\tilde{I} \tag{4.1}$$

where $\tilde{I}$ is the pressure impulse (the pressure gradient is unbounded and numerically the finite pressure impulse obtained), t_c is the time at which collision occurs and +/- the infinitesimal times before and after the collision, respectively [13].

The integration of the vorticity equation from t_c^+ to t_c^- results in a vorticity jump equal to zero, the velocity jump (the term $V^{t_c^+} - V^{t_c^-}$ to Eq. 4.1) is irrotational. Despite the wall, where additional vorticity is irrotational since it takes time for the diffusion of this vorticity. This irrotational flow is used for the calculation of the virtual mass [13].

For a particle p, the virtual mass is unaltered by finite-Reynolds-number effects and the contribution to the particle total force that depends on the instantaneous value of the acceleration is identical to that predicted by irrotational theory. The virtual mass coefficient of a solid particle towards a wall is equal to [15]:

$$C_{vm} = \frac{1}{2}\left\{1 + \frac{3}{8}\left(\frac{r}{r+y}\right)^3\right\} \tag{4.2}$$

where r is the sphere radius and y is the particle distance from the wall

The virtual mass coefficient described by Ardekani and Rangel [13] is given by:

$$C_{vm} = \frac{1}{2}\left\{1 + \frac{1.591}{(1.917 + y/r)^{3.887}}\right\} \tag{4.3}$$

The added mass coefficient plot of the simulation against the Ardekani & Rangel [13] results are given in Fig. 4.12.

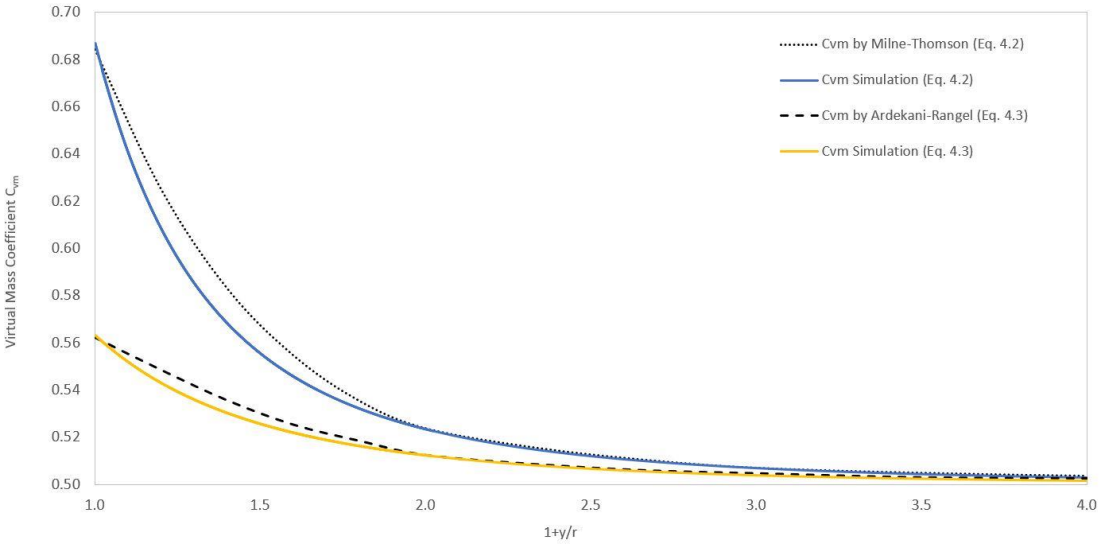

Figure 4.12: Virtual mass coefficient for a solid sphere moving towards a wall.

Milne-Thomson [15] suggested an expression of the sphere that its kinetic energy in an unbounded flow is increased by a wall correction function in the form of an infinite series that depends on the scaled centre-to-wall distance (y/r). By curtailing the series at the order of $(y/r)^{-3}$, the approximated wall-amplified virtual mass coefficient is retained (Eq. 4.2). Eq. 4.3 is derived from the viscous potential flow theory for a sphere moving towards a wall in the normal direction [13], [16]. This is used to calculate the force contribution that is applied to the sphere which is proportional to the particle acceleration. The potential flow solution can be acquired by a coupled-source image in the sphere and is provided as a series. The two solutions are very close for the 1+y/r values above 3 while for the 1+y/r = 1, they give C_{vm} values of 0.69 and 0.56, respectively. By applying the above equations to the simulation results, it is given that there is a good agreement of the results for the 1+y/r values above 2 whereas the results from the simulation are given slightly more concave curves for lower 1+y/r values.

4.3.6 Conclusions

In this study, the effect of different forces acting on a spherical particle is examined. The simulation results are compared with a benchmark case and mesh size and simulation time step is investigated. Generally, the simulation results follow quite well the benchmark profiles qualitatively. There is some good agreement of the results with a minimum variation when drag and added mass are applied, particularly when

the sphere moves towards and bounces at the wall from rest. A degree of the lift force is generated when the sphere rebounds again from the wall, however, the predominant forces are drag and added mass. The lubrication force due to the fluid effects close to the wall and the history (Basset) force was assumed small in this study but could also contribute.

Moreover, the virtual (added) mass coefficient agrees quite well with the benchmark data based on the equations given in Section 4.2.4. This is quite important as the solver captures well a dominant particle force, and this can be used on particle-laden flow cases that are used to estimate the erosion on the cavities.

5 Turbulence flow in backward-facing step

5.1 INTRODUCTION

The Backward-Facing Step (BFS) captures the key features found in general for separated flows. Its nature is three dimensional, however, it is ideal for a two-dimensional (2D) analysis under certain conditions with a simple step geometry.

The analysis of turbulence modifications by the particles with a fully developed flow in the channel is carried out. First, the analysis of turbulence in the channel without the presence of particles (unladen) is assessed. After that, the particle-laden flow is analysed to examine the influence of the particles on the flow. This is the first step to understanding the impact of the particles on the turbulence flow regime. The next step is to utilise the results from this study to assess the erosion on similar pipeline channels which is carried out in the next chapter.

5.2 BACKWARD–FACING STEP SIMULATION MODELLING

5.2.1 Problem description

The BFS involves the basic features of general separation flows. The schematic representation and flow development can be shown in Fig. 5.1 [118].

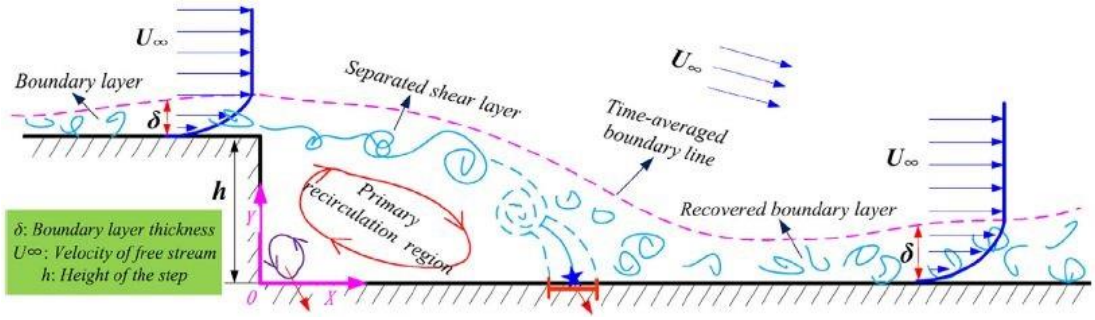

***Figure 5.1: Schematic geometry of BFS and flow evolution* [118]**

The BFS consists of a channel with height H and a step of height h. An inflow with uniform velocity (turbulent in this study) is considered into the channel. The flow field is generally divided into four regions: the separated shear layer, the primary recirculation region below the shear layer, the re-attachment region, and the recovery

region. The BFS flow occurs with large separations vortices in the backward step region and a smaller vortex in the corner.

5.2.2 Geometry

For this study, the BFS geometry was selected as per Fessler-Eaton experimental set-up (Fig. 5.2) [38]. The step and entrance channel height are H = 0.0267m and h = 0.04m, which results in an expansion ratio of about h/H = 5/3 [38]. The upstream and downstream channel length is set to L_U = 10h and L_D = 35h, respectively while the channel span is B = 4.28h. The upstream channel is relatively long and required to establish fully turbulent inlet conditions using a recycling method, which copies the turbulent velocity from a plane downstream of the channel entrance back onto the inlet. The periodic boundary conditions (BC) are applied in a spanwise direction, whereas no-slip boundary conditions were set at the lower and upper channel walls [39].

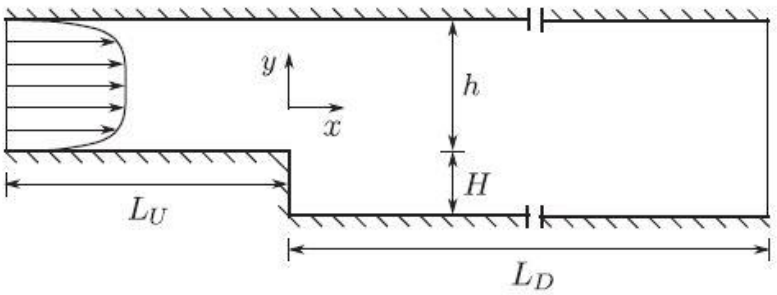

Figure 5.2: BFS geometry

5.2.3 Mesh

The HRN method is used initially to run the case and compare the simulation results with the experimental data for the unladen flow. To ensure mesh independence, three structured mesh grids with $1.5x10^4$, $2.5x10^4$ and $5.0x10^4$ cells were used. To resolve the boundary layer, the first grid point of the bottom wall was placed into the viscous sublayer area ($y^+ < 5$) using gentle grid stretching only in the bottom wall-normal direction. However, to keep the mesh and computational requirements at achievable levels, the first cell centroid of the leading (vertical) wall was placed in the log-law sublayer and get solved using wall functions. This was achieved using the multi-grading feature, therefore the mesh stretched to the walls. More specifically, the y^+ values for each mesh case are given below (Table 3):

	Corse Mesh	Medium Mesh	Fine Mesh
Resolution (cells no.)	$1.5x10^4$	$2.5x10^4$	$5.0x10^4$
Bottom wall y^+	1.31	1.09	1.09
Leading wall y^+	87.01	43.68	21.89

Table 3: Mesh resolution and y^+ values for the cases (HRN method)

For reference, the grid for the fine mesh case is given below (Fig. 5.3).

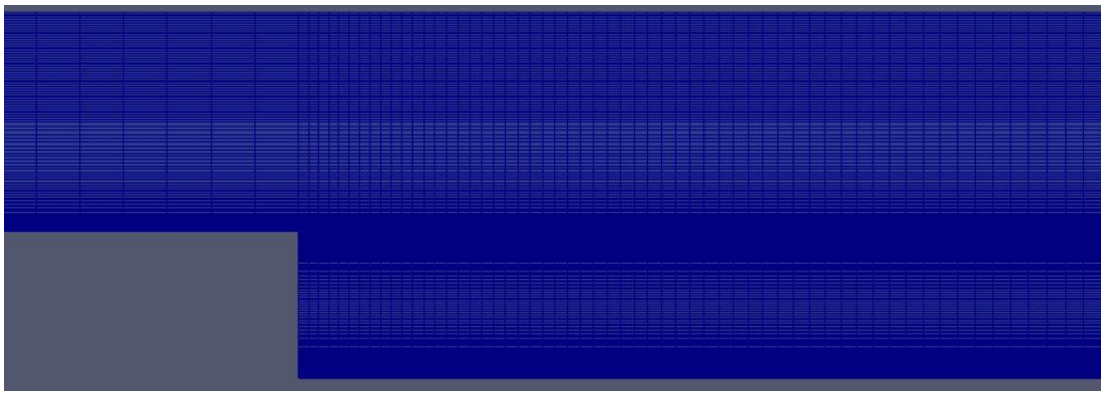

Figure 5.3: Mesh of $5.0x10^4$ cells close to the step (HRN approach)

5.2.4 Boundary Conditions

The boundary conditions for the far-field are calculated from Eq. (3.58) and (3.59) as:

$$k = \frac{3}{2}(0.06 \cdot 9.39)^2 \Rightarrow k = 0.45\ m^2/s^2$$

$$\omega = \frac{0.45^{0.5}}{0.09 \cdot 0.0028} \Rightarrow \omega = 2{,}662\ s^{-1}$$

The values of the k and ω parameters calculated above comply with the literature of the BFS simulation [40]. The turbulent quantities at the no-slip wall should be set as zero apart from the ω value [110], [119]. The mesh resolution in the leading (vertical) wall falls into the logarithmic layer while the bottom wall resolution into the viscous sublayer. Therefore, the boundary conditions are given by Eq. 3.56 for the leading wall and Eq. 3.57 for the bottom wall depending on the distance y of the first cell centroid to the adjacent wall.

5.3 RESULTS AND DISCUSSION

5.3.1 Unladen Flow

The first simulation case includes the unladen flow in the BFS in a 2D domain. The normalised mean ($U_{x,mean}/U_0$) and fluid fluctuating velocity ($U_{x,rms}/U_0$) are derived along the normalised height y/H. The air viscosity is given as $\nu = 1.5x10^{-5}$ m^2/s. The averaged mean velocity in the inlet is given as $U_{x,avg}$ = (9.39, 0, 0) m/s with a maximum velocity of $U_{x,0}$ = 10.5 m/s at the centreline (y/H = 0.5). The Reynolds number based on the centreline velocity of the upstream channel and the step height is $Re = U_0H/\nu$ = 18,700. The mean and fluctuating velocity graphs are given below against the experimental data from Fessler-Eaton (Fig. 5.4 and Fig. 5.5, respectively). On these plots, the y-axis is the normalised height of the channel (y/H) and the x-axis is the normalised profiles of time-averaged streamwise mean and fluctuating velocity, respectively. These velocities are amplified slightly (by 2 for the mean velocity and by 10 for fluctuating velocity) for clarity and comprehensibility [39]. Then the term x/H is added to show associated velocity profile over the length of the channel.

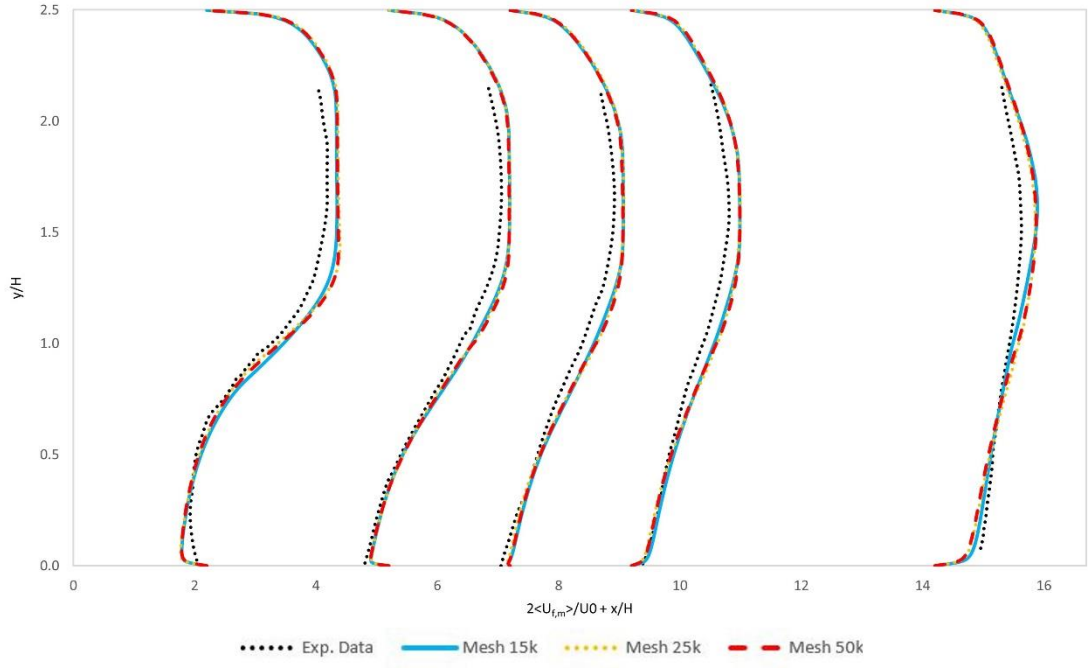

Figure 5.4: Comparison of the time-averaged flow profiles (continuous phase) for the streamwise mean velocity ($U_{f,m}$) in the backward-facing step flow with the experimental data* [38] *at x/H = 2, 5, 7, 9, 14 (HRN approach).

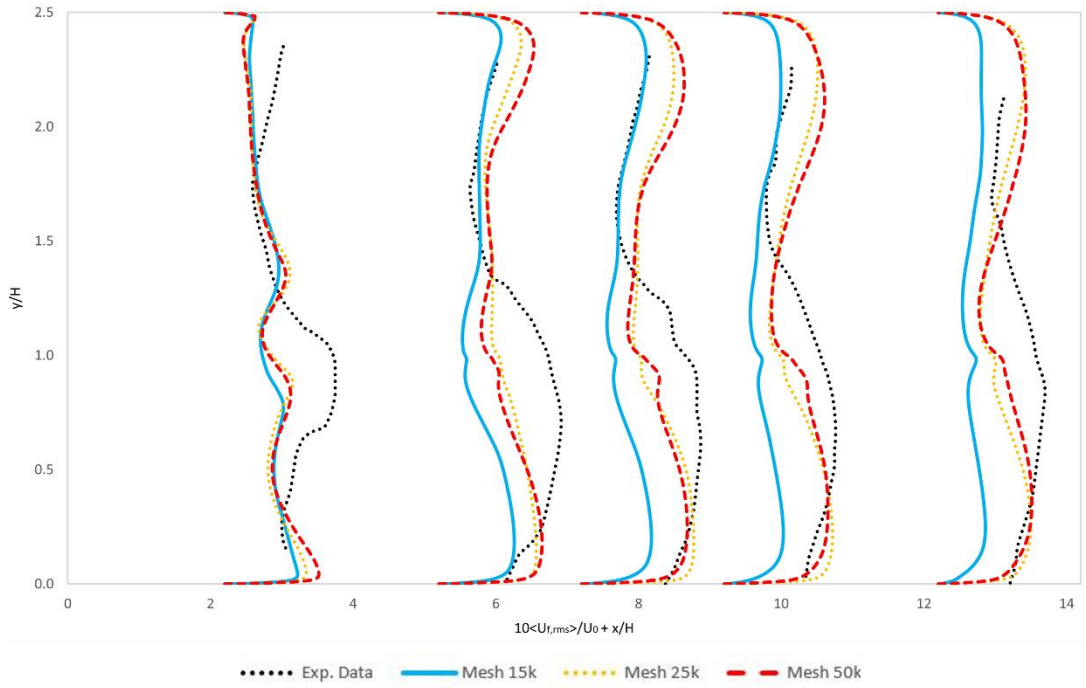

Figure 5.5: Comparison of the time-averaged flow profiles (continuous phase) for the streamwise velocity fluctuations ($U_{f,x,rms}$) in the backward-facing step flow against the experimental data* [38] *at x/H = 2, 5, 7, 9, 14 (HRN approach).

The fluid mean velocity graph (Fig. 5.4) shows an insignificant difference between the coarse, medium and fine mesh simulation and are in very good agreement with the experimental data for unladen flow [38]. The fluctuation velocity (Fig. 5.5) tends to correspond to the experimental curve, particularly in the bottom wall region. There is some divergence at the free stream region, particularly in the vertical distance above the y/H = 1.8. Moreover, behind the aft wall strong fluctuations are developed in the recirculation region and the upper flow channel which expands further away from where the flow becomes more uniform. Overall, there is a satisfactory qualitative agreement with the experimental data, however, a quantitative difference is visible.

The streamlines of the fluid mean velocity over the x-direction are given below for each mesh case (Fig. 5.6-5.8). For comparison, the streamlines of the BFS are given from the literature [82] for validation (Fig. 5.9).

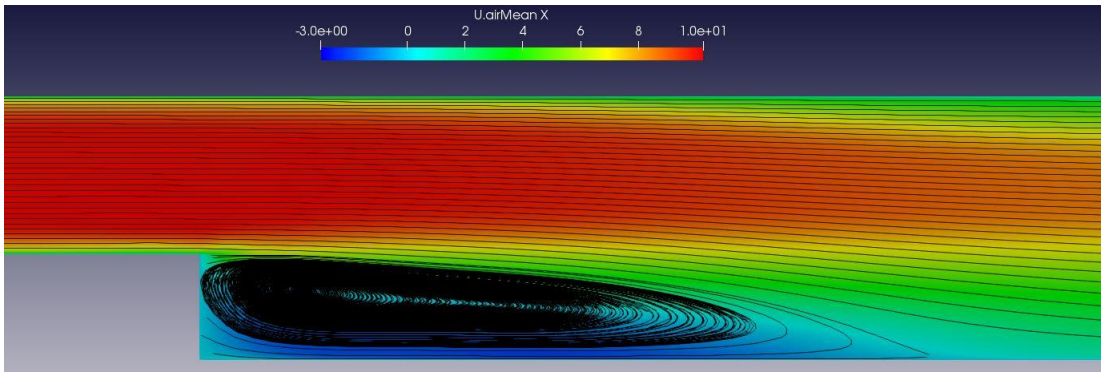

Figure 5.6: Streamlines of the fluid U_x, mean velocity for the 1.5x10^4 cells mesh (HRN method)

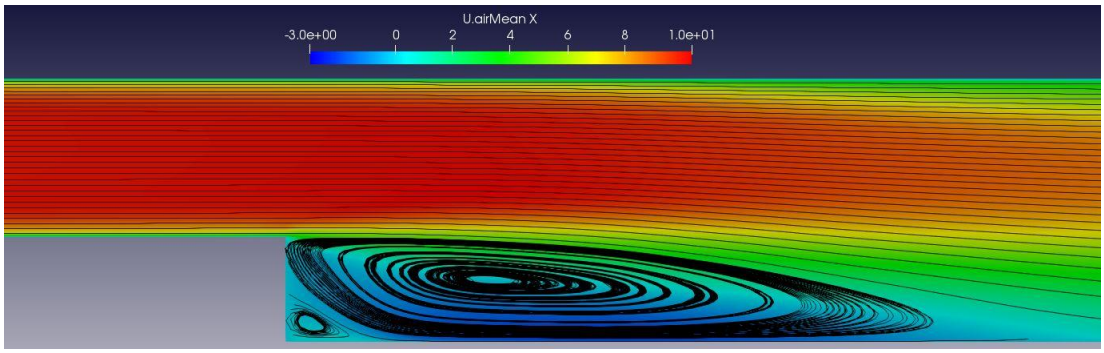

Figure 5.7: Streamlines of the fluid U_x, mean velocity for the 2.5x10^4 cells mesh (HRN method)

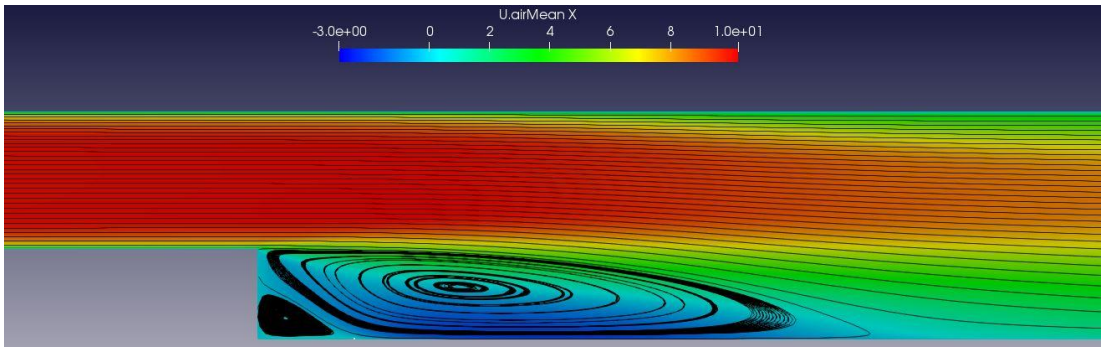

Figure 5.8: Streamlines of the fluid U_x,mean velocity for the 5.0x10^4 cells mesh (HRN method)

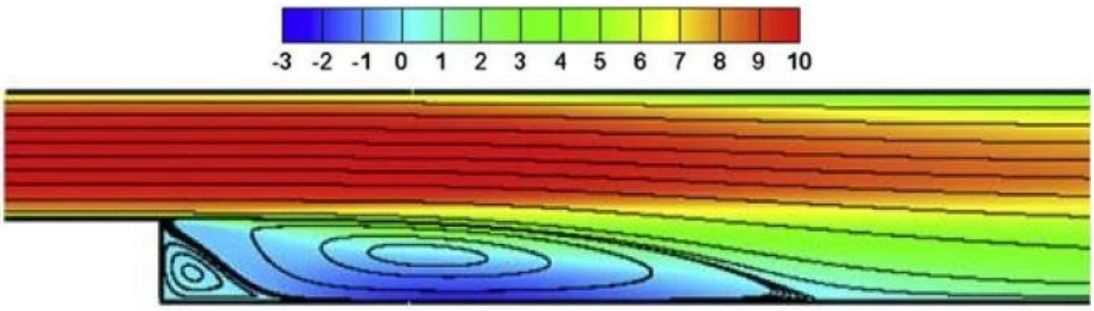

Figure 5.9 Streamlines of the fluid U_x, mean velocity **[82]**

In Fig. 5.6 to 5.8, the streamlines on the re-circulation area for all the cases are displayed. It is shown that a shear layer of the fluid flow separates from the leading wall and re-attaches on the bottom wall. The shear layer creates two vortices: the main vortex which is the large vortex adjacent to it and the secondary vortex which rises from the main and rotates opposite to the leading wall corner. It is shown that on the coarse mesh (Fig. 5.6) only the main vortex developed in an oblong shape. The main vortex improved on the medium mesh (Fig. 5.7) and the secondary vortex appears, while the finer mesh simulation (Fig. 5.8) shows very clearly the vortices development and is in very good agreement with the results against the literature (Fig. 5.9) [82]. The reattachment point (y/H = 7.49) for the fine mesh simulation agrees very well with Fessler's point (y/H = 7.4) [38].

The next case is the unladen flow in the BFS with the LRN approach. The number of grid cells remains similar, however, the integration on the leading (vertical) wall gives a $y^+ \approx 1$, therefore the first cell centroid falls into the viscous sublayer. To achieve this, the downstream domain length L_D is reduced to a value of $L_D = 10h$. As before, the mesh sensitivity will be checked with three mesh structures of the same cell numbers. Obviously, the wall functions are not used here with fixed values set as boundary conditions similar as before. The integration on the bottom and top walls remains as the HRN simulation (Table 4). For reference, the fine mesh structure near the wall and the fluid mean and fluctuating velocity is given below (Fig. 5.10).

	Coarse Mesh	Medium Mesh	Fine Mesh
Resolution (cells no.)	$1.6x10^4$	$2.5x10^4$	$5.0x10^4$
Bottom wall y^+	1.09	1.09	1.09
Vertical wall y^+	4.95	2.50	1.25

Table 4: y^+ values for vertical and bottom walls for the LRN simulations

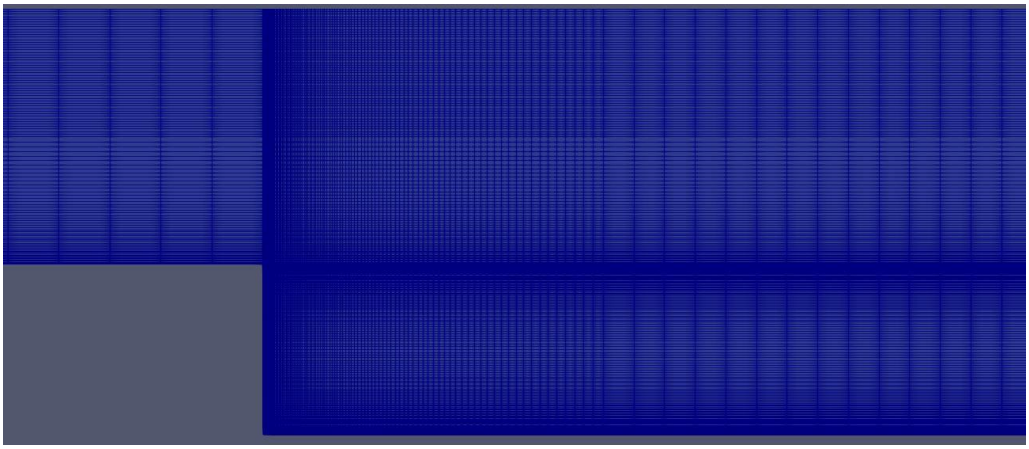

Figure 5.10: Mesh of $5.0x10^4$ cells close to the step (LRN approach)

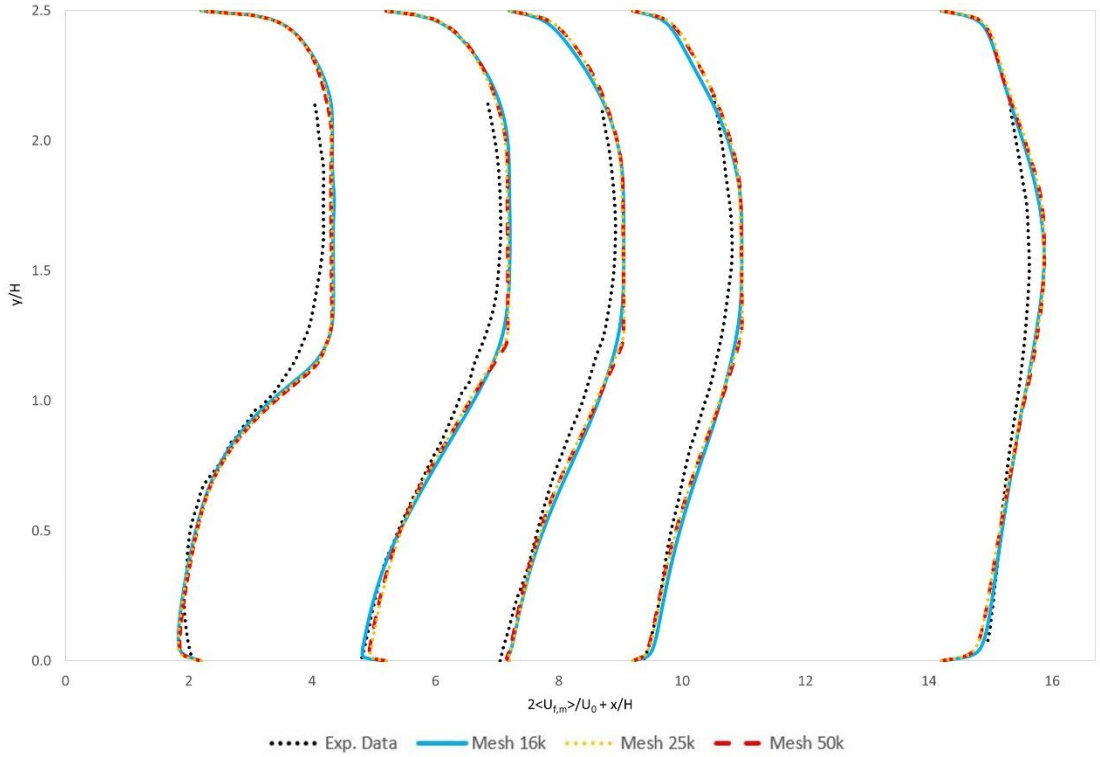

Figure 5.11: Comparison of the time-averaged flow profiles (continuous phase) for the streamwise velocity ($U_{f,m}$)in the backward-facing step flow with the experimental data* [38] *at x/H = 2, 5, 7, 9, 14 (LRN approach).

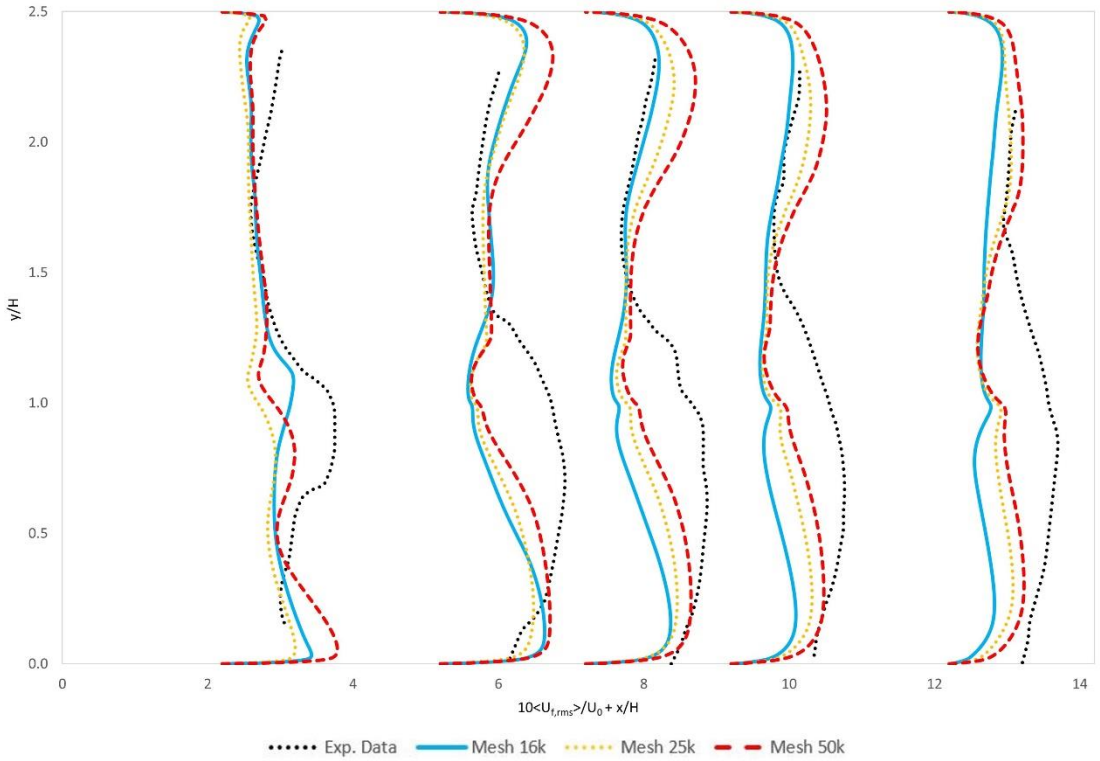

Figure 5.12: Comparison of the time-averaged flow profiles (continuous phase) for the streamwise velocity fluctuations ($U_{f,x,rms}$) in the backward-facing step flow against the experimental data* [38] *at x/H = 2, 5, 7, 9, 14 (LRN approach).

In Fig. 5.11 the mean fluid velocity is shown. As in the HRN method, the mean velocity is not changing significantly as the mesh becomes finer and is in good agreement with the experimental data. In Fig. 5.12, the fluctuations in fluid velocity are depicted. It is noted that for the finer mesh simulations, the curves are moving to the opposite side as expected (away from the experimental data). At the far-field, the velocity profile is almost vertical but not far from the benchmark curve. We can conclude that quantity and quality-wise the wall functions method provides much more satisfactory results. Therefore, this is the method to be used for the particle-laden simulation case.

5.3.2 Particle-Laden Flow

The BFS channel model is used here to investigate a particle-laden flow simulation. In addition to the previous case study, spherical copper particles are inserted randomly in the inlet of the channel. The particle parameters are given in Table 5.

Particle parameter	Value
Mass-averaged diameter d_p	70 μm
Density ρ_p	8800 kg/m^3
Young's Modulus E_p	1.3 x 10^{11} Pa
Poisson's ratio ν_p	0.35

Table 5: Copper particle parameter

As per Fessler-Eaton [38], the mass load ratio of the injected particles is $\beta = \dot{m}_d/\dot{m}_c = 0.1$. This gives a dispersed phase volume fraction of $\alpha_d < 10^{-3}$, therefore a two-way coupling is considered in this simulation case [39]. On Fig. 5.13, the time-averaged fluctuation velocity profile of the particle-laden simulation is shown. The mesh used is the fine grid used on the unladen case.

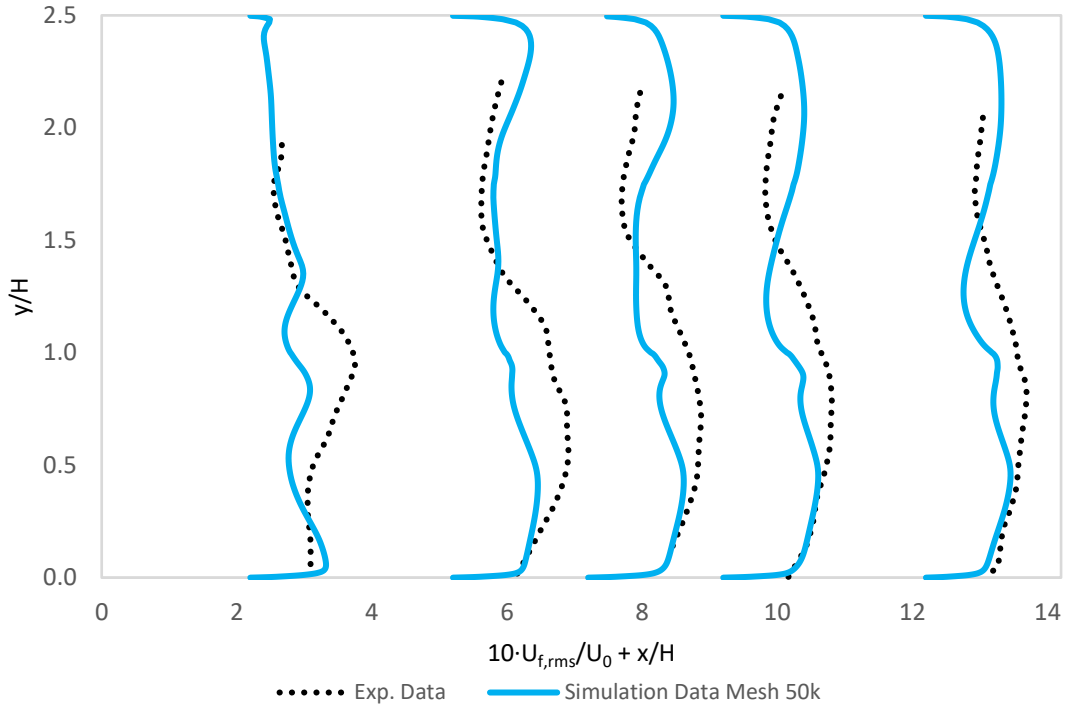

Figure 5.13: Comparison of the time-averaged flow profiles (continuous phase) for the streamwise velocity fluctuations ($U_{f,x,rms}$) in the backward-facing step flow against the experimental data* [38] *at x/H = 2, 5, 7, 9, 14 for particle-laden flow

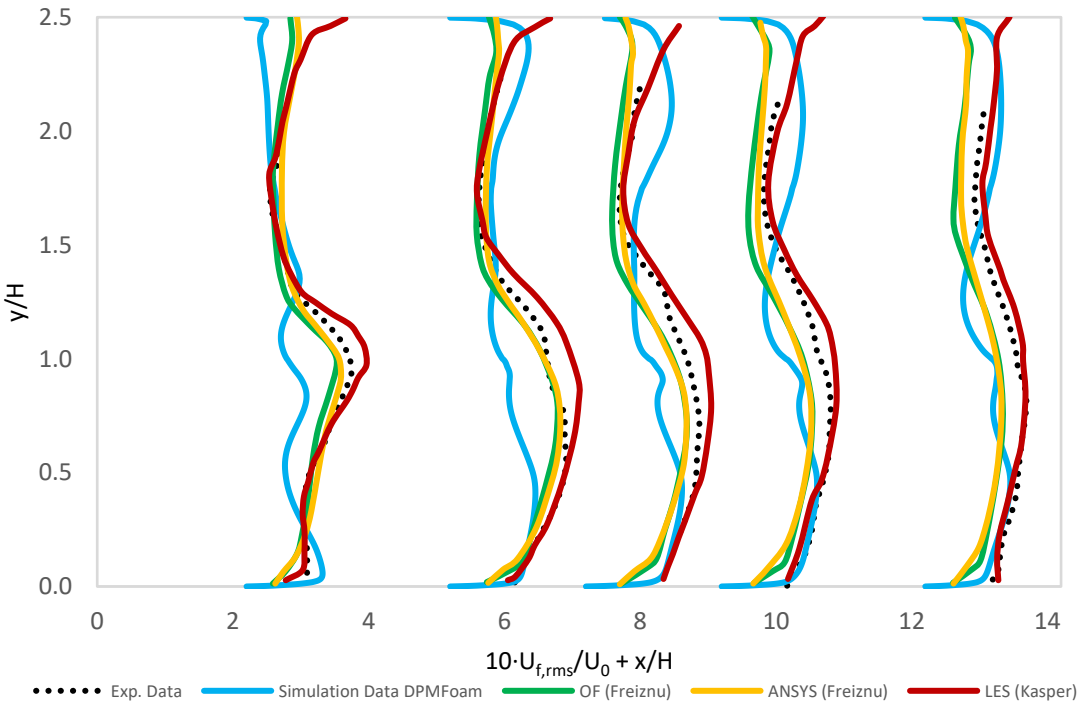

***Figure 5.14: Comparison of the time-averaged flow profiles (continuous phase) for the streamwise velocity fluctuations ($U_{f,x,rms}$) in the backward-facing step flow against the experimental data* [38], *OF and ANSYS k-ωSST simulation* [40] *and OF LES simulation* [39].**

The mean (Fig 5.15) and fluctuation (Fig. 5.17) velocity profiles are given below. For comparison, the mean velocity distribution of the LES simulation [120] is shown as well (Fig. 5.16).

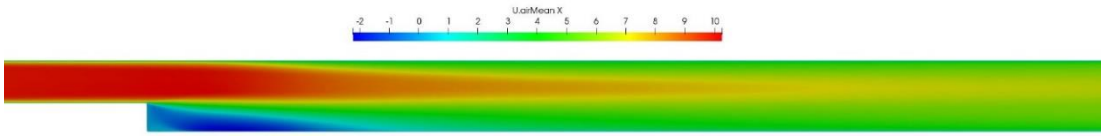

Figure 5.15: Fluid mean velocity distribution with the presence of 70µm copper particles k-ωSST simulation

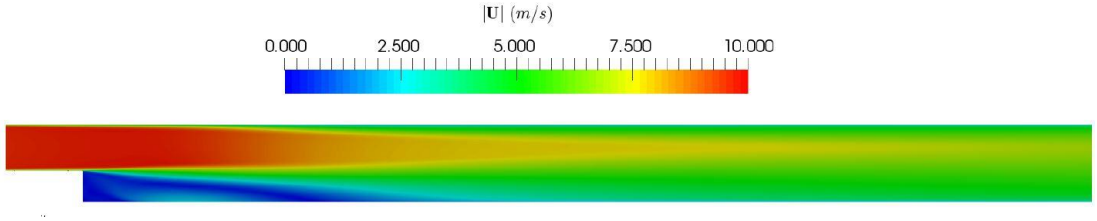

***Figure 5.16: Fluid mean velocity distribution with the presence of 70µm copper particles of LES simulation* [120]**

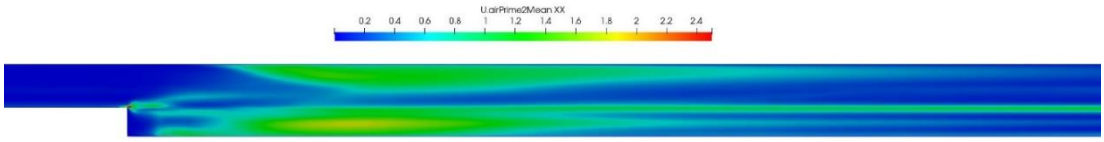

Figure 5.17: Fluid fluctuation velocity distribution with the presence of 70µm copper particles k-ωSST simulation

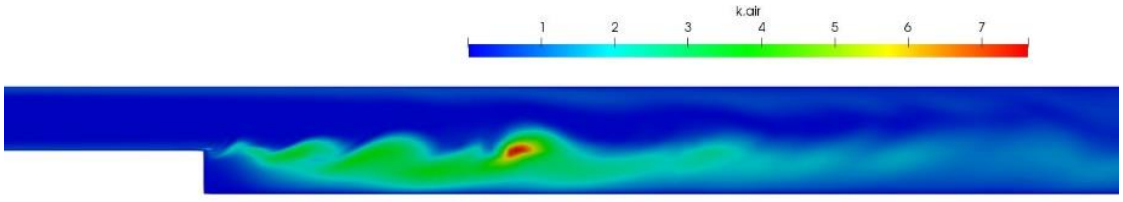

Figure 5.18: Fluid turbulence kinetic energy k distribution with the presence of 70µm copper particles k-ωSST simulation

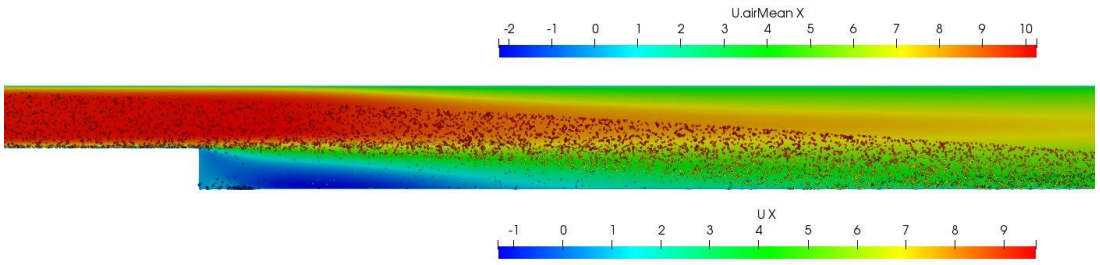

Figure 5.19: Particle distribution in the channel k-ωSST simulation

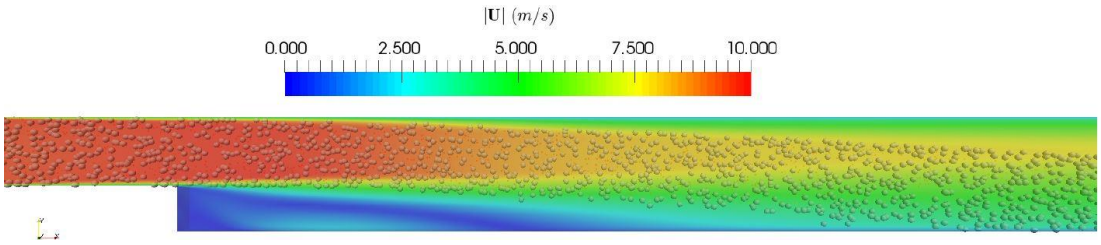

Figure 5.20: Particle distribution in the channel of E-L simulation **[120]**

5.3.3 Discussion and Conclusions

The BFS simulation study case conducted in this chapter has been provided useful information for the Lagrangian solver utilised. In both unladen and particle-laden simulations, the mean velocity agrees very well with experimental data. Directly behind the step, a recirculation zone is created where backflow occurs. In this area, a discrepancy of 7% between the simulation and experimental data occurs to the bottom wall while further to the main flow the deviation is smaller. Focusing further downstream, the deviation of velocity close to the wall is in the region of 1% (Fig. 5.11). Moreover, the capture of the vortices that arise in the recirculation region are in very good agreement with experimental data (Fig. 5.8 and Fig. 5.9, respectively).

The root-mean fluctuations profile in the RAS unladen simulations provide a satisfactory qualitative result. However, the difference in amplitude between the simulation results and experimental data is visible. The solver does not capture the velocity fluctuations in the x-direction with great precision. However, near the bottom wall the variation is quite small whereas the main variation occurs in the main flow region between x/H = 1.5 – 2.25 (Fig. 5.13 and Fig. 5.14). The fluctuating velocity distribution over the BFS channel is shown in Fig. 5.17.

Fig. 5.18 shows the turbulent kinetic energy (TKE) distribution in the channel. The TKE indicates the energy content of eddies in the turbulent flow. Therefore, the higher values of TKE in the flow region, the higher the eddy energy which is derived from the mean flow. In this case, the high TKE distribution is observed between the step tip area and recirculation region where the mean velocity is reduced following the time-averaged boundary line (Fig. 5.1). Fig 5.19 shows the particle distribution in the channel which is in good agreement with the literature (Fig. 5.20). The simulation results of this study show that the particles are following faster to the bottom wall as

the result of the drag, lift and added mass forces whereas the literature results consider only drag force.

The particle-laden RAS simulation improves the velocity fluctuations profile qualitatively and quantitatively. The fluctuations in the near-wall region are in good agreement with the experimental data while the quality of the curves has been improved in the far-field as well. Moreover, the particle trajectories and distribution are quite satisfactory compared to similar simulations using the LES turbulence model. Overall, the DPM solver can provide quality results for particle-laden flows particularly in the near-wall region, however, there is some discrepancy in the fluctuation solution of the results. Nevertheless, for an unresolved large number of particles flows the results are quite reliable in a sense of the mean and fluctuation velocity and the particle distribution into the channel. That gives confidence for utilising the DPM solver to carry out the erosion study.

6 Erosion modelling in cavities

6.1 INTRODUCTION

In this chapter, the erosion prediction in cavities is carried out. This is an extension of the BFS that has been investigated in the previous chapter is carried. Here the numerical simulation of the erosion rate due to the presence of the particles is examined. The Finnie model that has been integrated into the DPMFoam solver is used. In the first part, the simulated erosion rate prediction is compared with a numerical solution from the Lin et al. [82] study. In the second part, the erosion prediction of an annular cavity is carried out. The resulted material removal due to the particle erosion is examined for the BFS and the Forward-Facing Step (FFS) and it is compared to experimental data.

6.2 RECTANGULAR CAVITY EROSION PREDICTION

6.2.1 Problem description

The current study presents an erosion simulation analysis on a rectangular cavity similar to the BFS shown by the Fessler and Eaton [38] geometry. The rectangular cavity structure is given in Fig. 6.1. The geometry will be approximated by a two-dimensional (2D) domain and the computational results are compared with the one presented by Lin et al. [82]. For the equal height step, the particles hit the aft wall and rebound into the cavity through the vortex created as shown in the backward-facing step study (Fig. 5.8). Therefore, the aft wall will be investigated for the maximum erosion that occurred. For the general flow evolution on the backward-facing step, the reader can refer to Fig. 5.1

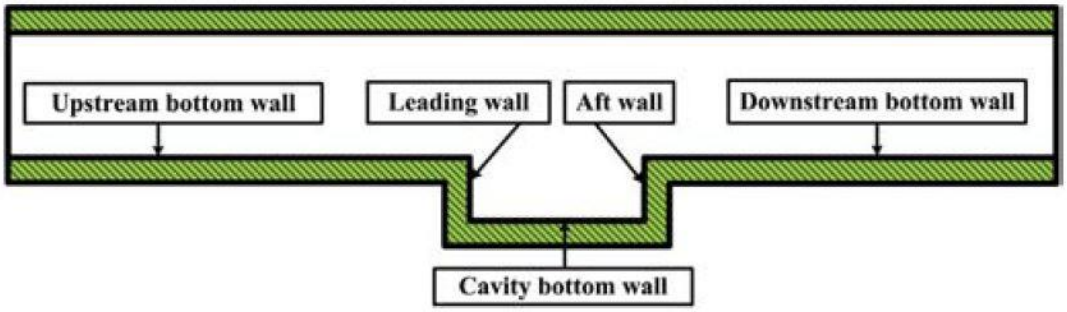

***Figure 6.1: Structure of an ideal cavity whose leading and aft wall have the same height* [82]**

6.2.2 Rectangular Cavity Erosion Simulation Case

The channel height S is 40mm and the leading wall height H is 26.7mm. The cavity upstream and downstream is 32S = 1,280mm and 35H = 934.5mm respectively, to obtain fully developed turbulence flow. The cavity length L normalized by H is constant with the value of 3, so that L/H = 3. The height difference h is zero so that the leading and aft walls are at the same height (Fig. 6.2). The channel geometry dimensions are given in Table 6.

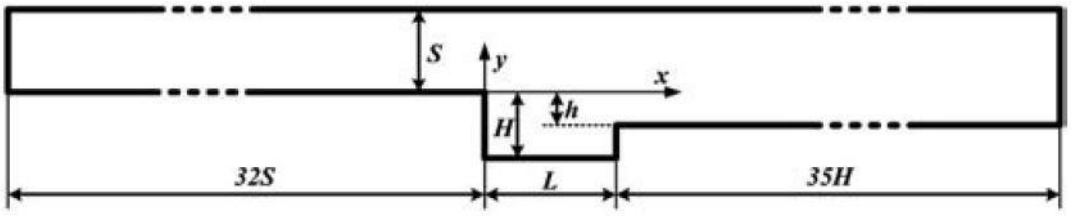

***Figure 6.2: Schematic structure of the computational domain (not to scale)* [82]**

Parameter	Symbol	Value
Channel height	S	40mm
Leading wall height	H	26.7mm
Step height difference	h	0mm
Cavity length	L	80.1mm

Table 6: Channel characteristic dimensions

The gas inlet velocity is set as 9.3 m/s which meets the centreline velocity of 10.5 m/s for a fully developed flow. At the wall boundaries, the velocity components are set as a no-slip shear conditions. The erodent material is sand of 2,500 kg/m^3 density. The particles are inserted once the flow is fully developed after 1s at a rate of 80,000 particles per second. The channel walls material is carbon steel and is assumed smooth. The material constants for the carbon steel required to calculate the plastic

flow stress as per Eq. 3.49 are given as K_p = 530 MPa and n_p = 0.26 [121]. Table 7 provides the flow and erodent and wall material characteristic parameters.

Parameter	Symbol	Value
Bulk air velocity in channel	U	9.3 m/s
Air pressure	p_f	1.01×10^5 Pa
Air density	ρ_f	1.225 kg/m^3
Air dynamic viscosity	μ	1.5×10^{-5} Pa·s
Air kinematic viscosity	ν	1.2245×10^{-5} m^2/s
Reynolds number	Re	18,400
Erodent feed rate	G_0	80,000 particles/s
Erodent particle density	ρ_p	2,500 kg/m^3
Erodent particle diameter	d_p	50μm
Material Young's modulus	E_m	2.05×10^{11} Pa
Material Poisson's ratio	ν_m	0.295

Table 7: Flow and material characteristic parameters

The PIMPLE algorithm is used to solve the gas phase equations. A structured mesh is used. The k-ωSST turbulence model is used to provide the additional transport equations for the turbulence flow. The smallest cell size is selected to provide the log-law method so that the centroid of the cell adjacent to the wall falls into the logarithmic sublayer ($30 < y^+ < 200$). The second-order discretisation scheme is used for the pressure gradient, convection and divergence terms. The lagrangian tracking scheme is used for the particle phase where the motion equations are integrated with a higher-order scheme. The linear Eulerian discretised systems were solved by a Pre-conditioner Conjugate Gradient (PCG) solver with Particle-In-Cell (PIC) pre-conditioning for pressure. This is faster than standard methods by solving first on coarser meshes. A Gauss-Seidel smoothing solver for velocity is used only to reduce residuals.

The transient simulation time step varies to achieve a Courant number Co ≈ 0.99 with a minimum value of 5×10^{-4} s. Initially, the gas flows into the channel without the presence of the particle for a time of 1s to achieve a steady fluid phase. Then, the particles are inserted into the channel for the remainder of the simulated period. The total flow time is 2.5s to match the literature data, with a total of 120,000 particles included in the simulation. At that period, the erosion is assumed arbitrary steady. The erosion prediction data was computed and acquired during 1.5-2.5s. This happens

because the particles need about 0.5s to reach and contact the aft wall surface. The erosion rate is defined as the mass eroded per unit area and time [kg/m^{2}s].

The first step is to investigate the mesh independence test for three different meshes using the Finnie model from the OF library and doing the same thing and comparing the results with the Finnie model developed (see Section 3.4.2). Then, adopting the best grid results for each model, these are validated compared with the simulation data from the Lin et al. study [82]. As mentioned above, the computational domain is 2D and three grid densities were investigated: 15,000, 29,500 and 45,000 cells. The results for the erosion prediction of the aft wall of the three meshes against the selected curve from Lin [82] for each model is given in Fig. 6.3-6.5. The x-direction shows the dimensionless distance y of the aft wall distance defined as $y = y_i/H$ where y_i is the local height on the wall using the coordinate system in Fig. 6.2 and H the total wall height as defined above and equal to 26.7mm. Therefore, the zero point is at the top of the aft wall and -1 the cavity bottom wall (Fig. 6.2).

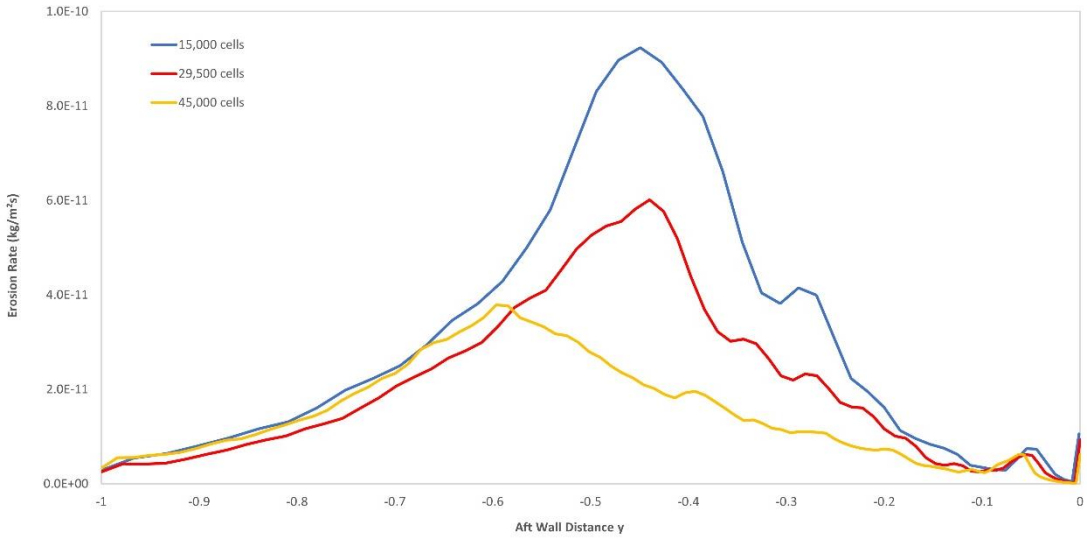

Figure 6.3: Erosion rate comparison on the aft wall of cavity for various grid numbers for Finnie model from OF library

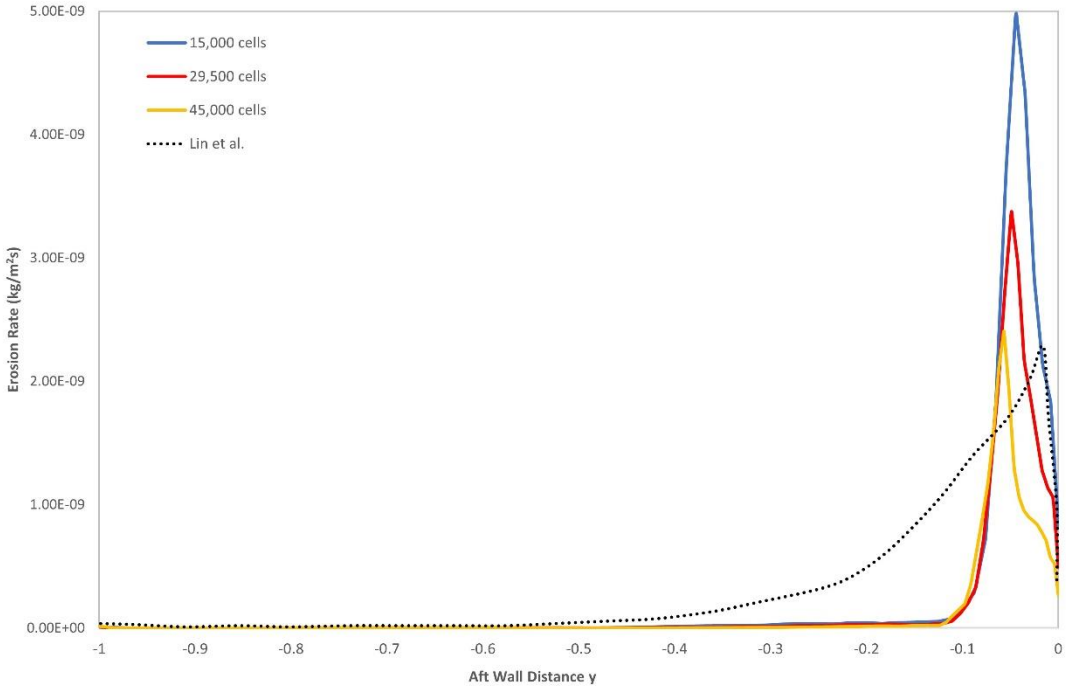

Figure 6.4: Erosion rate comparison on the aft wall of cavity for various grid numbers for developed Finnie model

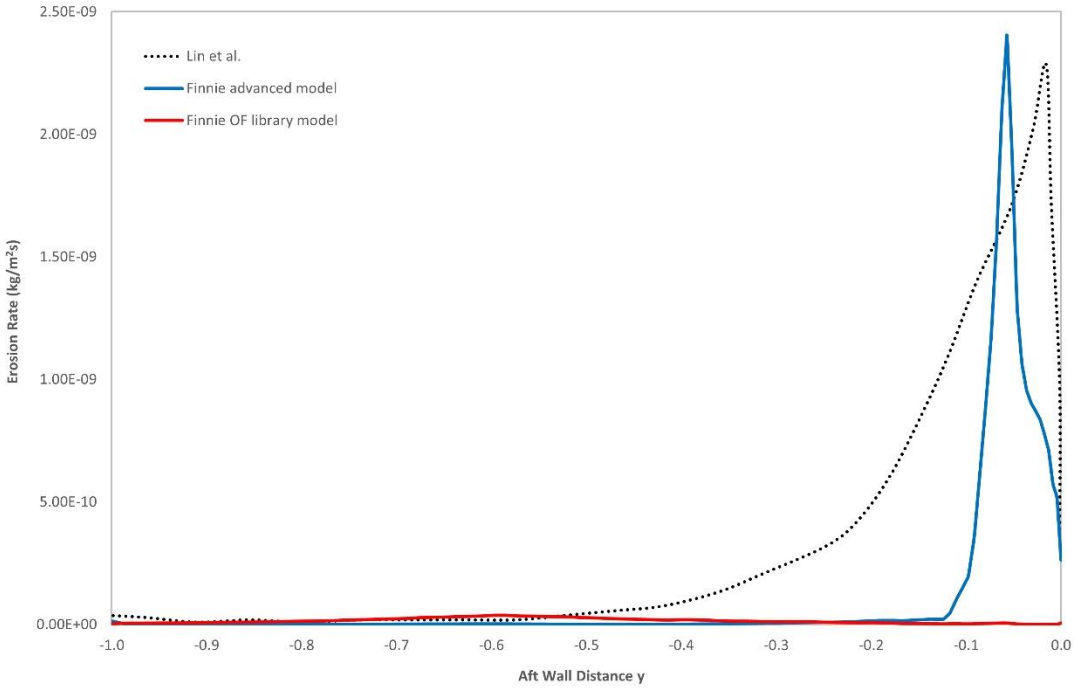

Figure 6.5: Erosion rate comparison on the aft wall of cavity for finer grid numbers for Finnie models against Lin results **[82]**

The standard Finnie model (Fig. 6.3) is not capturing the erosion on the aft wall top corner as expected. The maximum erosion rate is happening at the middle of the

wall and the magnitude is on the order of 10 less. On the other hand, the developed Finnie model (Fig. 6.4) successfully captures the damage at the aft wall. As the mesh is increased, the maximum erosion spike is shifted lower and it agrees quite well with the literature. However, it fails to capture the erosion in the region lower to the top wall area having a steeper ramp up from low erosion to the maximum. The difference between the three models is shown in Fig. 6.5.

6.2.3 Variable Step Height Erosion Simulation

The influence of the step height h is studied in this section. The step height is varied from 0.2 to 1 and the analysis of the gas phase flow and wall erosion rate by the dispersed phase is carried out. Despite the particle phase is being accounted for in the simulation model, the gas phase state downstream is not changed significantly due to the low mass flux ratio and particle diameter. The main change in the gas phase occurred in the cavity vortex structure. Fig. 6.6 shows the streamlines of the velocity in the x-direction for various step height differences and indicated the different vortical structures that exist.

As shown in the backward-facing step case, a shear layer is separated from the leading wall and imposed on the aft wall when the step height difference is low or re-attaches the airflow when the step is quite small or does not exist. This shear layer forms two vortices the main and the secondary and rotate in opposite directions. The secondary vortex is almost equal to the main for the equal step height and diminishes as the step height increases.

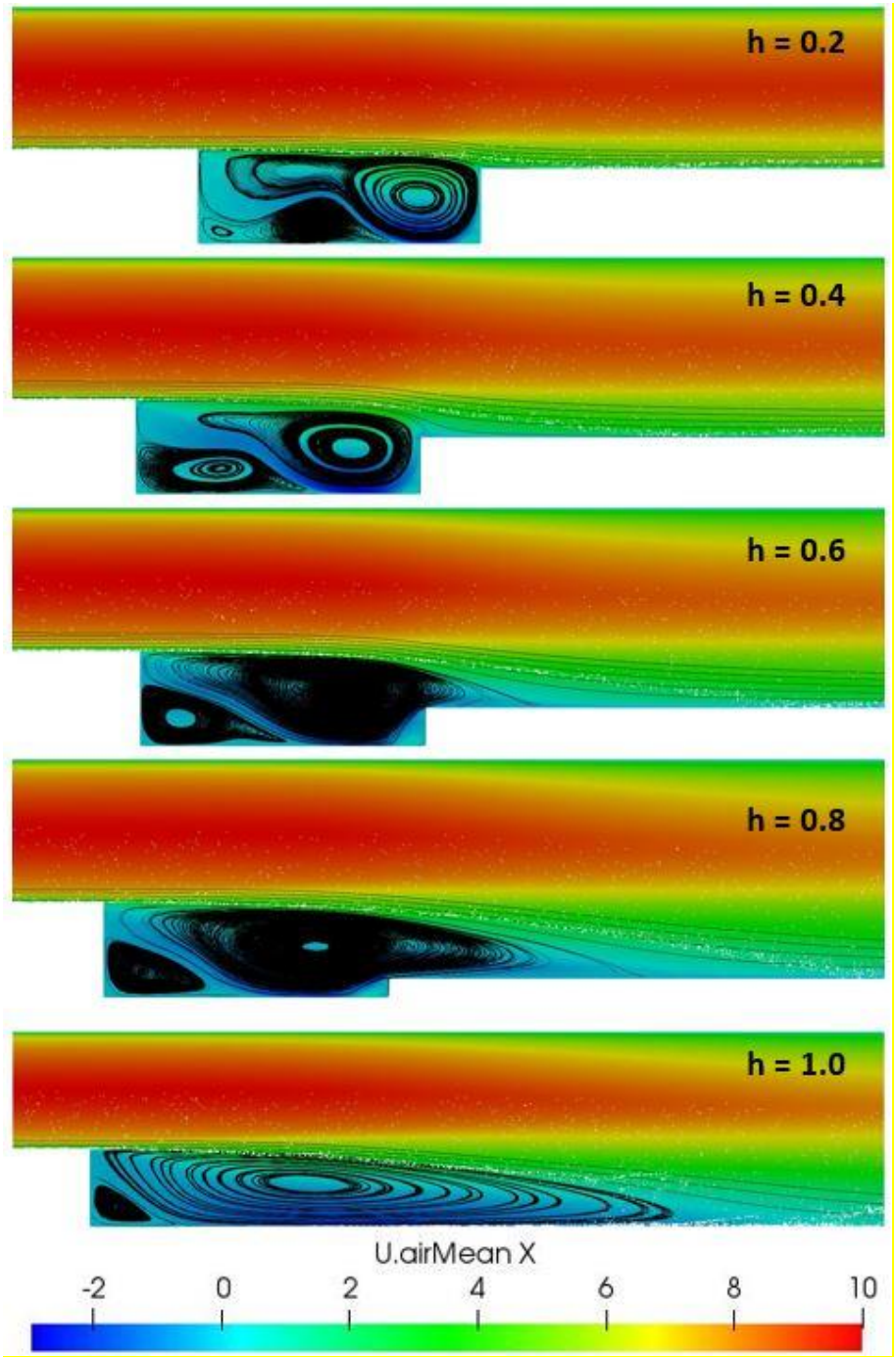

Figure 6.6: Gas phase streamlines and velocity in x-direction

To investigate further the shear layer reattachment phenomenon, the reattachment length is derived for the various step heights at the location where the intersection of the main flow and recirculation flow at the bottom downstream wall (Fig. 6.7). The literature data from [82] are also taken for comparison. The attachment length is about constant to 3 for $0.2 < h < 0.4$ and then there is a uniformly increased to the maximum of 7.5 for the $h = 1$. The reattachment length from experimental data

[38] for h = 1 is 7.4 which agrees quite well, whereas the maximum from Lin [82] is 8.

As the main vortex overflows the cavity, backflow is developed on the leading wall of the downstream bottom wall. The maximum backflow velocity at the position x = 2.5 for each of the step height differences h is extracted to analyse the influence of h on the swirling velocity (Fig. 6.8). It is shown that for the small heights h the backflow velocity decreases and then remains constant for h > 0.6. This could be caused by the combined influence of the vortices created and the cavity walls.

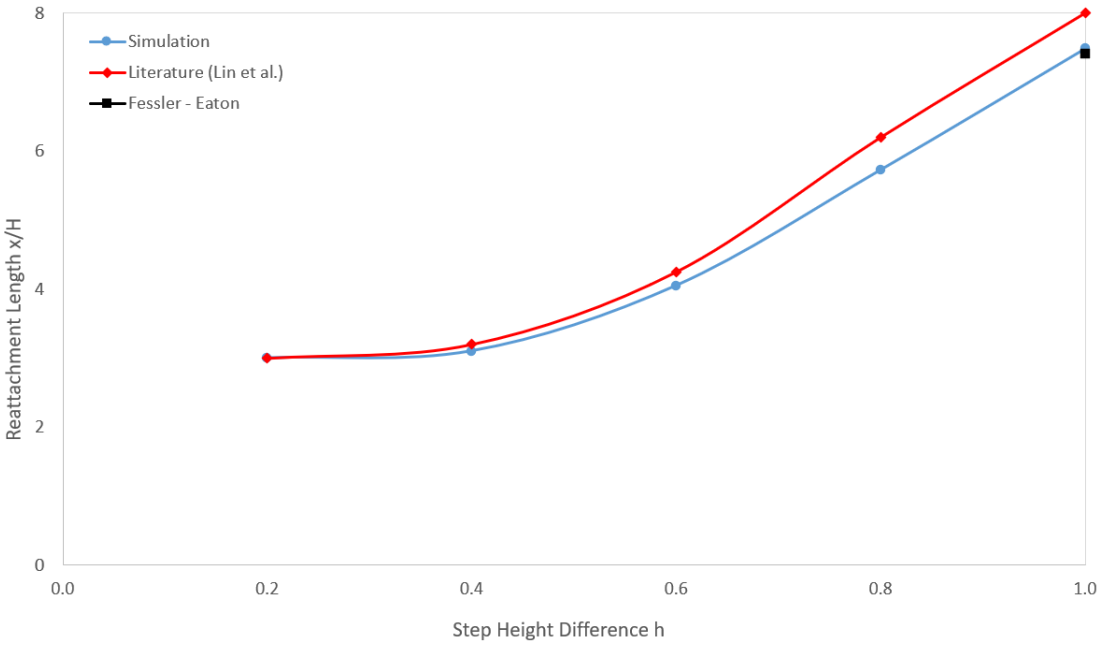

Figure 6.7: Shear layer reattachment length as function of the step height difference h

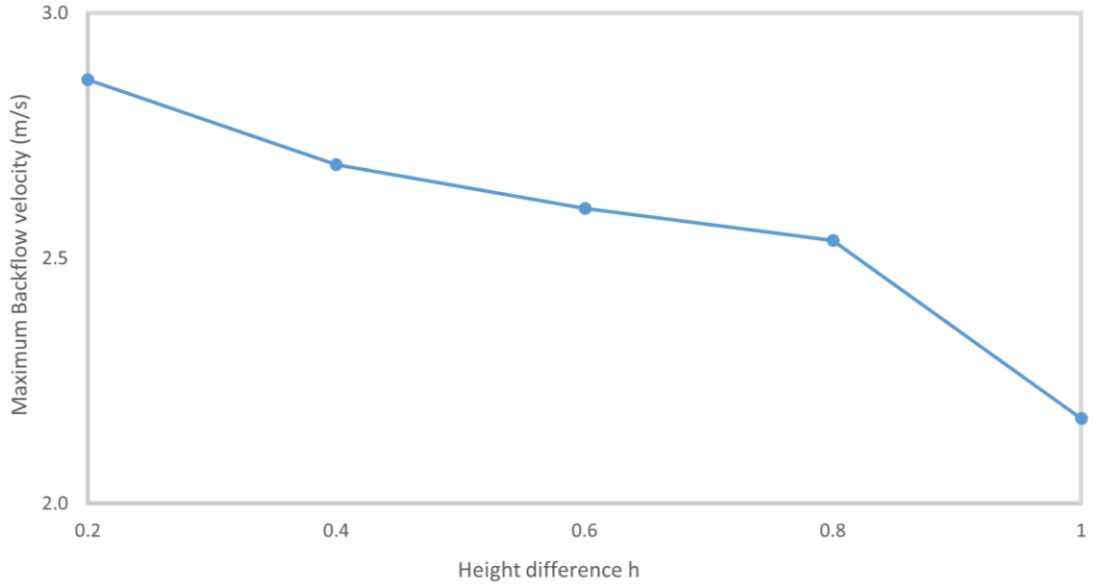

Figure 6.8: Maximum backflow velocity as function of the step height difference h

The particles distribution for various heights h is shown in Fig. 6.9. The particles cannot respond to the fluid motion, therefore their trajectory is controlled mainly by gravity. For the equal height step, the particles hit the aft wall and rebound into the cavity through the main vortex as shown in the previous case. As the height difference h increases the particles collide on the downstream bottom wall.

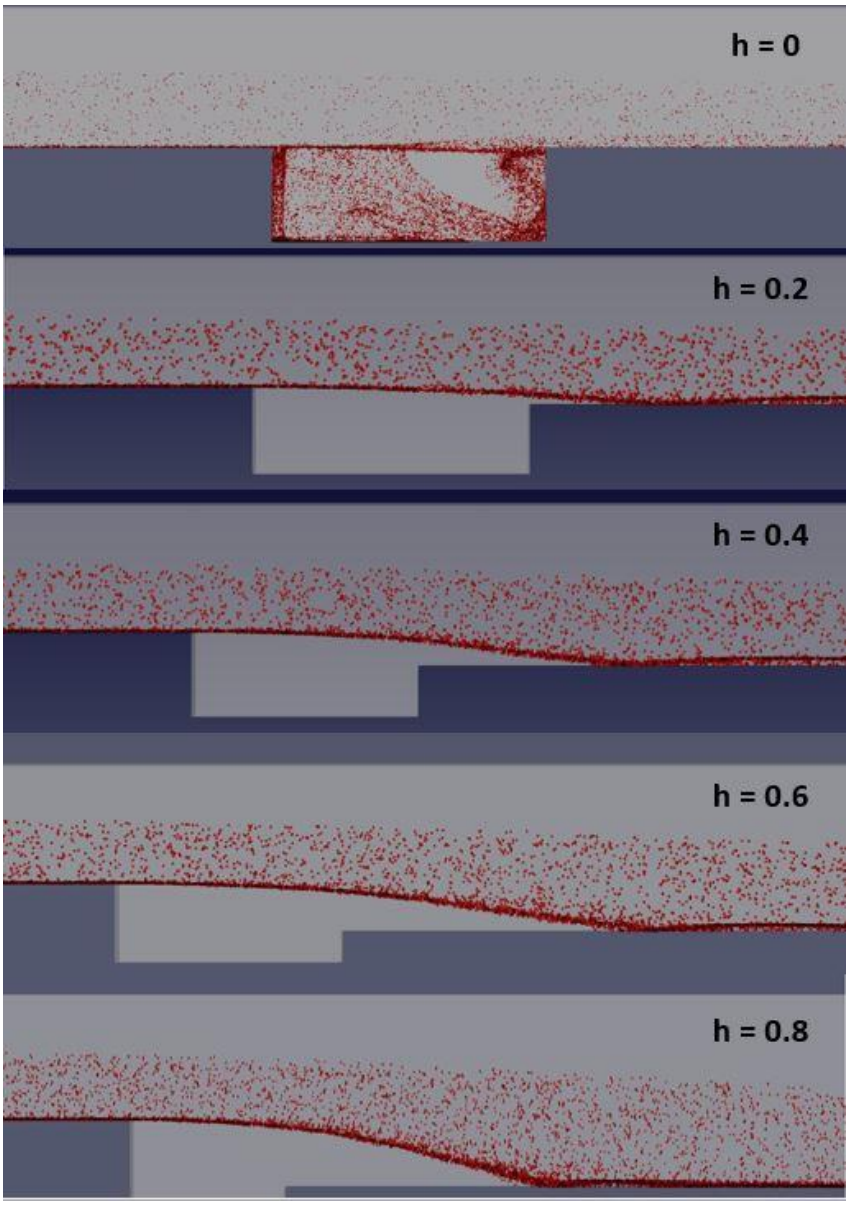

Figure 6.9: Particle distribution for various step height differences

For the $0.2 < h < 0.8$, the downstream bottom wall of the cavity will be investigated for erosion. The influence of height difference h on the erosion rate distribution is examined by extracting the erosion data across the downstream bottom wall of the cavity and normalised by the maximum value of erosion from each case

that occurred (Fig. 6.10). The zero-distance reference in the x-axis is the start of the downstream bottom wall (the cavity corner with the aft wall).

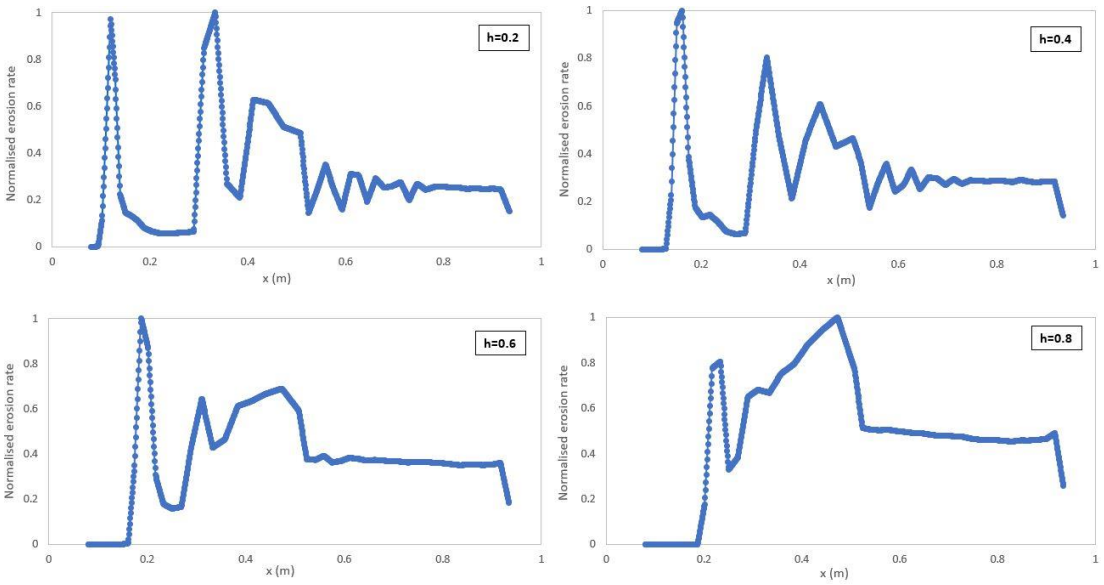

Figure 6.10: Normalised erosion rate across downstream bottom wall for various step height differences h

For 0.2 < h < 0.8 the particles are distributed and impact mainly along the downstream bottom wall. The maximum impact and the maximum erosion rate occurs on the lower wall, after the cavity on the downstream lower wall due to the parabolic trajectory of the particles. It is noted that three regions can be identified on each plot. The first one is from 0 to 0.3m where there are two spikes of the erosion rate. This is the area where most of the particles impacted the bottom wall. Hence, the maximum values of the erosion rate have occurred. The next region is between 0.3-0.7m for h=0.2 and h=0.4 and between 0.3-0.5m for h=0.6 and h=0.8. In this region, a fluctuating erosion occurs with areas of higher and lower impact. After this region, a constant erosion rate 0.2 to 0.5 happens for the rest of the wall length. In this area, the particle flow and volumes seem to have settled and the erosion doesn't change with the distance.

6.3 PIPE CAVITY EROSION SIMULATION CASE

6.3.1 Problem Description

This chapter regards the erosion prediction of an annular pipe cavity. This is an extension of the BFS with leading and aft wall which is a common application in industry. There are experimental data available, therefore the simulation results

evaluation can be carried out. In this cavity, the flow expands within a larger pipe diameter before it suddenly contracts into a reduced diameter pipe. This type of cavity is commonly found in the oil and gas industry. The computational results are compared with experimental and simulation data from the literature. The experimental data are extracted from an apparatus as shown in Fig. 6.11. The geometry of the annual pipe cavity is also shown below in Fig. 6.12.

A 75kW blower draws ambient air and the airflow is determined by the pressure drop across the 200mm inlet. The particle hopper is pressurised above the back-pressure in the flow loop and the particles are fed by gravity. The sand particles (Unimin 100G) are supplied in bulk bags. To estimate the total erosion that occurred, a combination of multi-layer paint erosion experiments and surface profile measurements of the eroded surfaces was performed. Captures of the eroded paint surface and surface profiles were taken when the total erodent accumulated to 0kg (baseline), 25kg, 50kg, 75kg, 150kg and 300kg. Then the associated measurements were conducted in the forward-facing and backward-facing steps to approximate the total erosion.

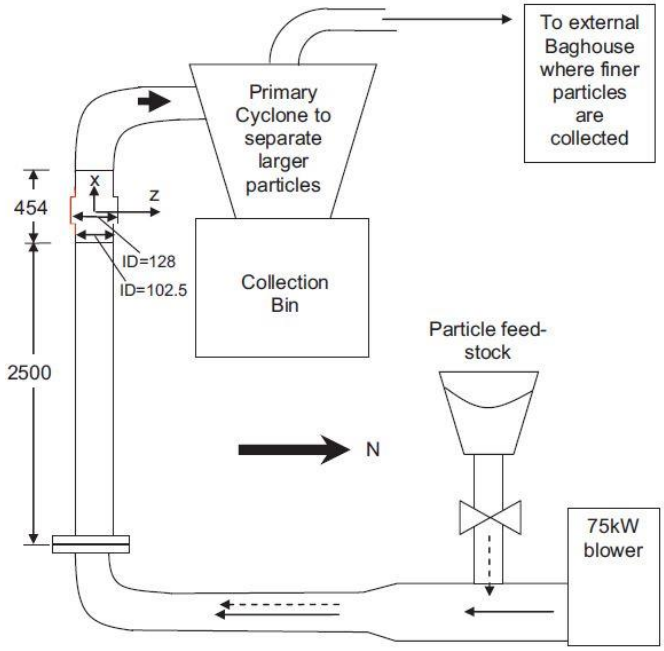

Figure 6.11: Schematic diagram of the erosion test facility with the pipe cavity (in mm) **[81]**

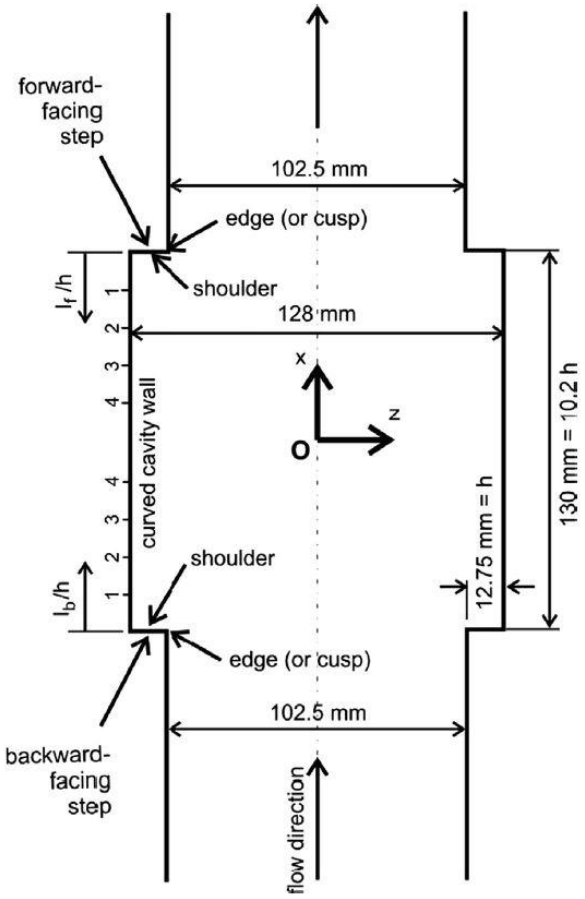

Figure 6.12: Schematic diagram of the annular pipe cavity. Flow is upward **[81]**

The experimental conditions are given in Table 8.

Parameter	Symbol	Value
Bulk air velocity in channel	U	80 m/s
Air pressure	p_f	1.01×10^5 Pa
Air density	ρ_f	1.196 kg/m^3
Air dynamic viscosity	μ	1.83×10^{-5} Pa·s
Air kinematic viscosity	ν	1.53×10^{-5} m^2/s
Reynolds number	Re	5.36×10^5
Mean particle velocity	u	62.5 m/s
Erodent feed rate	G_0	0.03 kg/s
Erodent particle density	ρ_p	2,700 kg/m^3
Erodent particle mean diameter	d_p	50μm
Material Young's modulus	E_m	6.9×10^{10} Pa
Material Poisson's ratio	ν_m	0.335

Table 8: Flow, erodent particles and pipe wall properties

6.3.2 Pipe Annular Cavity Erosion Prediction

The data for the erosion prediction on the forward and backward-facing steps are established by converting the linear mass removal rate indicated as the surface depth

removed per unit time and then averaging around the circumference of the annular test section. Therefore, the radial profile of mass removal is calculated for both steps and the axial profile is calculated for the cavity surface. The given CFD prediction profiles are compared with the experimental and simulation data from the publication (Fig. 6.15 and Fig. 6.16).

The solution procedure is implemented in two stages. Initially, the gas phase air is introduced into the pipe and the Eulerian simulation calculations are performed throughout the geometry. The standard k-ωSST model is used for turbulence prediction. Once the steady fluid phase is achieved, the particles released from the inlet and the Lagrangian techniques are used to track their trajectories. The accumulated mass removal of the forward and backward-facing step is calculated at the end step.

The axial flow through the pipe represents the bulk of the flow field which accelerates as the pipe diameter reduces to 102.5mm and the flow separation and recirculation occurred on the 90 degrees bends. The mean flow velocity at the cavity section is approximately 80 m/s whereas the mean particle velocity is 62.5 m/s. The recirculation predicted in the cavity has an approximate air velocity of 20 m/s. The mean velocity profile in the cavity is shown in Fig. 6.13.

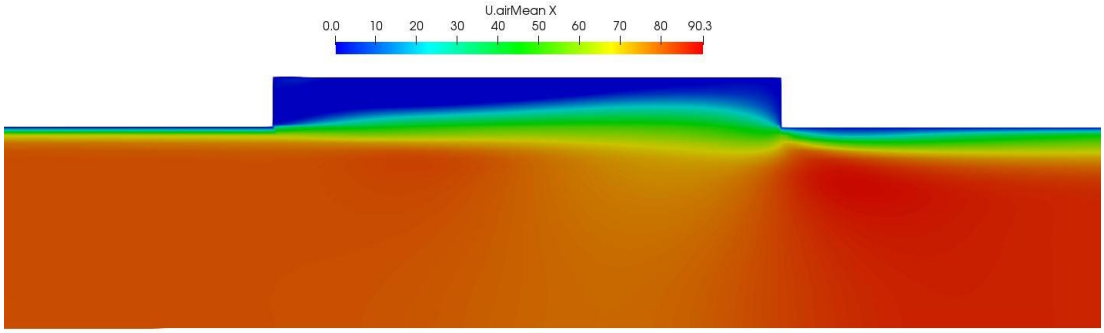

Figure 6.13: Fluid mean velocity profile in x-direction on the cavity

The air velocity distribution in the test section is shown in Fig. 6.14. It shows the recirculation points on the forward and backward-facing steps. The flow has a small recirculation region at the cavity entrance and is forced back into the pipe on the forward-facing step (back arrows drawn in the cavity).

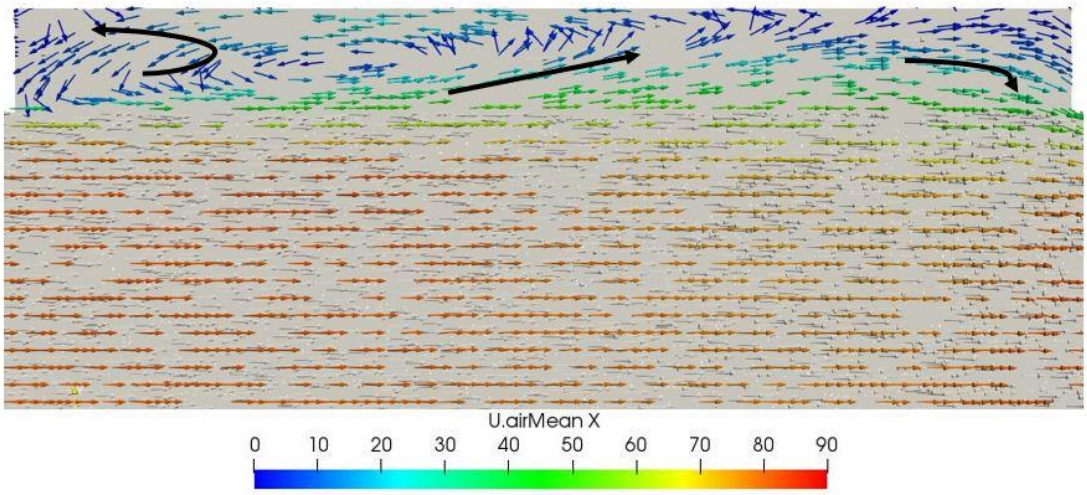

Figure 6.14: Air velocity distribution through the cavity section (pipe section is shown in horizontal position)

As mentioned, the erosion data averaged around the circumference of the test section and the radial profile of the linear mass removal rate are calculated for the forward and backward facing surfaces. The simulated data are compared with the experimental and computational results in Fig.6.15 for the forward-facing step and Fig. 6.16 for the backward-facing step. The computational analysis is carried out for the exposure of the entire 300kg of erodent Unimin 100G and presented as the 0-300kg line (black dots) in the graph. This is the case that CFD erosion prediction implemented from the author denoted by blue dots as well as in the literature [81] which is denoted by the white circles.

The material removed from the cavity surface in the forward-facing step is of the order of 20 in magnitude greater than that on the backward-facing step. This is reflected in the computational results both from this study and from the literature. For the forward-facing step, the CFD prediction of the maximum material removal rate is 3.56 mm/day and occurs at a radial distance of 51.89mm. This is in good agreement with the experimental data (2.96 mm/day at 51.40mm) as well as the issued computational prediction (3.88 mm/day at 52.69mm). However, the erosion modelling under-predicts the mass removal magnitude at locations higher in the cavity wall. In the current study, the linear mass removal rate has a steep increase from a radial distance of about 53mm up to the maximum point and starts to decrease whereas in the experimental data the mass removal rate happens earlier at about 58mm. This is captured in the simulation by Wong et al [81] but there is a steep increase at about 57mm which does not correlate to the experimental curve.

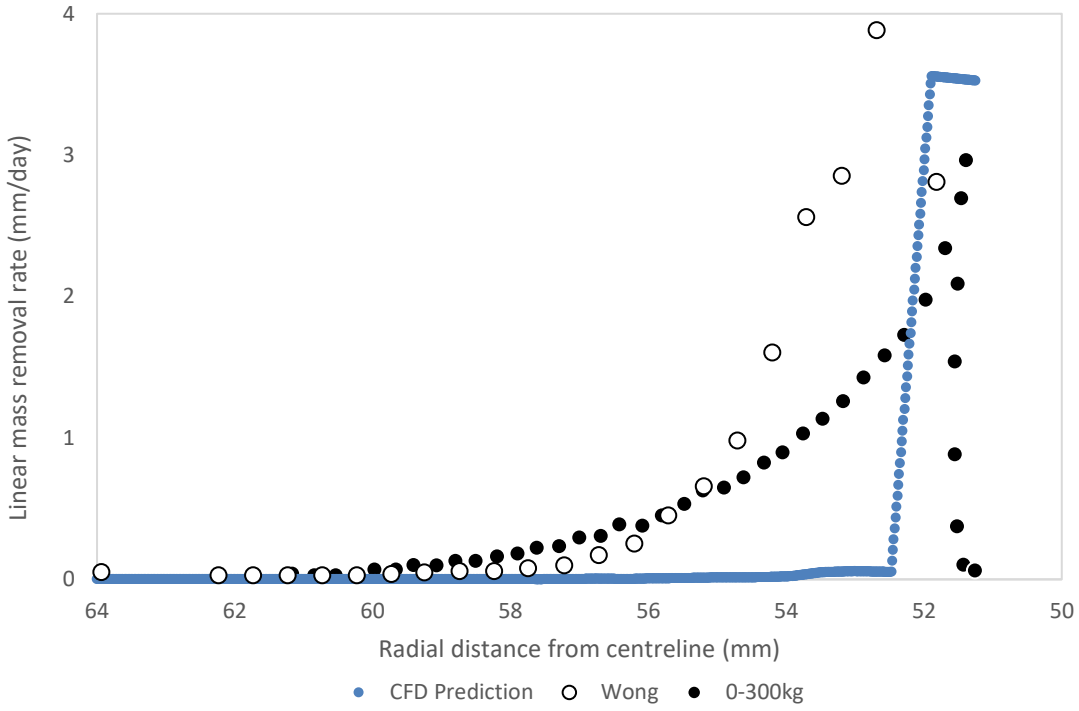

Figure 6.15: Radial distribution of linear mass removal rate on the forward-facing step with Unimin 100G erodent and upstream flow

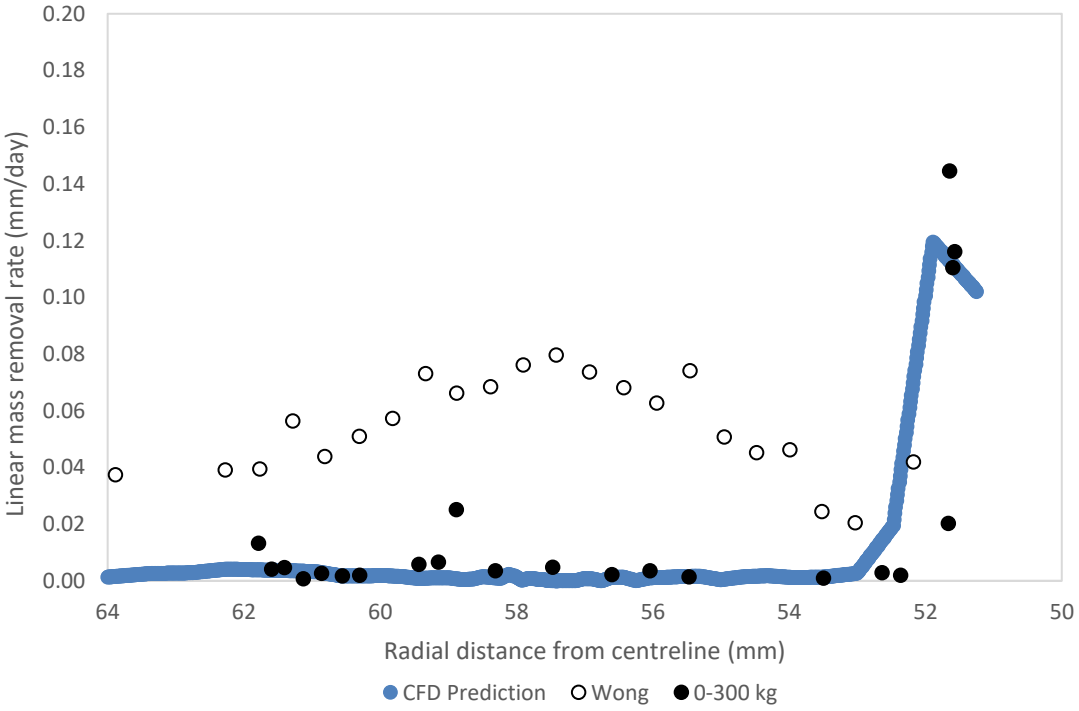

Figure 6.16: Radial distribution of linear mass removal rate on the backward-facing step with Unimin 100G erodent and upstream flow

In Fig. 6.16 the backward-facing step linear mass removal rate is shown in a similar fashion. Here the erosion modelling is following very well the experimental data (black dots). The maximum mass removal rate is 0.119 mm/day at 51.86mm radial

distance (0.145 mm/day at 51.65mm in the experiment). Some individual experimental points do not follow the trend as shown in the graph. These are not fully captured from simulation which adheres to a more linear curve. Computational results by Wong have a significant deviation from the CFD erosion modelling of this study and experimental data. There is a higher mass removal rate at a radial distance of 64-53 mm and the maximum removal rate occurs at about 57.5mm.

Overall, the agreement of computational erosion prediction is good for both steps of the cavity. The CFD modelling inaccuracies can be summarised as below:

- The 2D geometry of the test section is giving a good approximation of the flow and erosion of the cavity surfaces. However, a 3D modelling expansion to the whole test model can provide a better insight throughout the pipe and cavity flow and erosion.
- The experimental measurements show a change of the forward-facing profile after the exposure to the erodent. This surface change can smooth the step edges and alter the paths of particles. The computational geometry remains static, therefore it cannot capture these changes.
- The choice of the turbulence model could be important for the particle paths and flow prediction. A more elaborate turbulence modelling technique (for instance LES) could be attempted for the erosion prediction investigation.
- The erosion modelling developed and utilised in this study is one of the many models in the literature. Several other models can be used and investigate the suitability of this application.

7 Conclusions

The results of the current study have been assessed and discussed in each chapter. A summary of the main conclusions is given below.

The fluid and particles properties required for accurate modelling of the laden flows are introduced. The particle response time and the concept of the dilute and dense flows are discussed. In addition, the CFD-DEM coupling and unresolved method are presented, along with the fluid finite volume method and discretisation are examined.

The Eulerian and Lagrangian frameworks are reviewed. The main focus is the particle forces acting on the particles and the collision modelling. The single-particle sedimentation case is the starting point to review and evaluate the computational modelling of the particle behaviour. The main outcome is the capture of the particle forces and the particle-wall interactions. It is shown that the unresolved CFD-DEM method can capture sufficiently the particle motion in a fluid and the primary forces such as drag, lift and virtual mass are well evaluated. The main limitation here is that an important force of the relatively large particle in sedimentation, the lubrication force becomes significant and is not captured by the existing solver. The integration of this force into the solver is out of the scope of this study.

The turbulent flow in an unladen and particle-laden are investigated using the common geometry case of the Backward-Facing Step. The mean and fluctuation velocities of the fluid are examined across the channel and compared with experimental and computational data from the literature. Moreover, the re-circulation area around the step is investigated and well captured in terms of the vortices created. This is the main contribution of the study on this case. RAS modelling is used to capture the flow phenomena. This is quite acceptable on the near-wall which is the main focus of the study. The incorporation of the more accurate LES modelling would be recommended for further analysis.

A comprehensive review of the erosion prediction modelling is presented. The main contribution of this work in this area is the development and solver integration of an erosion model based on Finnie's work. The model accuracy is examined using a BFS channel and the results are compared to experimental and computational data

from the literature. Furthermore, an extension of this geometry involving an annular pipe cavity was also examined. Again, the results are evaluated against experimental and computational data. In this case, the results are well agreed with the literature. This is the primary objective of the project. As above, the incorporation of the LES modelling can be used to investigate more accuracy.

8 Recommendations and future work

The following recommendations and potential future work can be directed toward researchers in the field of numerical modelling and simulation of particle-laden flows. Some recommendations derived after the completion of this study are:

- The particle forces modelling can be improved with the utilisation of the lubrication and Basset (history) forces. The lubrication force particularly could improve the dynamics analysis of the sphere close to the wall.
- The surface roughness is not accounted on this study. The influence of the surface roughness on the coefficient of restitution can be assessed.
- The vortex dynamics of the sphere particle approaching the wall can be further assessed. This requires the incorporation of the resolved coupling methods.
- The inclusion of the LES model can improve the resolution of the large eddies close to the wall, particularly behind the channel step.
- The material deformation is not captured in this study. This might have a profound impact on the predicted erosion rate and material damage. Moreover, a 3D geometry might provide a better understanding of the erosion prediction circumferentially.

Bibliography

[1] A. Lopez, M. T. Stickland and W. M. Dempster, "CFD study of fluid flow changes with erosion," *Computer Physics Communications,* vol. 227, pp. 27-41, 2018.

[2] A. Noorani, G. Sardina, L. Brandt and P. Schlatter, "Particle transport in turbulent curved pipe flow," *Fluid Mechanics,* vol. 793, pp. 248-279, 2016.

[3] H. Homann, T. Guillot, J. Bec, C. Ormel, S. Ida and P. Tanga, "Effect of turbulence on collisions of dust particles with planetesimals in protoplanetary disks," *Planets and planetary systems,* vol. 589, p. 15, 2016.

[4] A. B. Basset, A Treatise on Hydrodynamics: With Numerous Examples, London: Deighton Bell, 1888.

[5] J. Boussinesq, Therie Analytique de la Chaleur, Paris: L'Eclole Polytechnique, 1903.

[6] C. Oseen, Hydrodynamik, Leipzig: Akademische Verlagsgesellschaft, 1927.

[7] M. R. Maxey and J. J. Riley, "Equations of motion for a small rigid phere in a nonuniform flow," *The Physics of Fluids,* vol. 26, pp. 883-889, 1983.

[8] C. T. Crowe, J. D. Schwarzkopf, M. Sommerfeld and Y. Tsuji, "Particle-Fluid Interactions," in *Multiphase Flows with Droplets and Particles*, Boca Raton, FL, CRC Press, 2012, pp. 80-82.

[9] R. H. Davis, J. M. Serayssol and E. J. Hinch, "The elastohydrodynamic collision of two spheres," *J. Fluid Mech.,* vol. 163, pp. 479-497, 1986.

[10] G. G. Joseph, R. Zenit, M. L. Hunt and A. M. Rosenwinkel, "Particle-wall collisions in a viscous fluid," *J. Fluid Mech.,* vol. 433, pp. 329-346, 2001.

[11] P. Gondret, E. Hallouin, M. Lance and L. Petit, "Experiments on the motion of a solid sphere toward a wall: From viscous dissipation to elastohydrodynamic bouncing," *Phys. Fluids,* vol. 11, pp. 2803-2805, 1999.

[12] Gondret, Lance and Petit, "Bouncing motion of spherical particles in fluids," *Phys. Fluids,* vol. 14, pp. 643-652, 2002.

[13] Ardekani and Rangel, "Numerical investigation of particle-particle and particle-wall collisions in a viscous fluid," *Fluid Mechanics,* vol. 596, pp. 437-466, 2008.

[14] D. Legendre, J. Magnaudet and G. Mougin, "Hydrodynamic interactions between two spherical bubbles rising side by side in a viscous liquid," *J. Fluid Mech.,* vol. 497, pp. 133-166, 2003.

[15] Milne-Thompson, Theoretical Hydrodynamics, 5th ed., New York: Dover Publications, 1968.

[16] A. M. Ardekani and R. H. &. J. D. D. Rangel, "Motion of a sphere normal to a wall in a second-order fluid," *J. Fluid Mech.,* vol. 587, p. 163–172, 2007.

[17] Y. Zhang, G. Pan, Y. Zhang and S. Haeri, "A multi-physics peridynamics-DEM-IB-CLBM framework for the prediction of erosion by solid particle

impacts in viscous," *Computer Methods in Applied Mechanics and Engineering,* vol. 352, no. 1, pp. 675-690, 2019.

[18] Y. Zhang, B. McLaury, S. Shirazi and E. Rybicki, "A Two-Dimensional Mechanistic Model for Sand Erosion Prediction Including Particle Impact Characteristics," San Antonio, Texas, USA, 2010.

[19] K. Versteeg and W. Malalasekera, An Introduduction to Computational Fluid Dynamics, Pearson Education Limited, 2007.

[20] N. G. Deen, E. Peters, J. T. Padding and J. Kuipers, "Review of direct numerical simulation offluid–particle mass, momentum and heat transfer in dense gas–solid flows," *Chemical Engineering Science,* vol. 116, pp. 710-724, 2014.

[21] J. Smagorinsky, "General Circulation Experiments with the Primitive Equations. Part I, the Basic Experiment," *Monthly Weather Review,* vol. 91, no. 3, pp. 99-164, 1963.

[22] C. G. Speziale, "Turbulence Modeling for Time-Dependent RANS and VLES: A Review," *AIAA Journal,* vol. 36, no. 2, pp. 173-184, 1998.

[23] "cfd-online.com," 25 October 2016. [Online]. Available: https://www.cfd-online.com/Wiki/Two_equation_turbulence_models.

[24] D. Wilcox, "Reassessment of the Scale-determining Equation for Advanced Turbulence Models," *AIAA,* vol. 26, no. 11, pp. 1299-1310, 1988.

[25] D. Wilcox, "Comparison of Two-equation Turbulence Models for Boundary Layers with Pressure Gradients," *AIAA,* vol. 31, no. 8, pp. 1414-1421, 1993a.

[26] D. Wilcox, "Turbulence Modelling for CFD,," DCW Industries Inc., La Canada, CA, 1993b.

[27] F. Menter, "Performance of Popular Turbulence Models for Attached and Separated Adverse Pressure Gradient Flow," *AIAA,* vol. 30, pp. 2066-2072, 1992a.

[28] F. Menter, "Improved Two-equation k-ω Turbulence Models for," NASA Technical Memorandum TM-103975, CA, 1992b.

[29] F. Menter, "Two-equation Eddy-viscosity Turbulence Model for Engineering Applications," *AIAA,* vol. 32, pp. 1598-1605, 1994.

[30] F. Menter, "Eddy-viscosity Transport Equations and their Relation to the k–ε Model," *Fluids Engineering,* vol. 119, no. 4, pp. 876-884, 1997.

[31] G. Hetsroni, "Particles-turbulence interaction," *Intl J. Multiphase Flow,* vol. 15, pp. 735-746, 1989.

[32] R. A. Gore and C. T. Crowe, "Modulation of turbulence by dispersed phase," *J. Fluids Engineering,* vol. 113, pp. 304-307, 1991.

[33] K. D. Squires and J. K. Eaton, "Particle response and turbulence modification in isotropic turbulence," *Phys. Fluids A,* vol. 2, pp. 1191-1203, 1990.

[34] S. E. Elghobashi and G. C. Truesdell, "On the two-way interaction between homogeneous turbulence and dispersed solid particles. I: Turbulence modication," *Phys. Fluids A,* vol. 5, pp. 1790-1801, 1993.

[35] M. Maeda, H. Kiyota and K. Hishida, "Heat transfer to gas-solids two-phase flow in separated, reattached, and redevelopment regions," in *7th Intl Heat Transfer,* Munich, 1982.

[36] K. Hishida and M. Maeda, "Turbulence characteristics of particle-laden flow behind a reward facing step," *ASME FED,* vol. 121, pp. 207-212, 1991.

[37] Y. Hardalupas, A. M. K. P. Taylor and J. H. Whitelaw, “Particle dispersion in a vertical round sudden expansion flow,” *Royal Society London,* vol. 341, pp. 411-442, 1992.

[38] J. Fessler and J. Eaton, “Turbulence modification by particles in a backward-facing step flow,” *Fluid Mech.,* vol. 394, pp. 97-117, 1999.

[39] R. Kasper, J. Turnow and N. Kornev, “Numerical modeling and simulation of particulate fouling of structured heat transfer surfaces using a multiphase Euler-Lagrange approach,” *Heat and Mass Transfer,* vol. 115, pp. 932-945, 2017.

[40] F. Greifzu, C. Kratzscha, T. Forgberb, F. Lindnera and R. Schwarzea, “Assessment of particle-tracking models for dispersed particle-laden flows implemented in OpenFOAM and ANSYS FLUENT,” *Engineering Applications of Computational Fluid Mechanics,* vol. 10, no. 1, pp. 30-43, 2016.

[41] H. Meng and K. Ludema, “Wear models and predictive equations: their form and content,” *Wear,* Vols. 181-183, pp. 443-457, 1995.

[42] M. Parsi, K. Najmi, F. Najafifard, S. Hassani, B. S. McLaury and S. A. Shirazi, “A comprehensive review of solid particle erosion modeling for oil and gas wells and pipelines applications,” *Natural Gas Science and Engineering,* vol. 21, pp. 850-873, 2014.

[43] I. Finnie, “The Mechanism of Erosion of Ductile Metals,” *3rd US Nat. Congress of Applied Mechanics, New York, ASME,* pp. 527-532, 1958.

[44] I. Finnie, “Erosion of surfaces by solid particles,” *Wear,* vol. 3, no. 2, pp. 87-103, 1960.

[45] A. Levy, Solid Particle Erosion and Erosion - Corrosion of Materials, ASM International, Material Park, Ohio: ISBN 0-87170-519-2, 1995.

[46] R. Bellman and A. Levy, “Erosion meschanism in ductile metals,” *Wear,* vol. 70, pp. 1-28, 1981.

[47] S. Srinivasan and R. O. Scattergood, “Effect of erodent hardness on erosion of brittle materials,” *Wear,* vol. 128, no. 2, pp. 139-152, 1988.

[48] G. Sundararajan, “A comprehensive model for the solid particle erosion of ductile materials,” *Wear,* vol. 149, no. 1-2, pp. 111-127, 1991.

[49] I. Kleis and P. Kulu, Solid Particle Erosion Occurrence, Prediction and Control, Library of Congress Control Number: 2007937988.2007937988 ed., Springer-Verlag London Limited, 2008.

[50] V. Sooraj and V. Radhakrishnan, “Elastic Impact of Abrasives for Controlled Erosion in Fine Finishing of Surfaces,” *Manufacturing Science and Engineering,* vol. 135, no. 5, 2013.

[51] I. Finnie, “Some observations on the erosion of ductile metals,” *Wear,* vol. 19, no. 1, pp. 81-90, 1972.

[52] J. Bitter, “A study of erosion phenomena part I,” *Wear,* vol. 6, no. 1, pp. 5-21, 1963.

[53] J. Bitter, “A study of erosion phenomena: Part II,” *Wear,* vol. 6, no. 3, pp. 169-190, 1963.

[54] S. Sato, A. Shimizu and T. Yokomine, “Numerical prediction of erosion for suspension,” *Wear,* Vols. 186-187, pp. 203-209, 1995.

[55] A. Gnanavelu, N. Kapur, A. Neville, J. Flores and N. Ghorbani, "A numerical investigation of a geometry independent integrated method to," *Wear,* vol. 271, pp. 712-719, 2011.

[56] W. Jennings, W. Head and C. Manning Jr., "A mechanistic model for the prediction of ductile erosion," *Wear,* vol. 40, no. 1, pp. 93-112, 1976.

[57] I. Hutchings, R. Winter and J. Field, "Solid particle erosion of metals: the removal of surface material by spherical projectiles," *Proc. R. Soc. Lond. Ser. A Math. Phys. Sci.,* vol. 348, pp. 370-392, 1976.

[58] I. Hutchings, "A model for the erosion of metals by spherical particles at normal incidence," *Wear,* vol. 70, no. 3, pp. 269-281, 1981.

[59] C. Huang, S. Chiovelli, P. Minev, J. Luo and K. Nandakumar, "A comprehensive phenomenological model for erosion of materials in jet flow," *Powder Technology,* vol. 187, pp. 273-279, 2008.

[60] L. Coffin, "A study of the effect of cyclic thermal stresses on a ductile metals," *Trans. ASME,* vol. 76, pp. 931-950, 1954.

[61] S. Manson, "Behavior of Materials Under Conditions of Thermal Stress," *Heat Transfer Symposium,* pp. 9-75, 1953.

[62] M. Salama and E. Venkatesh, "Evaluation of API RP 14E Erosional Velocity Limitations for Offshore Gas Wells," in *Offshore Technology Conference*, Houston, Texas, 1983.

[63] A. Bourgoyne, "Experimental study of erosion in diverter systems due to sand production," in *SPE/IADC Drilling Conference*, New Orleans, Louisiana, 1989.

[64] K. Jordan, "Erosion in Multiphase Production of Oil & Gas," in *Corrosion 98, Paper No. 58, NACE International Annual Conference*, San Antonio, California, 1998.

[65] L. Timothy, *Laser Doppler Velocimeter Measurements for Validation of Turbulence Modeling in Choke Geometries (Master of Science Thesis),* Tulsa: University of Tulsa, 1999.

[66] L. Timothy and M. McLaury, "Laser Doppler velocimeter measurements to characterize turbulence in a constriction with sharp and rounded inlets," *Exp. Fluids,* vol. 32, no. 4, pp. 472-480, 2002.

[67] R. Bahoosh Kazerooni, A. Noghrehabadi, S. Bahrainian and M. Parsi, "V2f study of nano and micro-particles transportation in turbulent boundary layer in conjunction with Eddy Interaction Model," Taipei, Taiwan, 2010.

[68] M. Parsi, M. Mahdavimanesh and A. Noghrehabadi, "Surveying aerosol deposition in a turbulent duct flow," in *20th Annual Conference of Mechanical Engineering*, Shiraz, Iran, 2012.

[69] J. Hinze, "Turbulent fluid and particle interaction," *Prog. Heat Mass Transf.,* vol. 6, pp. 433-452, 1972.

[70] M. Phillips, "A force balance model for particle entrainment into a fluid stream," *Phys. D Appl. Phys.,* vol. 13, pp. 221-233, 1980.

[71] D. Milojevic, "Lagrangian Stochastic-Deterministic (LAD) prediction of particle dispersion in turbulence," *Syst. Charact.,* vol. 7, pp. 181-190, 1990.

[72] Q. Lu, J. Fontaine and G. Aubertin, "Particle motion in two-dimensional confined turbulent flows," *Aerosol Sci. Technol.,* vol. 17, no. 3, pp. 169-185, 1992.

[73] V. Mehrotra, G. Silcox and P. Smith, “Numerical simulation of turbulent particle dispersion using a Monte Carlo approach,” in *ASME Fluids Engineering Division Summer Meeting*, Washington, DC, 1998.

[74] G. Klose, B. Rembold, R. Koch and S. Wittig, “Comparison of state-of-the-art droplet turbulence interaction models for jet engine combustor conditions,” *Int. J. Heat Fluid Flow,* vol. 22, pp. 343-349, 2001.

[75] C. Marchiolo and A. Soldati, “Mechanisms for particle transfer and segregation in a turbulent boundary layer,” *Fluid Mechanics,* vol. 468, pp. 283-315, 2002.

[76] A. Gosman and E. Ioannides, “Aspects of computer simulation of liquid-fuelled combustors,” *Energy,* vol. 7, pp. 482-490, 1983.

[77] X. Chen, B. McLaury and S. Shirazi, “Application and experimental validation of a computational fluid dynamics (CFD)-based erosion prediction model in elbows and plugged tees,” *Computers & Fluids,* vol. 33, pp. 1251-1272, 2004.

[78] K. Ahlert, *Effects of particle impingement angle and surface wetting on solid particle erosion of AISI 1018 Steel,* University of Tulsa, Tulsa, Master Science Thesis, 82pp., 1994.

[79] Y. Zhang, E. Reuterfors, B. McLaury, S. Shirazi and E. Rybicki, “Comparison of computed and measured particle velocities and erosion in water and air flows,” *Wear,* vol. 263, pp. 330-338, 2007.

[80] A. Gnanavelu, N. Kapur, A. Neville and J. Flores, “An integrated methodology for predicting material wear rates due to erosion,” *Wear,* vol. 267, pp. 1935-1944, 2009.

[81] C. Wong, C. Solnordal and A. W. J. Swallow, “Experimental and computational modelling of solid particle erosion in a pipe annular cavity,” *Wear,* vol. 303, pp. 109-129, 2013.

[82] Z. Lin, X. Ruan, Z. Zhua and X. Fua, “Numerical study of solid particle erosion in a cavity with different wall heights,” *Powder Technology,* vol. 254, pp. 150-159, 2014.

[83] T. Anderson and R. Jackson, “A fluid mechanical description of fluidised beds: Equations of motion,” *Industrial and Chemistry Engineering Fundamentals,* vol. 6, pp. 527-534, 1967.

[84] K. Kafui, B. Thornton and J. Frohlich, “Discrete particle-continuum fluid modelling of gas-solid fluidised beds,” *Chemical Engineering Science,* vol. 57, no. 13, 2002.

[85] R. Sun and H. Xiao, “SediFoam: A general-purpose, open-source CFD-DEM solver for particle-laden flow with emphasis on sediment transport,” *Computers and Geosciences,* vol. 89, pp. 207-219, 2016.

[86] R. Courant, K. Friedrichs and H. Lewy, “On the partial difference equations of mathematical physics,” *IBM Journal of Research and Development,* vol. 11, no. 2, pp. 215-234, 1967.

[87] E. Robertson, V. Choudhury, S. Bhushana and D. Walters, “Validation of OpenFOAM numerical methods and turbulence models for incompressible bluff body flows,” *Computer and Fluids,* vol. 123, pp. 122-145, 2015.

[88] C. Greenshields, “OpenFOAM v8 User Guide: 4.5 Numerical schemes,” OpenFOAM Foundation, 2020.

[89] T. Barth and D. Jespersen, “The design and application o fupwind schemes on un-structured meshes,” 1989.

[90] Fernandes, Semyonov, Ferrás and M. Nóbrega, “Validation of the CFD-DPM solver DPMFoam in OpenFOAM through analytical, numerical and experimental comparisons,” *Granular Matter,* no. 18 August 2018, p. 20:64, 2018.

[91] R. Issa, “Solution of the implicitly discretised fluid flow equations by operator-splitting,” *Computational Physics,* vol. 62, no. 1, pp. 40-65, 1986.

[92] S. Patankar and D. Spalding, “A calculation procedure for heat, mass and momentum transfer in three-dimensional parabolic flows,” *International Journal of Heat and Mass Transfer,* vol. 15, no. 10, pp. 1787-1806, 1972.

[93] L. Chen, J. Zang, A. Hillis, G. Morgan and A. Plummer, “Numerical investigation of wave – structure interaction using OpenFOAM,” *Ocean Engineering,* vol. 88, pp. 91-109, 2014.

[94] K. D. Squires and J. K. Eaton, “Particle response and turbulence modification in isotropic turbulence,” *Fluid Dynamics,* vol. 2, no. 7, 1990.

[95] M. Sommerfeld, Particle Motion inFluids, VDI Heat Atlas: Springer, 2010.

[96] B. Vreman, B. J. Geurts, N. Deen, J. Kuipers and J. Kuerten, “Two- and Four-Way Coupled Euler–Lagrangian Large-Eddy Simulation of Turbulent Particle-Laden Channel Flow,” *Flow, Turbulence and Combustion* , vol. 82, p. 47–71, 2008.

[97] S. Elghobashi, “On Predicting Particle-Laden Turbulent Flows,” *Applied Scientific Research,* vol. 52, pp. 309-329, 1994.

[98] M. Vångö, S. Pirker and T. Lichtenegger, “Unresolved CFD–DEM modeling of multiphase flow in densely packed particle beds,” *Applied Mathematical Modelling,* vol. 56, pp. 501-516, 2018.

[99] Z. Peng, E. Doroodchi, C. Luo and B. Moghtaderi, “Influence of void fraction calculation on fidelity of CFD-DEM simulation of gas-solid bubbling fluidized beds,” *AIChE Journal,* vol. 60, no. 6, p. 2000–2018, 2014.

[100] P. Saffman, “The lift on a small sphere in a slow shear flow,” *J. Fluid Mech.,* vol. 22, pp. 385-400, 1965.

[101] P. Saffman, “Corrigendum to "The Lift on a Small Sphere in a Slow Shear Flow,” *J. Fluid Mech.,* vol. 31, no. 3, p. 624, 1968.

[102] R. Mei and J. Klausnert, “Shear lift force on spherical bubbles,” *International Journal of Heat and Fluid Flow,* vol. 15, no. 1, pp. 62-65, 1994.

[103] T. Auton, J. Hunt and M. Prud'Homme, “The force exerted on a body in inviscid unsteady non-uniform rotational flow,” *Fluid Mechanics,* vol. 197, pp. 241-257, 1988.

[104] F. Odar, “Verification of the proposed equation for calculation of the forces on a sphere accelerating in a viscous flow,” *Fluid Mechanics,* vol. 25, no. 3, pp. 591-592, 1966.

[105] E. E. Michaelides and A. Roig, “A reinterpretation of the Odar and Hamilton data on the unsteady equation of motion of particles,” *Particle Technology and Fluidization,* 2010.

[106] A. E. Husam and D. K. Tafti, “Development and validation of a re duce d order history force model,” *International Journal of Multiphase Flow,* vol. 85, p. 284–297, 2016.

[107] Y. Tsuji, T. Kawagushi and T. Tanaka, “Lagrangian numerical simulation of plug flow of cohesionless particles in a horizontal pipe,” *Powder Technology,* vol. 71, pp. 239-250, 1992.

[108] F. Liu, “A Thorough Description Of How Wall Functions Are Implemented In OpenFOAM,” Chalmers University of Technology, Stockholm, 2017.

[109] J. Southard, “Introduction to Fluid Motions, Sediment Transport, and Current-Generated Sedimentary Structures,” in *Course Textbook,* MIT, 2006, p. 102.

[110] F. R. Menter, “Zonal Two Equation k-ω Turbulence Models for Aerodynamic Flows,” *AIAA 93-2906 Paper,* 1993.

[111] R. Neve and T. Shansonga, “The effects of turbulence characteristics on sphere drag,” *Heat and Fluid Flow,* vol. 10, no. 4, pp. 318-321, 1989.

[112] E. Marshall and M. Shaw, “Forces in dry surface grinding,” *Trans. Am. Soc. Mech. Engrs.,* vol. 51, p. 74, 1952.

[113] T. H. Courtney, Mechanical Behavior of Materials, Singapore: McGraw-Hill Publ. Co., ISBN 0-07-100680-X, 1990.

[114] C. J. McMahon and C. D. Graham, Introduction to Engineering Materials, 2 ed., Merion Books, 1992.

[115] B. McLaury, *Predicting solid particle erosion resulting from turbulent fluctuations in oilfield geometries,* University of Tulsa, Tulsa, MAster of Science Thesis, 115pp, 1996.

[116] D. Legendre, R. Zenit, C. Daniel and P. Guiraud, “A note on the modelling of the bouncing of spherical drops or solid spheres on a wall in viscous fluid,” *Chemical Engineering Science,* vol. 61, pp. 3543-3549, 2006.

[117] R. Davis, J. Serayssol and E. Hinch, “The elastohydrodynamic collision of two spheres,” *Fluid Mechanics,* vol. 163, p. 479, 1986.

[118] L. Chen, K. Asai, T. Nonomura, G. Xi and T. Liu, “A review of Backward-Facing Step (BFS) flow mechanisms, heat transfer and control,” *Thermal Science and Engineering Progress,* vol. 6, pp. 194-216, 2018.

[119] G. Kalitzin, G. Medic, G. Iaccarino and P. Durbin, “Near-wall behavior of RANS turbulence models and implications for wall functions,” *Computational Physics,* vol. 204, pp. 265-291, 2005.

[120] R. Kasper, “Particle Simulation with OpenFOAM,” in *German OpenFOAM User Meetings 2017 (GOFUN2017),* University of Rostock, 2017.

[121] S. Kalpakjian and S. Schmid, Manufacturing Processes for Engineering Materials, University of Michigan, Illinois Institute of Technology: Addison-Wesley, 6th Edition, 1984.

[122] E. E. Michaelides, Nanofluidics - Thermodynamic and Transport Properties, New York: Springer, 2014.

[123] F. Chalot, G. Chevalier, Q. Dinh and L. Giraud, *Some investigations of domain decomposition techniques in parallel cfd,* Lecture Notes in Computer Science, 1685:595–602, 1999.

[124] J. T. Farmer and J. R. Howell, “Comparison of Monte Carlo Strategies for Radiative Transfer in Participating Media,” *Advances in Heat Transfer,* pp. 333-429, 1998.

[125] S. Luding, “Introduction to discrete element methods: Basic of contact force models and how to perform the micro-macro transition to continuum theory,”

European Journal of Environmental and Civil Engineering, vol. 12, no. 7-8, pp. 785-826, 4 10 2011.

[126] J. Link, L. Cuypers, N. Deen and J. Kuipers, "Flow regimes in a spout–fluid bed:A combined experimental and simulation study," *Chemical Engineering Scienc*, vol. 60, pp. 3425-3442, 2005.

[127] M. Vångö, S. Pirker and T. Lichtenegger, "Unresolved CFD–DEM modeling of multiphase flow in densely packed particle beds," *Applied Mathematical Modelling*, vol. 56, pp. 501-516, 2018.

[128] G. Sundrarajan and P. Shewmon, "A new model for the erosion of metals at normal incidence," *Wear*, vol. 84, no. 2, pp. 237-258, 1983.

[129] D. Tabor, The Hardness of Metals, Oxford: Clarendon Press, 1951.

[130] S. Shirazi, J. Shadley, B. McLaury and E. Rybicki, "A procedure to predict particle erosion in elbows and tees," *Press. Technol.*, vol. 117, pp. 45-52, 1995.

[131] K. Jordan, "Erosion in Multiphase Production of Oil & Gas," San Antonio, 1998.

[132] P. Weiner and G. Tolle, "Detection and Prevention of Sand Erosion of Production Equipment," API OSAPER Project No. 2, American Petroleum Inst., Texas A&M Research Foundation, 1976.

[133] G. Tolle and D. Greenwood, "Design of Fittings to ReduceWear Caused by Sand Erosion," API OSAPER Project No. 6, American Petroleum Inst., Texas A&M Research Foundation, 1977.

[134] S. Haeri, *Hierarchical modelling of multiphase flows using fully resolved fixed mesh and PDF approaches*, University of Southmpton, Faculty of Engineering and the Environment, Doctoral Thesis, 277pp., 2012.

[135] M. Mamoun, "Analytical Models for the Erosive-Corrosive Wear Process," Argonne National Laboratory, Argonne, Illinois, 60439, 1975.

[136] E. Rabinowicz, "The Wear Equation for Erosion of Metals by Abrasive Particles," Department of ME, MIT, 1979.

[137] J. Chen, Y. Wang, X. Li, R. He, S. Han and Y. Chen, "Erosion prediction of liquid-particle two-phase flow in pipeline elbows via CFD–DEM coupling method," *Powder Technology*, vol. 282, pp. 25-31, 2015.